Exchange Bias Effect and Hard Disk Media Studied by Means of Quantitative Magnetic Force Microscopy
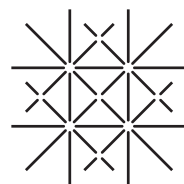
Peter Kappenberger

aus Leonberg (Deutschland)

Basel, 2005

UNI
BASEL

Genehmigt von der Philosophisch-Naturwissenschaftlichen Fakultät

auf Antrag der Herren Professoren:

Prof. Dr. H.-J. Güntherodt
Prof. Dr. H. J. Hug
Prof. Dr. E. Meyer

Basel, den 2. Dezember 2003

Prof. Dr. M. Tanner, Dekan

Erklärung

Hiermit erkläre ich, dass ich die Dissertation mit dem Titel

Exchange Bias Effect and Hard Disk Media
Studied by Means of
Quantitative Magnetic Force Microscopy

nur mit der darin angegebenen Hilfe verfasst, und bei keiner anderen Fakultät eingereicht habe.

Basel, 2. Dezember 2003

Contents

Introduction

The first method to reliably image magnetic materials was introduced by Bitter [1] and Hámod and Thiessen [2]. They provided the first direct experimental evidence for magnetic domains, postulated by Weiss in his theory of ferromagnetism [3]. The experimental technique relies on the so called *decoration* of the surface of a magnetic sample by small magnetic particles. These particles arrange themselves on the surface governed by the interaction with the stray field gradient of the sample. The major disadvantages of this method are that only one specific magnetization state of the sample can be investigated. It is not possible to image the evolution of the domain structure in an external magnetic field, because the particles remain fixed on the sample surface after the initial decoration.

The principle of the decoration method, namely the interaction of a magnetic particle with the stray field or stray field gradient of the sample represents also a core element of a magnetic force microscope (MFM). In contrast to the Bitter technique, in magnetic force microscopy, an arbitrary sample area can be scanned and the evolution of an arbitrary magnetization structure can be studied as a function of temperature and magnetic field. The MFM is a member of the scanning force microscope family, developed for the measurement of magnetic forces between a sensor and a magnetic sample. In analogy to the atomic force microscope, the MFM uses a cantilever with a sharp tip which carries a magnetic moment. This small modification makes the scanning force microscope (SFM) sensitive to the magnetic stray field emanating from a magnetization distribution in the sample. Other sensors, for example Hall sensors or magnetoresistive sensors can be used in an SFM as well. However, their spatial magnetic resolution is much lower than that of the MFM. Therefore the magnetic force microscope is more commonly used in the investigation of magnetic samples.

The first successful measurements with an MFM were performed only three years after the invention of the scanning force microscope [4, 5]. The first important results published were studies of magnetic recording media [6]. Since then, the MFM has been a valuable tool to image and analyze recording media and write heads. Further, over the last 15 years, a wide variety of hard and soft magnetic samples have been investigated under various conditions, such as in air, vacuum [7], at cryogenic temperatures [23] or in large external magnetic fields [8] with this technique. Moreover, the improvement in quality of the instruments as well as the measurement methods have allowed the development of procedures to quantitatively understand the measurement contrast. It is possible to *calibrate* an MFM tip in order to determine the sample stray field from MFM data. A very reliable and powerful method was developed by van Schendel [9].

In recent years other imaging techniques with a high spatial resolution of magnetization structures have emerged, namely photo-emission electron microscopy (PEEM) [10, 11] and scanning electron microscope with polarization analysis (SEMPA) [12, 13]. These methods have the potential to achieve a resolution equal to magnetic force microscopy. However, the machine maintenance costs, complexity of sample preparation and instrument operation has prevented their widespread use. Figure 0.0.1 shows a direct comparison of an MFM

measurement and a SEMPA measurement on the same hard disk media. The MFM image was acquired with the prototype of a new industrial standard MFM, designed and built during this Ph.D. thesis at the University of Basel. The SEMPA image was measured by Kohashi-san at Hitachi Global Storage Devices, Japan. The size of the images is 500 nm × 500 nm and 400 nm × 400 nm, respectively. The lateral magnetic resolution in both images is about 10 nm.
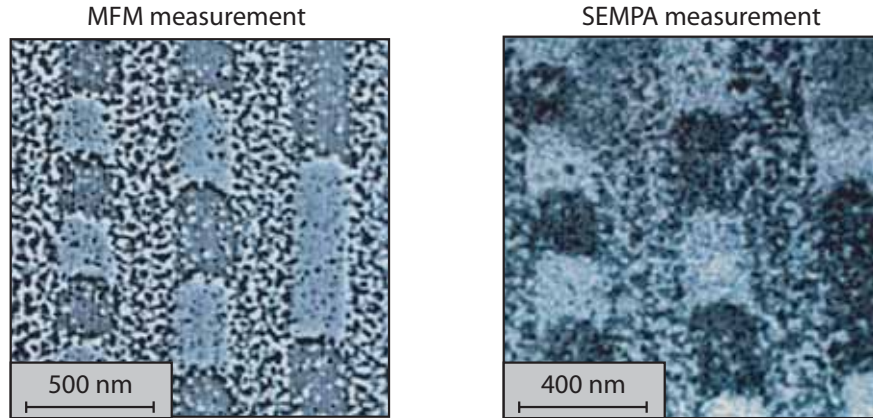
Fig. 0.0.1: Comparison of an MFM and SEMPA measurement on the same hard disk media. The resolution in both images is about 10 nm.

Outline of the thesis

More than 15 years after its invention, the MFM has become a widespread tool to characterize magnetic materials and structures. However, the impact of the technique in academic and industrial research has declined in recent years due to the lack of lateral magnetic resolution and the possible influence of the tip stray field on the magnetization structure of the sample. Moreover, a profound understanding of the contrast formation in an MFM experiment and hence the quantification of measured MFM data remains elusive.

In the first chapter of this thesis, the contrast formation in an MFM image is described by a transfer function theory. The theory in combination with experimental methods introduced by van Schendel [9] allows the calibration of the imaging properties of an MFM tip and therefore the quantitative interpretation of an MFM measurement ($\rightarrow$ chapter 1).

All data presented in this thesis were acquired by either a low temperature ultra high vacuum microscope (LTSFM) or a high resolution magnetic force microscope (hr-MFM) designed and build for the investigation of hard disk media in an industrial environment ($\rightarrow$ chapter 2).

In order to improve the lateral resolution down to about 10 nm, ultrasharp tips with a high aspect ratio and a magnetic coating thickness of only a few nanometers have to be used. In addition, the tip–sample distance during data acquisition has to be decreased to below 10 nm. In this distance regime, non-magnetic forces, e.g. the van der Waals force, become comparable to the magnetic force. As a consequence, new methods to separate the magnetic from the non-magnetic contributions to an MFM measurement (and therefore to an MFM image) were developed ($\rightarrow$ chapter 3.1). Further, the influence of the tip geometry and its coating on the magnetic imaging properties were studied. In high resolution MFM ultra sharp, fragile tips are used, so that any tip–sample contact destroys the tip. However, achieving this is not trivial

because the tips are typically used for the acquisition of micron-sized images, which takes place at tip–sample distances of only a few nanometers. In the last part of the chapter, the degradation of the imaging properties of tips of various geometry, after tip–sample contacts of increasing intensity were studied ($\rightarrow$ chapter 3.3).

The high resolution images on hard disk media obtained with the hr-MFM has sparked the interest in the magnetic recording industry in this technique. The knowledge gained in the process of the work presented in the thesis and the wish of the industrial researchers to perform high resolution MFM measurements on their hard disk media has led to an intense interaction between the research group in Basel and various industrial labs. In several visits to these labs during this thesis, the importance of a quantitative interpretation of hr-MFM images of recording media became apparent. Up to now, the performance of hard disk media, read and write heads was mostly characterized in spin stand experiments. Although, the MFM images obtained with the hr-MFM resolved the micromagnetic structure of written tracks and bits in the media in great detail, the interpretation of these images in relation to typical quantities determined in spin stand experiments remained unclear. Hence, new image analysis procedures were developed which allow the extraction of head and media properties from the measured MFM data ($\rightarrow$ chapter 4). In the process of the analysis, it became apparent, that the recording performance of todays hard disk drives is determined by nano-scale physics of the media and the write head stray field.

The continuous demand for increased storage density throughout the last decade could only be met with an astonishingly rapid transfer of newly discovered physical phenomena into products of the computer industry. One example of this kind is the use of the GMR effect [15, 16] in read heads of magnetic storage devices such as hard drives. The basis of such a read head is a so-called spin-valve [87]. One of its components is a ferromagnetic (FM) layer with a magnetization direction stabilized by the exchange coupling of an adjacent antiferromagnetic (AF) layer. Although the effect of the exchange coupling is used in todays products, a detailed qualitative and quantitative understanding of the mechanism is still lacking. It is commonly accepted, that the interface of the AF and FM layer plays a key role. So far, the magnetic structure of the interface has only been studied by XMCD methods. These methods have the advantage of chemical sensitivity, thus in principle, the magnetic state of one specific element can be accessed. However, the disadvantages are the limited spacial resolution of XMCD microscopy methods, the complexity of the instrumentation,which involves a beam line at a synchrotron and the long data acquisition times. The latter makes experiments that require the variation of external parameters such as the temperature or the magnetic field, tedious. In chapter 5, an MFM based method is discussed that allows the determination of the uncompensated spin density with a superior lateral resolution and the study of the evolution of the domain structure in the ferromagnetic layers as a function of an applied external field.

Chapter 1

Theory of MFM contrast formation

In an MFM experiment, the image contrast is the result of the interaction of the tip magnetization with the stray field of the sample. The magnitude of the measurement signal depends on the stray field distribution when tip and sample are in close proximity. However, the magnetic field produced by the magnetization distribution of the tip, can affect the magnetization structure of the sample and vice versa. The strength of these pertubations depends on imaging conditions, tip and sample geometry and the coercitivity of the materials used. As a consequence the measured interaction may be a function of the tip–sample position or even the history of the measurement. Depending on the extent of the modification, the contrast formation process can be divided in three groups:

Negligible modification : As long as the magnetization of the tip and the distribution of the stray field of the sample do not change with the tip–sample position, the measured contrast can be described as a linear operation on the sample stray field.

Reversible modification : The distribution of the tip magnetization or the sample stray field can change with the tip–sample position. As long as all modifications in the system are reversible, the measured contrast is a function of the tip–sample position only.

Irreversible or hysteretic modification : The distribution of the tip magnetization or the sample stray field changes irreversibly with the tip–sample position. The measured contrast is a function of the tip–sample position and its history.

In this thesis the discussion of contrast formation in an MFM experiment is limited to the negligible modification case. As van Schendel [9] has pointed out, the quantitative analysis and reconstruction of the remaining two cases is complicated and largely unexplored. In order to determine if the tip and sample modifications are negligible, a test procedure described in detail in [14, 17] can be used (see also the end of section 1.1).

1.1 The magnetization and stray field of the sample

In general, the magnetic stray field emanating from a ferromagnetic sample can be calculated [18] by:

$$\mathbf{H}(\mathbf{r}) = -\int_V \nabla \cdot \mathbf{M}(\mathbf{r}') \frac{\mathbf{r} - \mathbf{r}'}{|\mathbf{r} - \mathbf{r}'|^3} dV' + \int_A \hat{\mathbf{n}} \cdot \mathbf{M}(\mathbf{r}') \frac{\mathbf{r} - \mathbf{r}'}{|\mathbf{r} - \mathbf{r}'|^3} dA', \qquad (1.1.1)$$

7

where the integrals are performed over the ferromagnetic volume V and the surface A of the sample respectively. $\hat{\mathbf{n}}$ defines the outward unit normal vector from the sample surface. A general vector field (e.g., the magnetization $\mathbf{M}$) can be written as a sum of a divergence free part $\mathbf{M}_{rot}$ and a curl free part $\mathbf{M}_{div}$:

$$\mathbf{M} = \mathbf{M}_{div} + \mathbf{M}_{rot} \quad \text{with} \quad \nabla \times \mathbf{M}_{div} = 0 \quad \text{and} \quad div\,\mathbf{M}_{rot} = 0. \tag{1.1.2}$$

Equation 1.1.1 implies that only the curl free part of the magnetization of the sample contributes to the stray field. Therefore an MFM measurement will only provide information about $\mathbf{M}_{div}$. This is one of the reasons for the statement that there are an "infinite number of magnetization patterns which generate the same stray field pattern".

In analogy with electrostatic fields, it is useful to define the magnetic volume charge ρ_M and the magnetic surface charge σ_M by

$$\begin{aligned} \rho_M &= -div\,\mathbf{M}, \\ \sigma_M &= \hat{n} \cdot \mathbf{M}. \end{aligned} \tag{1.1.3}$$

If the area above the sample is current free and does not contain any time–varying electrical fields, the curl of the magnetic stray field is zero ($rot\,\mathbf{H} = 0$). It can be expressed as the gradient of a magnetic scalar potential ϕ_M by $\mathbf{H} = -\nabla\phi_M$. The scalar potential can be calculated everywhere inside or outside the sample using the boundary conditions:

$$\begin{aligned} \Delta\phi_M &= 0 & \text{outside the sample,} \\ \Delta\phi_M &= -\rho_M & \text{inside the sample,} \\ \frac{\partial\phi_{M,i}}{\partial n} - \frac{\partial\phi_{M,o}}{\partial n} &= \sigma_M & \text{on the sample surface,} \end{aligned} \tag{1.1.4}$$

where $\phi_{M,o}$ and $\phi_{M,i}$ are the boundary values of ϕ_M outside and inside the sample respectively.

In order to derive some specific properties of the magnetostatic fields, the discussion is further pursued in Fourier space. The stray field of the sample as well as its magnetization can be transformed using the following Fourier transform pairs:

$$\begin{aligned} G(\mathbf{k}) &= \int_{-\infty}^{\infty} g(\mathbf{r})e^{-i\mathbf{k}\cdot\mathbf{r}}dxdy, \\ g(\mathbf{r}) &= \frac{1}{4\pi^2}\int_{-\infty}^{\infty} G(\mathbf{k})e^{-i\mathbf{k}\cdot\mathbf{r}}dk_xdk_y. \end{aligned} \tag{1.1.5}$$

Note that the above equations transform only the x and y coordinates of the triplet (x, y, z). As a consequence, in all the following equations, the coordinates are given as $(\mathbf{r}, z)$ and $(\mathbf{k}, z)$ where $\mathbf{r} = (x, y)$ and $\mathbf{k} = (k_x, k_y)$ are two–dimensional vectors.

From equation 1.1.4 and the special form of the nabla operator in Fourier space, $\nabla = (ik_x, ik_y, \partial/\partial z)$, it is easily derived that a sinusodial potential decays exponentially with the product of the magnitude of the k–vector, $k = (k_x^2 + k_y^2)^{1/2}$ and the distance from the sample

$$\phi_M(\mathbf{k}, z) = \phi_M(\mathbf{k}, 0)e^{-kz}. \tag{1.1.6}$$

A direct result of equation 1.1.6 is that the Fourier transform of the stray field $\mathbf{H}(\mathbf{k}, z)$ also decays exponentially with the distance z.

Outside the sample where the Laplace equation holds, the nabla operator can be further simplified to $\nabla = (ik_x, ik_y, -k)$. Hence the magnetic scalar potential, and thereby all stray

field components in the x-y–plane, can be determined from a measurement of the stray field in the z-direction, H_z, using the relationships:

$$\phi_M(\mathbf{k}, z) = -\frac{1}{k} H_z(\mathbf{k}, z),$$ (1.1.7)

$$\mathbf{H}(\mathbf{k}, z) = -\frac{\nabla}{k} H_z(\mathbf{k}, z).$$

Therefore it is not necessary to measure the sample stray field using a tip with an in-plane magnetization to derive the in-plane components of the stray field.

In addition, the exponential decrease of the stray field can be used to test whether the tip–sample modifications have indeed been negligible. If no modifications were induced in the tip and sample, the measured signal in two MFM images taken at the same lateral position (x,y) but at consecutive larger tip–sample separations z should decay exponentially [14].

Almost all measurements presented in the experimental chapters 3 to 5 were performed on magnetic thin films with a magnetization perpendicular to the film plane. The magnetization varies in x and y direction, but remains perpendicular to the surface of the sample, $\mathbf{M} = (0, 0, \pm M_s(x, y))$. Such a sample has only magnetic surface charges on the top and bottom surfaces and these are equal to $\pm M_z$. Using the boundary conditions in equation 1.1.4, the Fourier components of the stray field become:

$$\mathbf{H}(\mathbf{k}, z) = -\frac{\nabla}{k} H_z(\mathbf{k}, z) = \frac{e^{-kz}(1 - e^{-kt})}{2} \frac{\nabla}{k} \mathbf{M}(\mathbf{k}),$$ (1.1.8)

with t being the thickness of the magnetic layer.

1.2 The tip–sample interaction: Transfer function theory

In the negligible modification case, the magnetic force $\mathbf{F}(\mathbf{r}, z)$ can in principle be calculated in direct space as a convolution between the sample stray field and the derivative of the tip magnetization distribution, using:

$$\mathbf{F}(\mathbf{r}, z) = \mu_0 \int_{-\infty}^{\infty} \mathbf{H}_{sample}(\mathbf{r}', z') \cdot (-\nabla')\mathbf{M}_{tip}(\mathbf{r}' - \mathbf{r}, z' - z)d\mathbf{r}'dz'$$ (1.2.1)

The primed coordinate system is fixed at the tip apex with the $\mathbf{r}'$–plane parallel to the sample surface. The vector $(\mathbf{r}, z)$ denotes the position of the tip relative to the sample. The integration is performed over the whole space penetrated by the stray field. Equation 1.2.1 has only an analytic solution for special cases, for example, a magnetic point dipole at the end of the tip apex [14, 19] . However, if the two–dimensional Fourier transform of equation 1.1.5 is used, equation 1.2.1 can be rewritten in Fourier space:

$$\mathbf{F}(\mathbf{k}, z) = -\mu_0 \int_{-\infty}^{\infty} \mathbf{H}_{sample}(\mathbf{k}, z' + z) \cdot (-\nabla')\mathbf{M}_{tip}^*(\mathbf{k}', z')dz'$$

$$= -\mu_0 \mathbf{H}_{sample}(\mathbf{k}, z) \int_{-\infty}^{\infty} e^{-kz'}(-\nabla')\mathbf{M}_{tip}^*(\mathbf{k}', z')dz'$$ (1.2.2)

$$= \mu_0 \mathbf{H}_{sample}(\mathbf{k}, z)q_{tip}^*(\mathbf{k})$$

where the asterisk denotes the complex conjugate. It is important to note that the nabla operator $\nabla = (ik_x, ik_y, -k)$ cannot be used in equation 1.2.2, because the relation is only valid in source free space. The quantity $q_{tip}(\mathbf{k})$ is the Fourier transform of a tip-equivalent surface charge pattern (so called *tip transfer function*), with the surface charges located in

a plane parallel to the sample surface and touching the tip apex. In order to calculate the force acting on the tip from a given sample stray field, the function q_{tip} must be known. The quantity can be calculated by micromagnetic modelling calculations if the geometry of the tip and the distribution of the magnetic charges on the tip are known. However, for most tips, the geometry and homogeneity of the magnetic layer on the tip are undetermined, therefore any modelling approach will be an approximation. A procedure to determine the tip transfer function using a magnetic calibration sample is discussed in chapter 1.3. A detailed description is found in [9, 14].

The tip stray field below the before mentioned plane can be calculated from $q_{tip}(\mathbf{k})$ using the expression:

$$\mathbf{H}_{tip}(\mathbf{k}, z) = -\frac{1}{2k} \begin{pmatrix} ik_x \\ ik_y \\ -k \end{pmatrix} e^{k(z'-z)} q_{tip}(\mathbf{k}) \qquad (1.2.3)$$

with z being the tip–sample distance and $z' < z$ the distance of the plane, in which the tip field was calculated, to the sample.

In an MFM experiment, the measured quantity is either proportional to the force $F_{n_c}(\mathbf{k})$ in direction of the cantilever normal (for static acquisition modes) or its derivative $d/dn\, F_{n_c}(\mathbf{k})$ (for dynamic modes) as shown in figure 2.1.1. This direction is characterized by the vector $\mathbf{n} = (0, \sin\theta, \cos\theta)$, with θ being the angle between the axes of the tip and the normal of the sample surface (*canting angle*). Both, the normal force and the normal force derivative can be calculated from the force vector by [6]:

$$\frac{d}{dn} F_{n_c} = \mathbf{n} \cdot \nabla F_{n_c} = \mathbf{n_c} \cdot \nabla(\mathbf{n_c} \cdot \mathbf{F}). \qquad (1.2.4)$$

Inserting equations 1.2.2 and 1.1.7 into equation 1.2.4, it follows that

$$F_{n_c}(\mathbf{k}) = -\mathbf{n_c}\left(\mu_0 q_{tip}^*(\mathbf{k}) \frac{\nabla}{k} H_z(\mathbf{k})\right) = \mu_0 \sigma_{tip}^*(\mathbf{k}) LCF(\mathbf{k}, \theta) H_z(\mathbf{k}), \qquad (1.2.5)$$

$$\frac{d}{dn_c} F_{n_c} = -k\mu_0 q_{tip}^*(\mathbf{k}) [LCF(\mathbf{k}, \theta)]^2 H_z(\mathbf{k}), \qquad (1.2.6)$$

where $LCF(\mathbf{k}, \theta)$ is the *lever canting function* describing the effect of the canting of the cantilever with respect to the scan plane on the MFM measurement. The main effect of the canted orientation is a complex phase shift of the MFM measurement in the direction of the cantilever. A canting angle θ results in a phase shift of magnitude θ in static operation modes and 2θ in dynamic operation modes [9, 14].

All MFM images acquired for this thesis were performed in a dynamic constant height mode. Here, the measured signal is the frequency shift δf which can be related to the force acting on the tip, F_{n_c}, using [20, 21]:

$$\delta f(\mathbf{r}_0) = -\frac{f_0}{2c_L} \frac{2}{\pi a} \int_0^\pi F_{n_c}(\mathbf{r}(\phi)) \cos\phi \, d\phi \quad , \qquad (1.2.7)$$

with f_0 the free resonance frequency of the cantilever and c_L its force constant. The normalized oscillation amplitude is described by a and ϕ is a variable accounting for the oscillation angle. Inserting 1.2.5 into equation 1.2.7, it follows that:

$$\delta f(\mathbf{r}_0) = \frac{f_0 \mu_0}{2c_L} \frac{2}{\pi a} \int_0^\pi \frac{1}{4\pi^2} \int_{\mathbf{k}} q_{tip}^*(\mathbf{k}) \frac{\nabla \cdot \hat{\mathbf{n}}}{k} H_z(\mathbf{k}, 0) \cdot e^{\nabla \cdot \mathbf{r}(\phi)} d\mathbf{k} \cos\phi \, d\phi \qquad (1.2.8)$$

By expanding $\mathbf{r}(\phi)$, and changing the order of integration the frequency shift as a function of the sample stray field and the tip transfer function finally becomes:

$$
\begin{aligned}
\delta f(\mathbf{r}_0) &= \frac{f_0 \mu_0}{2c_L} \frac{1}{4\pi^2} \int_{\mathbf{k}} q_{tip}^* LCF(\mathbf{k}, \theta) H_z(\mathbf{k}, 0) e^{\nabla(\mathbf{k}) \cdot \mathbf{r}_0} \\
&\quad \times \frac{2}{\pi A} \int_0^\pi \exp\left[\nabla(\mathbf{k}) \cdot \hat{\mathbf{n}} A \cos\phi\right] \cos\phi \, d\phi \, d\mathbf{k} \qquad (1.2.9) \\
&= \frac{f_0 \mu_0}{2c_L} \frac{1}{4\pi^2} \int_{\mathbf{k}} q_{tip}^*(\mathbf{k}) LCF(\mathbf{k}, \theta) H_z(\mathbf{k}, 0) \, e^{\nabla(\mathbf{k}) \cdot \mathbf{r}_0} \cdot \frac{2}{A} I_1 \left[\nabla(\mathbf{k}) \cdot \hat{\mathbf{n}} A\right] d\mathbf{k},
\end{aligned}
$$

with $I_1(z)$ the first order modified Bessel function of the first kind with a complex argument [22].

It is useful to define an *instrumental calibration function*, $ICF(\mathbf{k})$ that describes the relation between the sample stray field (or its derivative) and the frequency shift. $ICF(\mathbf{k})$ can be directly determined from a calibration measurement. In addition to $q_{tip}(\mathbf{k})$, this function contains the properties of the cantilever and the lever canting function. Several instrumental calibration functions can be defined, at least one for each measurement mode. Appropriately for the dynamic acquisition mode used in the thesis, the definition of the instrumental calibration functions

$$
\begin{aligned}
ICF_{df/H_z}(\mathbf{k}) &= \frac{f_0}{2c_L} \mu_0 k q_{tip}^*(\mathbf{k}) [LCF(\mathbf{k}, \theta)]^2, & (1.2.10) \\
ICF_{df/dH_z}(\mathbf{k}) &= -\frac{f_0}{2c_L} \mu_0 q_{tip}^*(\mathbf{k}) [LCF(\mathbf{k}, \theta)]^2 & (1.2.11)
\end{aligned}
$$

are appropriate. Hereby, $ICF_{df/H_z}(\mathbf{k})$ describes the relation between the frequency shift and the z-component of the stray field and $ICF_{df/dH_z}(\mathbf{k})$ describes the relation between the frequency shift and the derivative of the z-component of the stray field.

1.3   Calibration of an MFM tip

The calibration of the MFM tip is a prerequisite for the quantitative analysis of an MFM measurement. The aim of the procedure is the determination of the magnetic properties of the MFM tip, including the magnitude of the effective dipole and monopole moments. Preferably, the calibration procedure should output the tip transfer function without any assumption about the geometry of the tip or its magnetic layer contrary to the calibration methods suggested by Madabhushi *et al.* [24], Chang *et al.* [25] and Zhu *et al.* [26][1]. Lohnau *et al.* [27] have introduced a method in which the cantilever is scanned across a current carrying ring emanating a well defined stray field. Measurements are performed as a function of the scan height and the stray field allowing the effective magnetic dipole and monopole moments of the tip to be calculated. However, these values depend on the geometry of the calibration sample. In the calibration method developed by van Schendel *et al.* [9, 14], the tip transfer function is independent of the calibration sample. In addition, no assumption about the distribution of the magnetic charges on the tip are necessary.

---

[1]Madabhushi *et al.* attempted to describe the tip transfer function by two dipole functions defining the MFM image of a magnetic point dipole on the sample. Chang *et al.* and Zhu *et al.* used an impulse response function, which they defined as the response of the tip to a magnetic point charge on the sample surface.

The choice of the calibration sample is important for the calibration process developed by van Schendel *et al.*. The magnetization direction should be perpendicular to the sample plane and homogenous throughout the film thickness. In addition, the saturation magnetization value has to be known very precisely for various measurement temperatures. The sample stray field should be large enough to allow the calibration of tips with a very low magnetic moment, but sufficiently small to prevent mutual modifications. On the other hand, the coercitivity of the sample should be high to prevent modifications of the sample by the tip stray field. Finally, the size distribution of the magnetic domains should be homogeneous for domain sizes ranging from a few hundred nanometers to less than 10 nm. Three types of sample have been successfully used to perform calibrations of MFM tips:
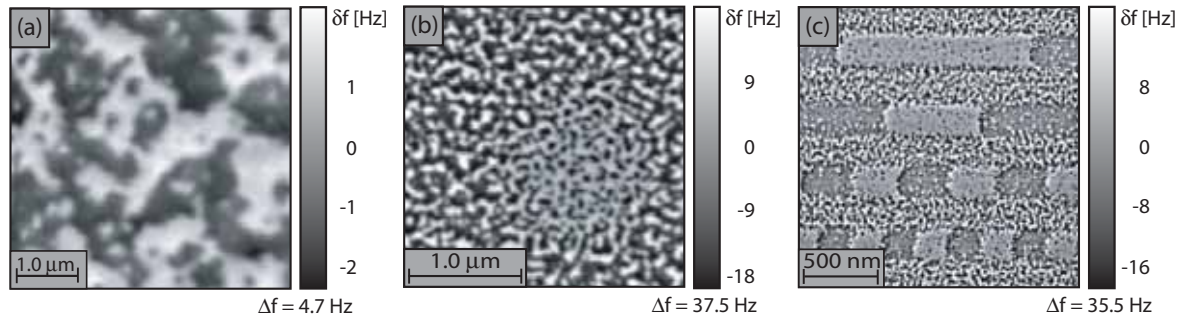

Fig. 1.3.1: Different calibration samples used for the tip calibration process. Panel (a) shows an MFM image of the Ni/Cu/Ni multilayer. Panel (b) depicts an image of the CAMST reference sample. In panel (c), an image of one of the new PRM calibration samples is shown

Cu/Ni/Cu multilayer : This sample consists of a Si(100) substrate on which a multilayer of 200 nm Cu, 8 nm Ni and 5 nm Cu has been deposited. The large lattice misfit between the Cu and the Ni layers creates a large magnetoelastic anisotropy in the magnetic layer and forces the magnetization vector into a perpendicular orientation. The saturation magnetization of Ni is 480 kA/m [28]. The domain size is about $1 \mu m$. The sample is described in detail in [29, 30] (Figure 1.3.1, panel (a)).

CAMST sample : This sample consists of 20 repetitions of a $Co_{50}Ni_{50}/Pt$ bilayer. Into the layer, bits were written by a magneto-optical method. The thickness of the $Co_{50}Ni_{50}$ layer is 0.55 nm and the thickness of the Pt layer is 1.2 nm. The sample has been suggested as a test sample for MFM imaging and tip calibration and used as such by many different groups. The saturation magnetization of the multilayer is 300 kA/m. However it creates a much stronger magnetic stray field than the Cu/Ni/Cu multilayer. The size of the smallest magnetic domains is about 15 nm. The sample is described in detail in [31] (Figure 1.3.1, panel (b)).

PMR samples : These samples were introduced as the new calibration samples in this thesis. The perpendicular magnetic recording (PRM) sample consists of a single poly-crystalline layer of a CoPtCrTa or CoPtCrB alloy grown on an silicon or aluminium substrate and a 20 nm seed layer of Ta. Into the magnetic layer, tracks of various bit densities have been written. The bit length ranges from 2 μm down to 35 nm, and the width varies between 200 nm and 450 nm. The grains of the layer have a diameter between 8 nm and 35 nm. They have perpendicular anisotropy and are well exchange decoupled. Therefore, beside the tracks, very small domains of one or several grains are formed. It is expected that the calibration of high resolution MFM tips is facilitated

because of a homogenous domain size distribution ranging from several micrometers to smaller than 10 nm. The saturation magnetization is 660 kA/m for the calibration sample from Hitachi Global Storage Devices (San Jose, USA) and 385 kA/m for the calibration sample from Seagate Research Center (Pittsburgh, USA). Most of the tip calibrations performed in this thesis have been carried out on one of these two samples (Figure 1.3.1, panel (c)).
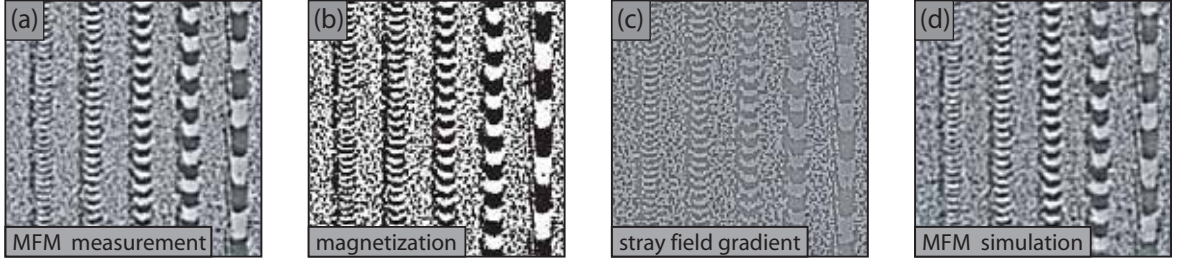

Fig. 1.3.2: Example of an MFM tip calibration process. From an MFM measurement (panel (a)), a magnetization image is calculated (panel (b)). Using the magnetization pattern, the stray field derivative (panel (c)) is computed. Using the tip transfer function $q_{tip}(\mathbf{k})$ an MFM measurement can be simulated (panel (d)). All images are 4μm $\times$ 4μm.

The calibration procedure uses equation 1.2.5, which states that the tip transfer function $q_{tip}(\mathbf{k})$ can be calculated from an MFM measurement if the stray field of the sample $H_z(\mathbf{k})$ is known. The sample stray field relies on the magnetization distribution inside the sample. For a perpendicular magnetized thin film in which the magnetization is homogenous throughout the film thickness ($\mathbf{M} = [0, 0, \pm M_s(x, y)]$), the magnetization pattern can easily be determined by applying a discrimination procedure to an MFM image (panel (a) of figure 1.3.2). From the magnetization pattern (panel (b)), the stray field or z-derivative of the stray field can be computed in a plane parallel to the sample surface touching the apex of the tip using equation 1.1.8. In panel (c), the stray field gradient was calculated in order to determine the instrumental calibration function $ICF_{df/dH_z}(\mathbf{k})$ and then the tip transfer function $q_{tip}(\mathbf{k})$. This is performed by a division of the Fourier components of the measurement by those of the stray field derivative. Calibration errors can be caused by contributions of the sample topography, non-negligible modifications of the sample or the tip magnetization and uncertainties in the magnetization estimate. These errors can be reduced by averaging over several calibration functions obtained from different MFM measurements [9, 14]. The standard deviation $\sigma_{q_{tip}}(\mathbf{k})$ gives a lower boundary for the error and can also be used to determine the maximum lateral magnetic resolution of the tip (cf. chapter 3.3). To test the quality of the calibration function, an MFM measurement can be simulated, using $q_{tip}(\mathbf{k})$ as shown in panel (d).

A useful representation of $q_{tip}(\mathbf{k})$ and $\sigma_{q_{tip}}(\mathbf{k})$ is shown in figure 1.3.3. It is calculated by a circular average of the frequency components having different directions but the same wave vector k in Fourier space, as described in reference [9, 17]. The averaged frequency components can be plotted and compared as a function of the wave vector or wavelength $\lambda = 2\pi/k$. The resulting spectrum is called *sensitivity spectrum*. A given value on the curve shows the magnetic imaging sensitivity of the tip for a magnetization pattern of a spatial wavelength. The wavelength is related to a corresponding magnetic resolution by $\lambda_r = \lambda/2$. In the ideal case of a magnetic monopol charge, $q_{tip}(\mathbf{k}) = q_0$, at the tip apex, all magnetic wave vectors are imaged with equal sensitivity. The resulting averaged tip transfer function would resemble a horizontal line in figure 1.3.3. A gradual decrease of the Fourier component values with increasing k represents an approximate monopole imaging behaviour of the tip.
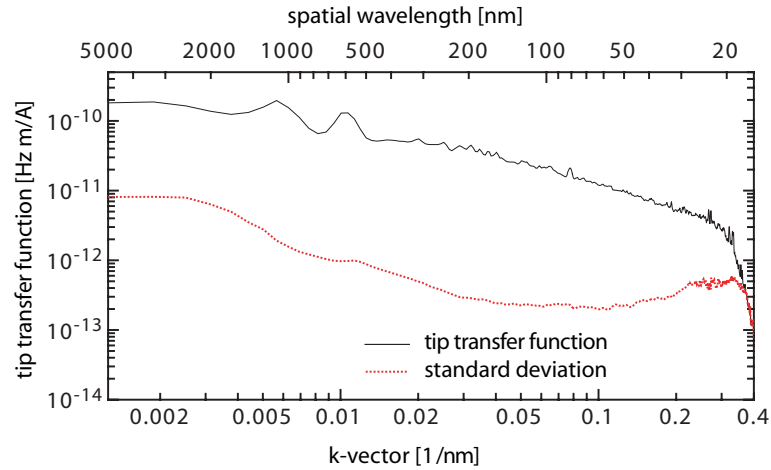
Fig. 1.3.3: Circular average of the average tip transfer function and its standard deviation as a function of the wave vector k and the wavelength λ.
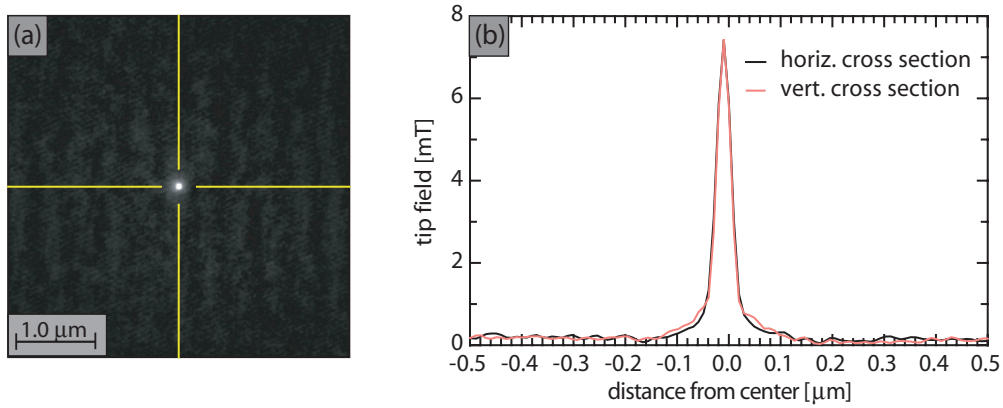
Fig. 1.3.4: Panel (a) shows the stray field distribution of the of the tip in a plane parallel to the surface of the sample touching the apex of the tip. Panel (b) shows a horizontal and vertical cross section along the lines in panel (a).

Knowing the tip transfer function, the tip stray field distribution in a plane parallel to the sample touching the tip apex can be calculated from equation 1.2.3. This is shown in figure 1.3.4, panel (a) and in a cross section in panel (b). A sharp decrease of the tip field from its maximum value, indicates better magnetic resolution. Moreover, in combination with a low peak field, the tip influence on the sample magnetization is reduced.

Chapter 2

Instrumentation

The heart of a scanning force microscope (SFM) measurement is the interaction between a tip of micrometer to nanometer dimensions and the sample surface. In order to determine the lateral and vertical variation of the interaction force, the tip and the sample can be moved relative to each other with sub–nanometer precision. The tip is situated on a cantilever of known geometry and spring constant. The deflection of the cantilever can be recorded and serves as a measure of the tip–sample interaction strength.

In this chapter, the principles of the different measurement modes used in this thesis are explained. All measurement data were acquired with the low temperature scanning force microscope (LTSFM) described in [7, 17, 32] and the newly built magnetic force microscope for high magnetic lateral resolution (hr-MFM). These microscopes are briefly discussed in sections 2.2 and 2.3.

2.1 The measurement principle

The magnitude of the interaction between the tip and the sample can be measured as a function of the spatial coordinates (x,y,z). The relative vertical and lateral positions are adjusted with sub–nanometer precision using piezo–electric actuators ($piezos$)[1]. In figure 2.1.1, the piezo elements are indicated in violet: one piezo is used to perform the scan motion in x, y and z, a second piezo vibrates the cantilever at a given frequency and amplitude; the third piezo is needed to keep the average distance between the cantilever bar and the fiber end face constant. This is important in order to compensate for slow thermal drifts of the fiber–cantilever system.

The tip is situated on a cantilever bar which deflects due to the tip–sample interaction. The deflection is detected by means of a laser beam reflected from the backside of the cantilever. The laser beam is brought into close proximity of the cantilever by an optical fiber. The reflections of the beam at the end–face of the fiber and at the cantilever bar produce an interference inside the fiber. If the oscillation amplitude of the cantilever is smaller than a quarter of the laser's wavelength, the interference leads to a sinusoidal modulation of the intensity of the laser beam guided through the fiber. The reflected laser beam is measured by

---

[1]The piezo–electric material is a ceramic compound which performs an elongation or contraction if a suitable voltage is applied. However, this mechanical movement is highly non–linear and depends strongly on the temperature and history of motion. Therefore the piezo has to be linearized and calibrated for each measurement temperature.
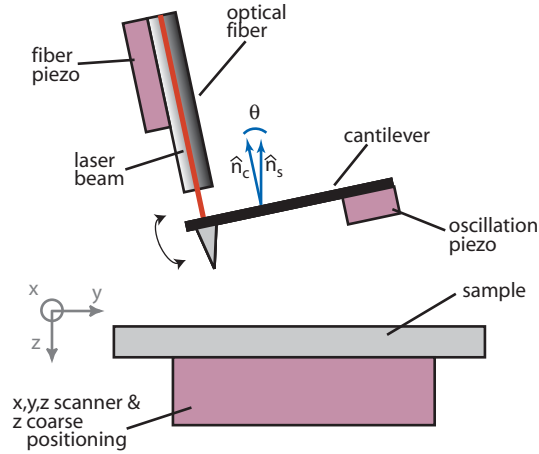
Fig. 2.1.1: Principle of non–contact scanning force microscopy used in this thesis: A tip is situated on a cantilever of known geometry and force constant. The deflection of the bar caused by a interaction of the tip with the sample is measured by a Michelson–interferometer. The sample can be scanned in x and y direction and the tip–sample separation (z direction) can be adjusted using piezo–electric actuators (*piezos*). The cantilever normal $\hat{\mathbf{n}}_c$ is tilted with respect to the sample surface normal $\hat{\mathbf{n}}_s$. The relative lateral and vertical tip–sample position can be adjusted with a coarse positioning system prior to measurement (not shown).

a photo diode and converted into an electric signal proportional to the laser light intensity. In order to avoid a contact of the cantilever chip with the sample surface, the cantilever normal $\hat{\mathbf{n}}_c$ is tilted with respect to the sample surface normal $\hat{\mathbf{n}}_s$.

All measurements performed in this thesis were performed in so called *dynamic non–contact* acquisition mode[2] in which the vibrational properties of the cantilever are recorded. The properties include the resonance frequency, the oscillation amplitude and the phase shift between the excitation and the oscillation of the cantilever. A complete review of dynamic modes has been given by Garcia *et al.* [33]. In this chapter, the focus is on measurement modes which record a tip–sample interaction by a shift in resonance frequency of the cantilever oscillation only.

A suitable theoretical model for a vibrating cantilever is a damped, driven oscillator. Its equation of motion in one dimension is described by:

$$c_L x(t) + \gamma \frac{\partial}{\partial t} x(t) + m_{eff} \frac{\partial^2}{\partial t^2} x(t) = F_{ts}(x) + F_{exc} \cos \omega t. \qquad (2.1.1)$$

Here, c_L and m_{eff} denote the spring constant and effective mass of the cantilever bar, F_{exc} is the driving force of the oscillation and F_{ts} is the measured interaction force. $\omega = 2\pi f$ and γ denote the oscillation frequency and the damping coefficient of the free oscillating cantilever,

---

[2]In general, SFM acquisition modes can be divided in *static* and *dynamic* modes. Using the first modes, the cantilever is scanned across the surface and its deflection due to a tip–sample interaction is recorded as the measurement signal. In the latter modes, the cantilever is excited with a certain frequency (usually its resonance frequency) while scanning over the sample. One of the dynamic properties of the cantilever (oscillation frequency, phase or amplitude) is recorded.

The above modes can be further subdivided into contact (tip is always in contact with sample), near–contact (tip is only a fraction of the oscillation cycle in contact with the sample) or non–contact modes (tip is never in contact with the sample).
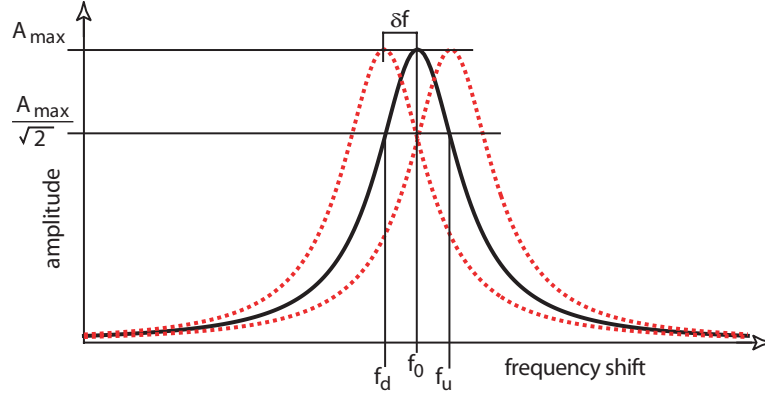
Fig. 2.1.2: Cantilever resonance curve acquired by oscillating the cantilever at a fixed amplitude while sweeping the frequency. The resonance curve of a free oscillating cantilever is depicted as solid black line, the shifted resonance curves due to an additional force field of attractive (repulsive) interaction is depicted at smaller (higher) frequencies as dotted red lines. The difference in the resonance frequency between the black and one of the red curves is called *frequency shift*.

respectively. The damping coefficient is related to its quality factor Q and the width of the resonance curve by

$$Q \equiv \frac{2\pi f_0}{\gamma} \approx \frac{f_0}{f_u - f_d}, \tag{2.1.2}$$

where f_0 is the resonance frequency of the cantilever and f_u, f_d are the frequencies at $A_{max}/\sqrt{2}$ as indicated in figure 2.1.2. A_{max} is the oscillation amplitude of the cantilever at its resonance frequency. At resonance, the energy dissipation per oscillation cycle is E/Q where $E = 1/2c_L A_{max}^2$ denotes the energy stored in the oscillating cantilever. The excitation amplitude $A_{exc} = F_{exc}/c_L$ becomes equal to

$$A_{exc} = \frac{A_{max}}{Q}. \tag{2.1.3}$$

The resonance frequency of the cantilever, in the regime where Hook's law applies, can be calculated from

$$f_0 = \frac{1}{2\pi} \sqrt{\frac{c_L}{m_{eff}}}. \tag{2.1.4}$$

Near the surface of the sample, the vibrating cantilever is influenced by the gradient in z-direction of the interaction force $\partial F/\partial z$. If the force gradient does not vary over the oscillation cycle, the resonance frequency of the perturbed cantilever oscillation f_r can be written as (neglecting the cantilever canting):

$$f_r = \frac{1}{2\pi} \sqrt{\frac{c_L + \frac{\partial F}{\partial z}}{m_{eff}}} = \frac{1}{2\pi} \sqrt{\frac{c_{eff}}{m_{eff}}}, \tag{2.1.5}$$

with c_{eff} being the effective force constant due to the additional tip–sample interaction. The difference in resonance frequency between the free and perturbed cantilever oscillation $\delta f = |f_r - f_0|$ is called *frequency shift*. It is negative for an attractive tip–sample interaction and positive for a repulsive interaction.

The lateral force constant (spring constant) of the cantilever can be calculated from its geometry, dimensions and Young modulus E. For a beam–like cantilever with thickness t, width

w and length l, the spring constant is determined by

$$c_L = \frac{Ew}{4}\left[\frac{t}{l}\right]^3.$$

(2.1.6)

Therefore the spring constant can easily be tuned by adjusting either the width or the length of the cantilever bar. The length of the bar is typically several hundred micrometers [59, 60] whereas the thickness measures only a few micrometers. It is evident, that the force constant of the cantilever is more sensitive for small changes in the thickness of the bar. The fundamental resonance frequency for a beam–like bar with specific density ρ is given by [34]:

$$f_0 = \frac{1.8731^2 t}{4\pi\sqrt{3}l^2}\sqrt{\frac{E}{\rho}},$$

(2.1.7)

with $E=1.25 \cdot 10^{11}$ N/m^2 and $\rho=2.33 \cdot 10^3$ kg/m^3 for a silicon cantilever.

In order to keep the cantilever oscillating at its resonance frequency throughout the whole measurement, the *frequency demodulation technique* first presented by Albrecht *et al.* [35] is used. It exploits the fact that in resonance, the excitation and the oscillation of a freely vibrating cantilever always have a phase difference of exactly 90°. However, if the cantilever vibration is additionally influenced by a spatially varying force field, the phase difference changes, if the driving frequency of the oscillation is kept constant. In order to keep the phase difference exactly at $90\check{r}$, the excitation frequency of the cantilever is continuously adjusted by a feedback loop to match its momentary resonance frequency. The resulting frequency difference between the free resonance frequency f_0 and the momentary resonance frequency f_r is recorded and provides a measure for the tip–sample interaction (*phase locked loop*, PLL). The smallest detectable frequency shift using this technique is limited by the thermal noise of the cantilever [35]:

$$\delta f_{rms} = \frac{1}{A_{osc}}\sqrt{\frac{k_B T B f_0}{\pi Q c_L}}$$

(2.1.8)

Here, T, k_B and B denote the temperature, the Boltzmann constant and the bandwidth of the frequency measurement. Equation 2.1.8 shows that δf_{rms} can be reduced by measuring at low temperatures and with a high quality factor. When going from ambient air pressure to vacuum, Q can be increased by a factor of at least 1000 [36]. Another tunable parameter in equation 2.1.8 is the resonance frequency to spring constant ratio for the cantilevers. It should be as large as possible. This is fulfilled only for micro–mechanical cantilevers. Lastly, the thermal frequency shift noise of the cantilever can be reduced by increasing the oscillation amplitude. However, this will also decrease the measurement sensitivity for sample force with a very small decay length. Therefore an empirical balance has to be found for A_{osc} for each tip–sample feature combination.

In magnetic force microscopy (MFM), the tip is scanned in a plane parallel to the sample tilt at a fixed tip–sample distance. Then, the frequency shift due to the interaction of the magnetic tip and the sample is acquired. The amplitude of the oscillating cantilever is held constant by an additional amplitude feedback loop. In a topography image, contours of constant frequency shift are scanned by adjusting the tip–sample distance with the frequency shift output of the PLL.

2.2   The low temperature scanning force microscope (LTSFM)

The LTSFM is housed inside an ultra high vacuum (UHV) system attached to a cryostat as shown in figure 2.2.3, panel (a). The UHV system consists of three chambers,
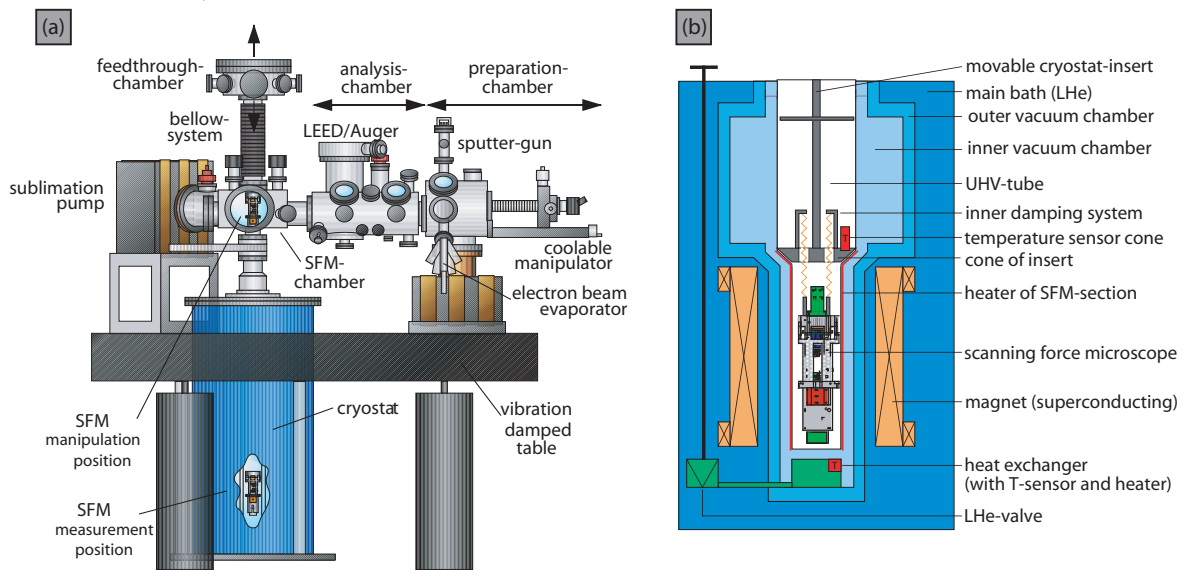
Fig. 2.2.3: Overview of the UHV system containing the LTSFM (panel (a)) and the cryostat (panel (b)). The fast entry air lock is situated on the rear side of the preparation chamber in panel (a). Drawings adapted from [32].
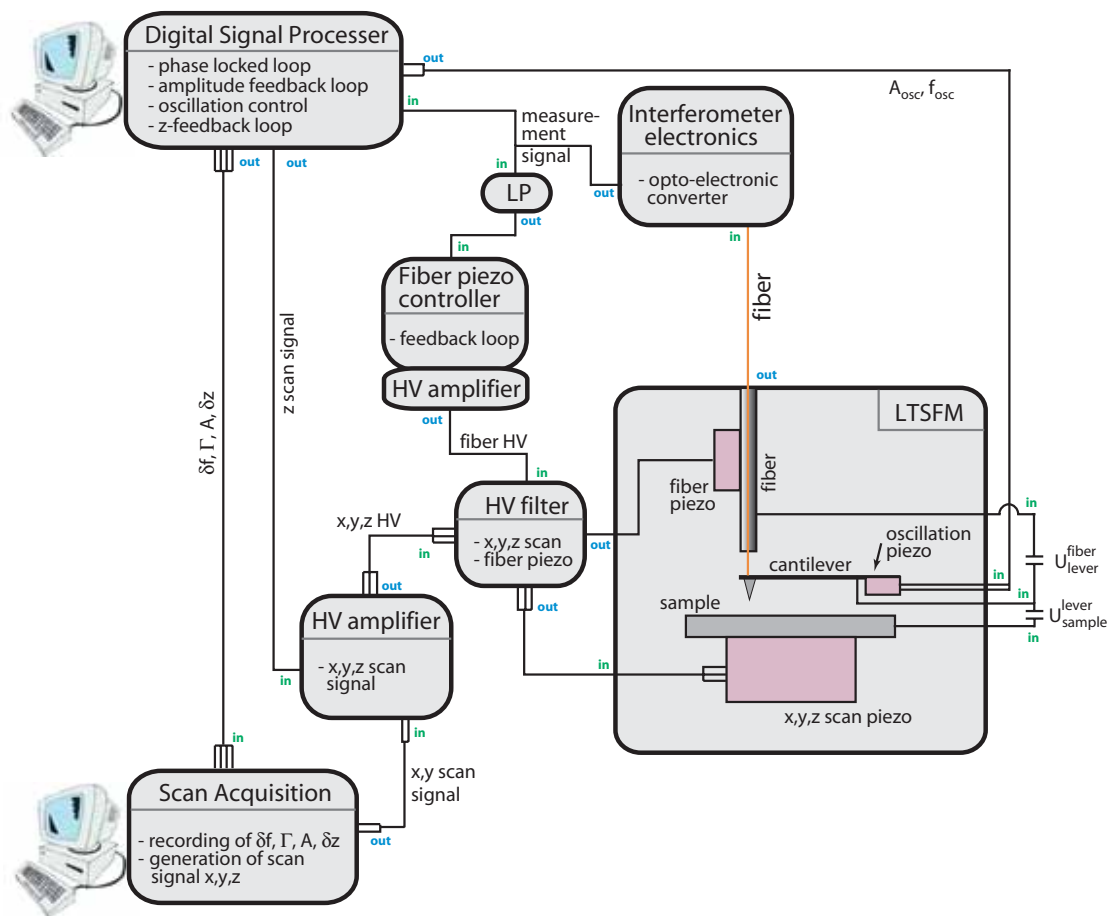

Fig. 2.2.4: Schematic diagram of the LTSFM electronics. Only the electronics needed for the scan motion and the data acquisition are shown.

namely the preparation chamber, the analysis chamber and the microscope chamber itself. The preparation chamber is equipped with a triple e–beam evaporator, a sputter gun and a mass spectrometer. On the rear side of the chamber, a fast entry air lock (not shown) permits a fast exchange of cantilever and samples between UHV and atmosphere. The chamber contains a heatable and coolable manipulator where cantilever and sample holders can be prepared. The stage can be rotated by 360° and moved in x, y and z in order to position the holders for sputtering or evaporation. All cantilevers used in this thesis have been prepared by the e–beam evaporation. The film thickness can be monitored by a quartz microbalance thickness monitor.

The second chamber serves for the analysis of the cantilever and the sample by LEED and Auger electron spectroscopy. A transport system links the two chambers with the microscope chamber. The whole UHV system is mounted on an actively and passively damped table in order to compensate for floor vibrations. The LTSFM is additionally damped in situ by a spring suspension system and eddy current dampers (cf figure 2.2.3, panel (b)). During a measurement, the microscope sits inside the cryostat. For manipulation purposes (exchange of cantilever and sample) it can be moved up into the microscope chamber. The cantilevers and samples are mounted on special holders described in [32] which allows an in situ cantilever and sample change with the help of a mechanical hand. Inside the microscope, the holders sit on special three–point mounts which guarantee stable and reproducible positioning.

Panel (b) shows a schematic drawing of the cryostat's side view. If the LTSFM is in measurement position, the cone mounted on the insert contacts a hollow cone inside the cryostat to allow a constant heat flow in order to cool the microscope. Prior to measurement, the temperature is adjusted to about 8 K. To ensure the stability of the temperature during measurement, a temperature sensor under the sample holder connected to a digital feedback loop and a heater element (*heater SFM-section*) is used. This guarantees a temperature stability of 5 μK. The cryostat also contains a superconducting solenoid that produces a magnetic field of maximum 7.0 T perpendicular to the sample mount[3] (shown in orange in panel (b)). The maximum scan range of the microscope at liquid helium temperature in x, y and z is 6.5 μm $\times$ 6.5 μm $\times$ 1.8 μm.

The scan electronics of the LTSFM are shown in the schematic diagram of figure 2.2.4. The interferometer electronics converts the optical signal into an electronic signal (*measurement signal*) proportional to the laser light intensity. The measurement signal is fed into two inputs: Firstly, it serves as input signal to the feedback controller for the fiber piezo (filtered by a very strong low pass filter) in order to keep the fiber–cantilever distance constant. Secondly, the signal is used as an input to the digital PLL developed by Loppacher *et al.* [38, 37] (*digital signal processor*). The resonance frequency of the cantilever can be measured with a relative accuracy exceeding 1 ppm (parts per million). The digital signal processor comprises not only the phase locked loop but also the amplitude feedback loop, the oscillation control and the tip–sample distance feedback (z-feedback) control used for topography measurements. The oscillation control determines the amplitude and frequency from the output of the amplitude feedback loop and the PLL. The oscillation control drives the oscillation piezo for the cantilever vibration.

The recorded data comprises the frequency shift δf, the amplitude A and dissipation Γ of the cantilever oscillation and the tip–sample distance variation δz. They are transmitted to the acquisition program (*scan acquisition*, SCANIT) developed by Moser [39]. The program also generates the scan motion vectors (x- and y-scan signal). These signals together with the

---

[3]In most cases, the plane of the sample mount is parallel to the surface of the sample.

z-scan signal from the digital signal processor and the fiber feedback loop signal are amplified and fed back to the scan piezo and fiber piezo respectively.

2.3 The high resolution magnetic force microscope (hr-MFM)

The hr-MFM was constructed focussing on increasing the magnetic lateral resolution, imaging sensitivity and measuring throughput. Further to this, easy handling in an industrial environment was important. The microscope was designed and built during this Ph.D. thesis. It is now available from SwissProbe AG [40], a spin-off company of the University of Basel. The whole instrument is depicted in figure 2.3.5, panel (a). The microscope operates at room temperature in a vacuum of $1{\cdot}10^{-7}$ mbar. It is mounted on an active vibration isolation table with an additional internal spring–based vibration isolation.

In order to exchange the cantilever and the sample, the vacuum system has to be vented and the microscope chamber moved away by an electronic lift system (not shown). When the microscope is exposed, the scan head can be rotated away from the sample stage with the aid of a handle. This is depicted in the schematic drawing of the hr-MFM in panel (b). The cantilever holder on the scan head is mounted in the same way as in the LTSFM. The sample stage can accept hard disk platters and full wafers. Furthermore, it features a fast clip mechanism to hold the sample.
The sample can be laterally positioned relative to the cantilever by a coarse positioning system in radial and angular direction (*R,Φ coarse positioning*). Using the R,Φ–system, it can be positioned reproducibly with a relative precision of 100 nm. The sample stage is built on top of the scanner unit which allows a scan range of 12.0 μm × 12.0 μm × 1.6 μm. The cantilever deflection is measured by the same method used in the LTSFM.

The scan electronics of the hr-MFM are shown in the schematic drawing in figure 2.3.6. In analogy to the LTSFM electronics, the optical signal is converted into an electric signal (*measurement signal*) proportional to the laser light intensity using the interferometer electronics. The frequency and the phase shift of the measurement signal are determined in a digital lock-in amplifier and transmitted to a National Instruments Real Time System^{TM}. This system controls the phase locked loop[4], the amplitude feedback loop, the fiber piezo feedback loop, the z–feedback loop, the cantilever oscillation and the scan control. It also generates the bias voltage U_{sample}^{lever}. The x, y and z scan signals as well as the output from the fiber piezo feedback loop are amplified and fed back to the hr-MFM scan piezo and fiber piezo respectively.

The acquisition and visualization of the scan data (δf, A, Γ, δz and the PLL error signal $\delta\theta$) is performed on a separate computer. In addition, the settings of all feedback loops and scan parameters as well as the bias voltage can be adjusted there. All software running on the Real Time System as well as the data acquisition computer is written in Labview^{TM} by Nanonis GmbH [41].

---

[4]Unlike the fully digital PLL running in the LTSFM electronics, this PLL relies on an external lock-in amplifier to determine the frequency and phase of the measurement signal. In addition it needs an external function generator to produce the analogue signal driving the oscillation piezo.
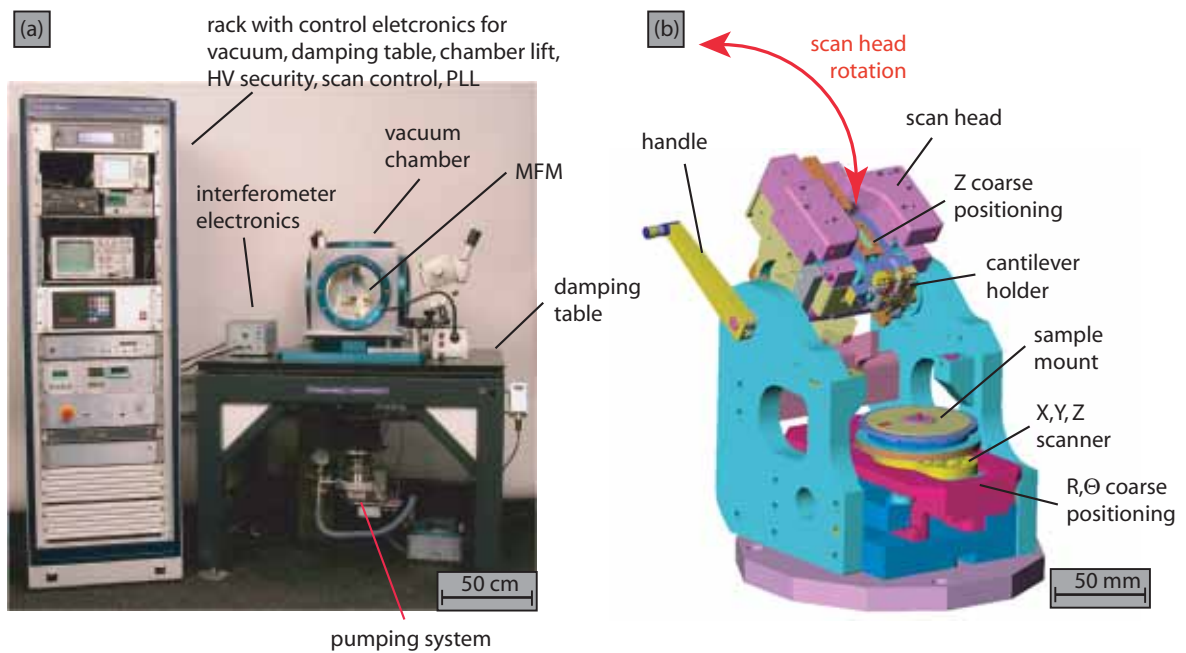
Fig. 2.3.5: The overview of the hr-MFM instrument with the microscope, the vacuum system and the control electronics is depicted in the picture in (panel (a)). A schematic drawing in panel (b) shows the scan head with the cantilever holder and the sample stage with the x,y,z scanner and the R,Φ–coarse positioning system.
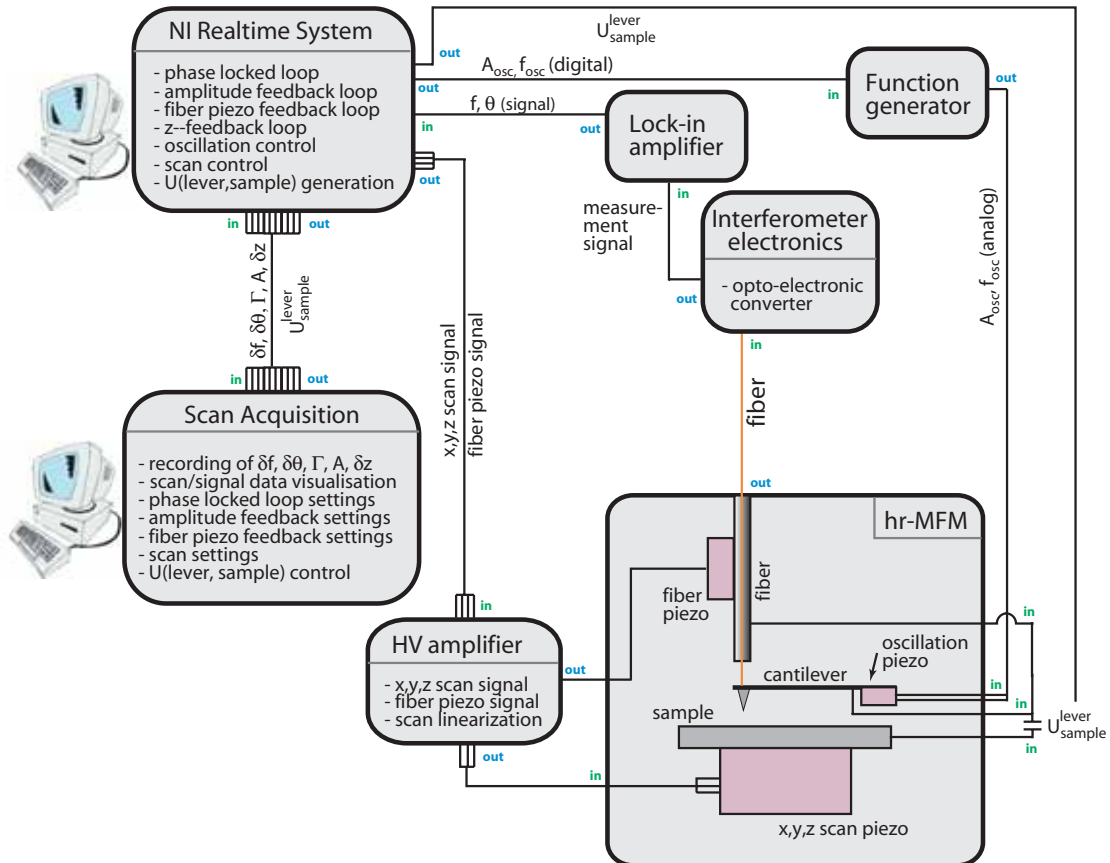

Fig. 2.3.6: Schematic diagram of the hr-MFM electronics. Only the electronics needed for the scan motion and the data acquisition are shown.

Chapter 3

Improvement of methods in MFM

One of the benefits of MFM is the possibility to non–destructively image the stray field of small magnetic structures in real space with high resolution. No sample preparation or decoration is required. In addition, MFM can be used to study the evolution of sample properties in magnetic fields at various temperatures. This is a clear advantage over the Bitter method [42] and Lorentz microscopy [42, 43] which have been widely used before. However in recent years, other real space imaging methods based on electron microscopy, namely photoelectron emission microscopy (PEEM) [10, 11] and scanning electron microscopy with polarization analysis (SEMPA) [12, 13] have been emerging. The new methods have the potential to be equal in resolution to MFM. However, the maintenance costs and complexity of sample preparation and instrument operation has prevented widespread use.

In this chapter, improvements of MFM operational methods and sensors are presented. The scope was set to improve the lateral magnetic resolution and achieve a separation of magnetic and non-magnetic forces. In order to achieve these goals, improved cantilever tips and magnetic coating procedures were developed. In addition, the degradation of the imaging properties of the tips was studied.

3.1 Separation of magnetism and topography in an MFM image

The measurement of a magnetic pattern with high sensitivity and magnetic lateral resolution requires an operation mode in which it is possible to maintain a constant tip–sample distance of typically a few nanometers. This is necessary in order to image very small magnetic wavelengths which have a very small decay length (cf. equation 1.1.8 in chapter 1). At such tip–sample separations, non–magnetic forces like van der Waals or electrostatic forces become comparable to the magnetic force and therefore contribute to the measurement signal (frequency shift). This may lead to artifacts in the MFM images arising from the variation of the non–magnetic tip–sample interactions.

The electrostatic force arising from the different work–functions of the tip and the sample given by

$$F_{el} = \frac{\partial C}{\partial z}(U_{bias} - U_{cp})^2. \tag{3.1.1}$$

Here C is the capacity between the tip and the sample and U_{bias} and U_{cp} denote the voltage across the tip–sample system and the contact potential (CP) respectively. An electrostatic

interaction between the tip and the sample can be avoided if the contact potential is compensated at every measurement position of the scan area.

The van der Waals (vdW) force depends strongly on the geometry of the tip and the tip–sample distance. For a sperical tip for example, the van der Waals (vdW) force arising from the interaction with a flat sample surface is [44, 20]

$$F_{vdW} = \frac{A_H r}{6d^2}, \tag{3.1.2}$$

where A_H is the so called Hamaker constant and r and d denote the tip radius and the tip–sample distance. At distances smaller than 10 nm, the vdW force becomes comparable to the magnetic force. Therefore scanning the tip in a plane parallel to the sample will result in local changes of the tip–sample distance and thus lead to a corresponding change of the vdW force. Topographic features become visible in the MFM image.

A separation of the magnetic and non–magnetic signal in an MFM experiment can be perfomed by modulating either the magnetic or the non–magnetic tip–sample interaction. Schönenberger *et al.* [45] have modulated the contact potential in order to keep the tip–sample separation constant during image acquisition. Other authors have suggested to measure the capacitive force between the tip and the sample separately in order to keep the tip–sample distance constant [46, 47]. Another method, often exploited in commercial MFMs, is the so called *lift mode* in which the local topography of the sample is first measured using the intermittent contact mode. In a second run, the MFM image is acquired using the previously recorded topography data. Although this technique results in two data–sets, the MFM image might not be free from topographic artifacts. These are a consequence of topographical features smaller than the highest achievable magnetic resolution [19].

In this chapter, two methods for the separation of magnetic and non–magnetic contributions in an MFM image are discussed. They consist of a combination of experimental and analysis steps. All measurements have been carried out using the LTSFM microscope in a dynamic non–contact mode[1]. For all samples investigated in this thesis, the CP does not depend on the tip–sample position because the samples have a metallic surface layer. The contact potential can be compensated by a suitable bias voltage prior to the measurement.

The first technique is illustrated in figure 3.1.1. Non–magnetic particles (shown in black) are adsorbed on an in–plane hard disk recording media containing a series of bits. The expected frequency shift signal when scanning a line in constant height mode over the surface is shown below the sketches. In panel (a), the magnetization of the tip is directed towards the sample, resulting in an attractive interaction with the first bit transition and a repulsive interaction with the second transition. In panel (b), the direction of the tip magnetization is changed by 180°, now pointing away from the sample. Consequently, the magnetic interaction at the bit transitions will be opposite (repulsive at the first and attractive at the second transition). The van der Waals interaction is attractive in both configurations of the tip magnetization. Therefore the so called *topographic influence* is cancelled out from an MFM measurement, if two scans with opposite tip magnetization are subtracted from each other; the sole magnetic signal results. Conversely, adding the two images will result in the topographic influence. However, this technique is only applicable if the modifications of the tip and the sample were negligible in both measurements (a) and (b).

Figure 3.1.2 shows an experiment using this technique. The images in panels (a) and (b) show

---

[1]The MFM images were taken in constant height mode in which a plane parallel to the sample tilt is scanned. The topography measurements were taken in the so called constant interaction mode where the tip follows a contour of constant frequency shift by a continuous adjustment of the local tip–sample distance.
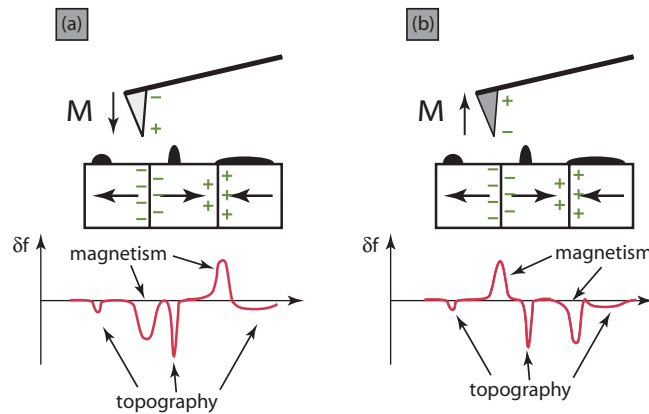
Fig. 3.1.1: Separation of topography and magnetism in an MFM measurement (first technique): Two MFM scans over the same sample area, once with the tip magnetization towards the sample (panel (a)), once away from the sample (panel (b)) are depicted. By rotating the tip magnetization direction by 180°, the MFM contrast in the line scan shown below the sketches inverses, however, the vdW contrast stays the same, due to the attractive nature of the vdW interaction independent of the tip magnetization.

a single bit transition on an in–plane hard disk material taken at the same horizontal and vertical scan position. The first image was taken with the tip magnetization direction towards the sample, the second one with the tip magnetization directed away from the sample.

The black spots in panel (b) (arrows one and two), for example, may result from an attractive magnetic or van der Waals interaction (see arrows one and two). In order to clarify this, the difference between the images in panels (a) and (b) can be computed resulting in a magnetic image free from topographical artifacts (panel (c)). If the two images are added, the topographic influence is revealed as shown in panel (d). The highest topographic features are imaged as black spots indicating a large decreases of the frequency shift due to a strong attractive van der Waals interaction.

The black spot indicated by arrow one in panel (b) is due to magnetic interaction, whereas the back spot indicated by arrow two originates from the vdW interaction between the tip and the sample.

A qualitative comparison of the topography influence in panel (d) can be performed with a topography measurement acquired in constant frequency shift mode shown in panel (f). The tip–sample distance for such a measurement is very small, typically less than 3 nm. In this regime, the van der Waals force is much larger than the magnetic force and the acquired image will only represent the local topography. Note that the largest vdW interaction signal is depicted as black spots in panel (d) which correspond to the highest elevations in panel (f) (white spots). In order to compare panel (d) and (f) it is instructive to invert the topography influence image (panel (e)).

Although delivering convincing results, the technique presented above imposes some difficulties in the experimental procedure. The magnitude of the magnetic field needed to flip the tip magnetization by 180° is large, up to 2.0 T. Such a high field would damage most magnetic samples irreversibly. Therefore the sample has to be removed from the microscope while the tip is remagnetized (in the LTSFM system) or the cantilever and sample stages have to be separated by at least a few centimeters (in the hr-MFM). The difficulty of the procedure lies in the precision with which the sample has to be reintroduced into the microscope (LTSFM) or the cantilever and sample stages have to be readjusted (hr-MFM). Both the magnetic and vdW forces depend strongly on the tip–sample distance, thus make it necessary to acquire the
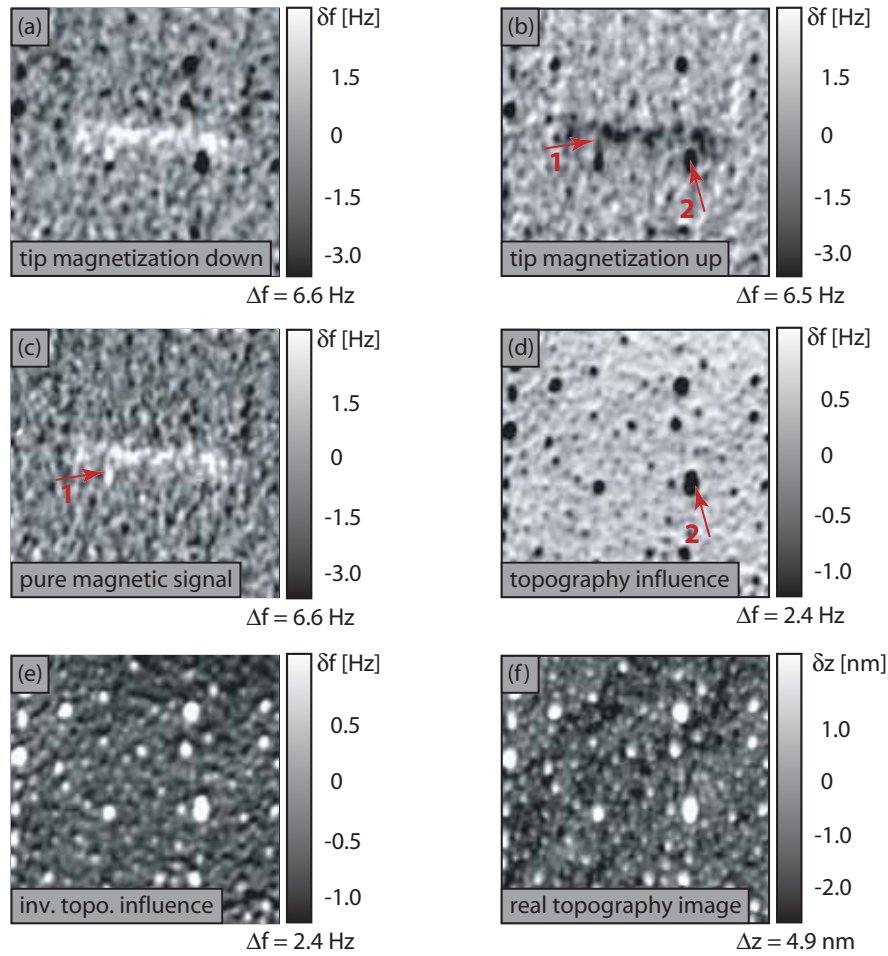
Fig. 3.1.2: Separation of topography and magnetism in an MFM measurement (first technique):
Two MFM images as explained above are taken (panels (a) and (b)). If the lateral and vertical
position of the two scans are identical, the difference of these two images reveals the sole magnetic
signal (panel (c)) and a summation the topographic influence (panel (d)). When comparing the
topographic influence with a real topography scan done in constant frequency shift mode (panel
(f)), it is instructive to invert the image from panel (d) for a better comparison (panel (e)). All
images are 0.5 μm $\times$ 0.5 μm in size.

two MFM images not only at the same lateral sample position, but also at exactly the same
tip–sample separation in order to make them comparable. While this experimental procedure
can be performed with a lateral accuracy of less than 500 nm and 250 nm in the LTSFM and
hr-MFM instrument respectively, the precision of these macroscopic mechanical operations
exceed the scan range of most MFMs. Therefore recovering the original scan area might not
be possible in other MFMs.
In addition, the changed tip magnetization can also influence the sample and lead to non–
identical MFM measurement conditions as reported by Foss *et al.* on Fe_2O_3 [8].

The second technique circumvents the experimental difficulties of the first technique. No
remagnetization of the tip is required. Figure 3.1.3 illustrates the experimental procedure.
First an MFM image is acquired in constant height mode, in analogy to the first technique
(cf. panel (a)). Again the image reflects a convolution between magnetic and van der Waals
forces as shown in the expected frequency shift signal below the sketch. In a second step, a
true topography measurement of the sample surface is measured in a non–contact constant
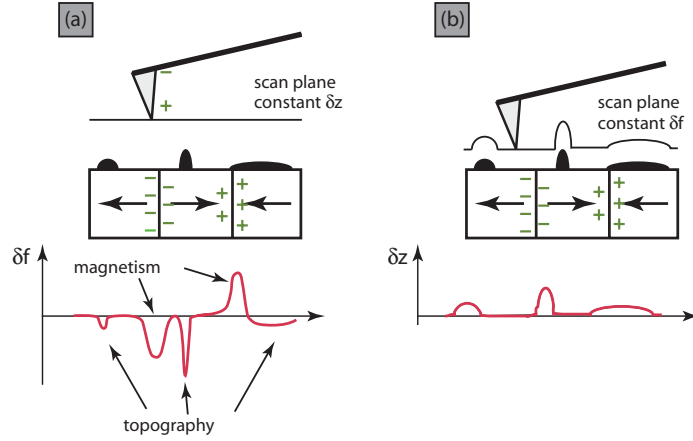
Fig. 3.1.3: Separation of topography and magnetism in an MFM measurement (second technique): Panel (a) shows an MFM measurement at constant height at a known tip–sample distance. The magnetic signal as well as the topographic artifacts are visible in the image. Panel (b) shows a true topography measurement taken at constant frequency shift mode very close to the sample. Only the van der Waals interaction is visible.

frequency shift scan mode at a very small tip–sample distance, typically less than 3 nm. In this regime, the van der Waals force is much larger than the magnetic force and the acquired image will only represent the local topography. If the geometry of the tip is known, it is possible to calculate the topographic influence at the tip–sample separation of the MFM image. Subtracting the calculated image from the MFM measurement will reveal the sole magnetic signal.

Figure 3.1.4 shows an experiment following this technique. The MFM image in panel (a) was taken at a tip–sample distance of 9.7 nm, the topography scan was acquired at a tip–sample separation of 1.8 nm. The calculated influence of the van der Waals interaction at the tip–sample distance of the MFM image is depicted in panel (c). Finally panel (d) depicts the sole magnetic image calculated by taking the difference between the MFM image in panel (a) and the topographic influence in panel (c).

In order to calculate the topography influence in the MFM image, it is necessary to determine the geometry of the tip. For this, frequency shift versus tip–sample distance (δf-z) spectroscopy data can be used [48, 49, 50, 51]. In such a spectroscopy measurement, the tip is approached to the sample surface, until the energy needed to maintain a certain oscillation amplitude of the cantilever exceeds a preset limit[2]. Then, the cantilever is retracted. The parallel recorded frequency shift (δf) data can be fitted with a function describing the vdW interaction between the tip and the sample surface. Several authors [52, 48, 49, 53] have found functions for various tip geometries. For a pyramidal, conical, parabolic and spherical tip geometry, the van der Waals interaction with a plane surface is given by:

$$F_{pyr}^{vdW}(z) = -\frac{2A_H tan^2(\alpha/2)}{3\pi}\left(\frac{1}{z} - \frac{1}{z+h} - \frac{h}{(z+h)^2} - \frac{h^2}{(z+h)^3}\right), \qquad (3.1.3)$$

$$F_{con}^{vdW}(z) = -\frac{A_H tan^2(\alpha/2)}{6}\left(\frac{1}{z} - \frac{1}{z+h} - \frac{h}{(z+h)^2} - \frac{h^2}{(z+h)^3}\right), \qquad (3.1.4)$$

$$F_{para}^{vdW}(z) = -\frac{A_H r}{6}\left(\frac{1}{z^2} - \frac{1}{(z+h)^2} - \frac{2h}{(z+h)^3}\right), \qquad (3.1.5)$$

---

[2]When the tip is in very close proximity of the sample oscillation energy is dissipated into the sample. This happens at tip–sample distance of typically less than 5Å.
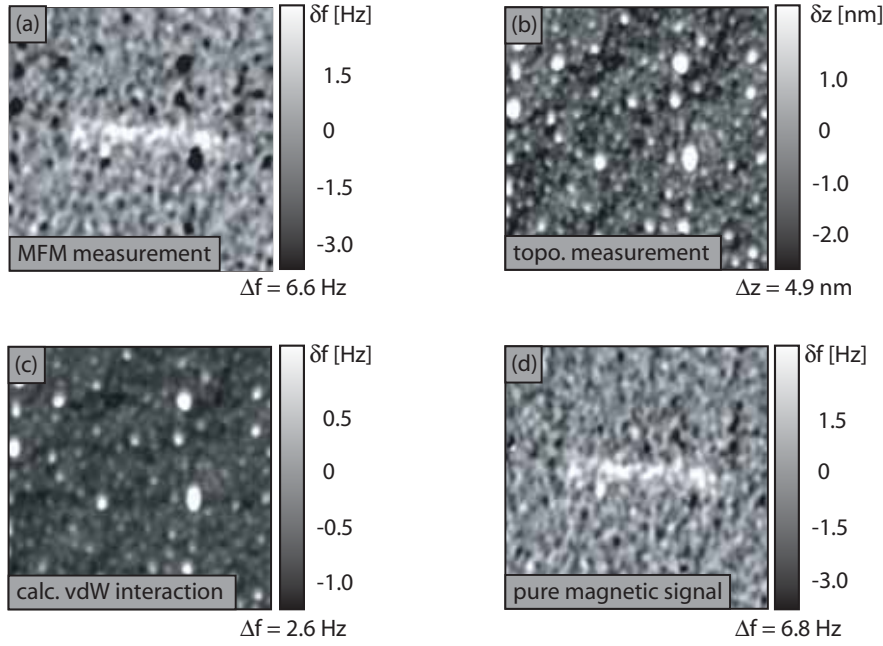
Fig. 3.1.4: Separation of topography and magnetism in an MFM measurement (second technique): An MFM image is taken at a given but known tip–sample distance in constant height mode (panel (a)). Then, a topography image in constant frequency shift mode is taken at a smaller tip–sample distance shown in panel (b). Panel (c) shows the topographic influence at the tip–sample separation of the MFM image in panel (a). Finally panel (d) depicts the sole magnetic image calculated by taking the difference between the MFM image in panel (a) and the topographic influence in panel (c). All images are 0.5 μm $\times$ 0.5 μm in size.

$$F_{sph}^{vdW}(z) = -\frac{A_H r}{6}\Big[\frac{1}{z^2} + \frac{1}{(z+h)^2} - \frac{2}{h}\Big(\frac{1}{z} - \frac{1}{z+h}\Big)\Big]. \tag{3.1.6}$$

Here α is the full tip cone angle, r the radius of the tip apex and h denotes the height of the tip. The van der Waals force can be converted into a frequency shift δf using

$$\delta f = -\frac{f_0}{2\pi a c_L}\int_0^{2\pi} F_{ts}^{vdW}(z + a\cos\varphi)\cos\varphi\, d\varphi, \tag{3.1.7}$$

where f_0, c_L and a denote the free resonance frequency, the spring constant of the cantilever and its oscillation amplitude respectively. The resulting frequency shift for a pyramidal, conical, parabolic and spherical tip geometry can be written as:

$$\delta f_{pyr}^{vdW}(z) = \frac{f_0}{2\pi a c_L}\Big[-\frac{2A_H tan^2(\alpha/2)}{3\pi}(I_1(z,a) - I_1(z+h,a) \tag{3.1.8}$$
$$-hI_2(z+h,a) - h^2 I_3(z+h,a))\Big],$$

$$\delta f_{con}^{vdW}(z) = \frac{f_0}{2\pi a c_L}\Big[-\frac{A_H tan^2(\alpha/2)}{6}(I_1(z,a) - I_1(z+h,a) \tag{3.1.9}$$
$$-hI_2(z+h,a) - h^2 I_3(z+h,a))\Big],$$

$$\delta f_{para}^{vdW}(z) = \frac{f_0}{2\pi a c_L}\Big[-\frac{A_H r}{6}(I_2(z,a) - I_2(z+h,a) \tag{3.1.10}$$
$$-2hI_3(z+h,a))\Big],$$

$$\delta f_{sph}^{vdW}(z) = \frac{f_0}{2\pi a c_L}\Big[-\frac{A_H r}{6}(I_2(z,a) + I_2(z+h,a) \tag{3.1.11}$$

$$-\frac{2}{h}\big[I_1(z,a) - I_1(z+h,a)\big]\big)\Big]$$

with $I_n(z,a)$ $(n = 1..3)$ being

$$I_n(z,a) = \begin{cases} \frac{2\pi}{a}\left(1 - \frac{z}{\sqrt{z^2-a^2}}\right) & (n=1) \\ \frac{(-1)^n}{(n-1)!}\left(-\frac{2\pi a}{(z^2-a^2)^{3/2}}\right)^{n-2} & (n \geq 2) \end{cases} \qquad (3.1.12)$$

In order to cancel out the magnetic interaction between the tip and the sample for distances larger than a few nanometers, two δf-z measurements are typically performed. The first data–set is taken over a domain with an alignment of the magnetization direction anti–parallel to the one of the tip (repulsive domain). The second data–set is recorded over a domain with a parallel alignment of the magnetization and the tip magnetization (attractive domain). It is important that the local topography at the lateral position of the two spectroscopy measurements is comparable. The best lateral positions for the two spectroscopy measurements can be identified from the previously recorded topography image. In a subsequent averaging of the two δf-z data–sets, only the influence of the magnetic interaction is cancelled out. The experiment was performed with a Team Nanotec ISC^{TM} cantilever (see figure 3.2.8,
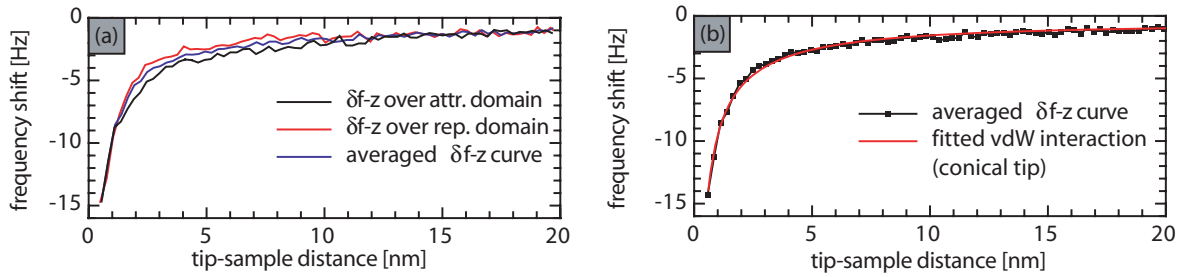

Fig. 3.1.5: Calculation of the tip parameters using the conical tip model. Panel (a) shows a frequency shift–distance curve over a repulsive and attractive domain as black and red lines, the average of the two as blue line. Panel (b) depicts the averaged frequency shift–distance curve and a fit of the vdW interaction using a cone–liked tip model, a resonance frequency of 55500 Hz, spring constant 0.3 N/m and oscillation amplitude of 5 nm. The Hamaker constant and the cone angle were computed to be $A_H = 1.9 \cdot 10^{-20}$ J and $\alpha = 9.2^o$ respectively.

panel (d)). Therefore, a cone–shaped tip was assumed for the fit. Figure 3.1.5, panel (a) depicts a δf-z curve taken on a repulsive domain, attractive domain and the averaged δf-z curve as solid black, red and blue line respectively. Panel (b) shows the averaged frequency shift–distance curve in black and a fit according to 3.1.8 for a cantilever with a conical tip, a resonance frequency of 55500 Hz, spring constant 0.3 N/m and oscillation amplitude of 5 nm. The resulting parameters of the fit were $A_H = 1.9 \cdot 10^{-20}$ J for the Hamaker constant and $\alpha = 9.2^o$ for the full cone angle. The fit is in very good agreement with the data–set.

In figure 3.1.6, the results of the two topography–magnetism separation techniques are compared. Panels (a) and (b) show the sole magnetic signal from the MFM images as computed by technique one and two, respectively. The contrast range is almost equal. However, some areas differ, e.g. the spots marked by the blue circles. The black spots inside the circles are clearly larger in panel (b) than in panel (a). A comparison with the MFM measurement in panel (a) of figure 3.1.2 reveals that in these areas, a large vdW interaction was superimposed on the magnetic interaction. With the first technique, this topographic influence was completely removed. However, using the second technique, parts of the vdW interaction signal remained. This is also visible in the line sections (marked areas in panel (c)) taken along
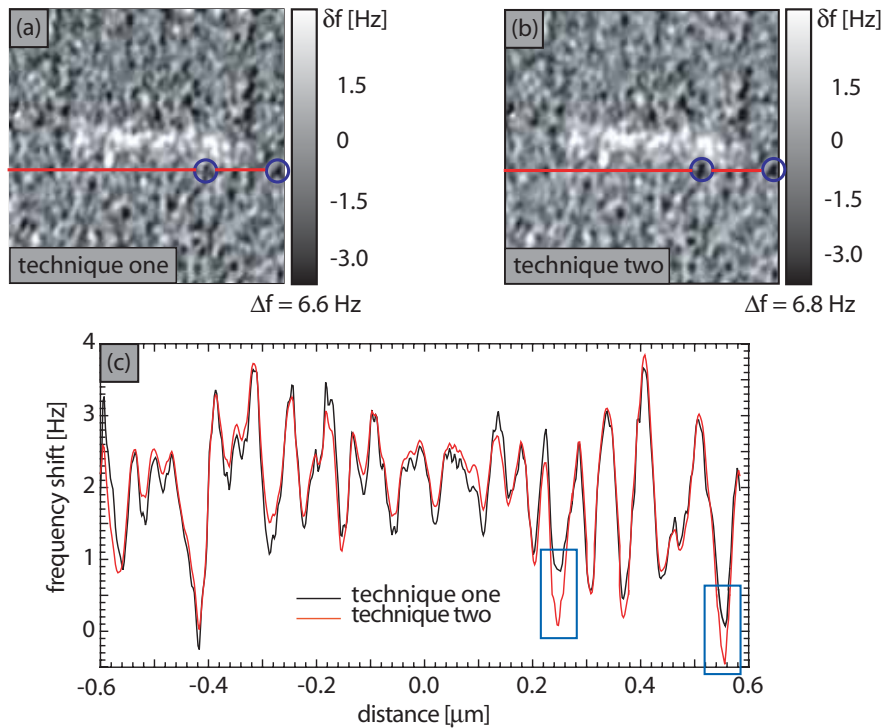
Fig. 3.1.6: Comparison of the two topography–magnetism separation techniques. Panel (a) shows the sole magnetic signal as derived by technique one, panel (b) as computed from technique two. The blue circles show a spot in the image were the topographic influence was compensated differently with the two techniques. Panel (c) shows a line scan taken at the red lines in panels (a) and (b). At the areas indicated by blue boxes, the difference is visible.

the lines indicated in panels (a) and (b). A possible reason is that the topographic influence calculated from the topography image is not equal to the topographic influence in the MFM measurement. This may be due to a change in the tip geometry resulting from a hard physical contact between the tip and a particle on the surface in the time between the measurement of the MFM image and the topography image.

3.2 Study of imaging properties of high resolution MFM cantilevers

Magnetic force microscopy is technologically important for imaging magnetization patterns with high resolution and minimal sample preparation. As such, it has always been an analysis tool in the hard disk manufacturing industry. However, magnetic forces have a very large decay length, unlike for example van der Waals forces in AFM. The lateral magnetic resolution in an MFM experiment depends strongly on the whole tip geometry. This geometry is characterized by the radius of curvature of the apex, the half cone angle of the taper as well as the tip length, the aspect ratio and tip-sample spacing [6]. For example, a high aspect ratio of the tip helps to minimize the influence of unwanted long range interactions due to electrostatic and van der Waals forces.

In order to achieve high lateral magnetic resolution of the order of 20 nm and smaller, considerable effort was made to optimize the cantilever tip geometry, magnetic coating and fabrication. Complex serial cantilever fabrication techniques were used to achieve an improved cantilever

preparation. This involved lithographic processes resulting in nm–sized Ni dots on the apex of pyramidal shaped Si–tips [54] and growth of a carbon nanotube with a nickel particle on top of a Si cantilever [55]. Folks *et al.* have used field ion beam milling (FIB) to perforate the apex of a commercial MFM tip [56] and thereby, they created a magnetic dipole at the end of the tip. Liu *et al.* [57] and Wua *et al.* [58] used FIB to first trim the apex of a commercial cantilever tip. Then they coated the tip with a ferromagnetic (FM)/Ru/FM system with antiferromagnetic (AF) coupling and a FM/AF system respectively. Other authors have used field electron beam deposition of magnetic material on the apex of commercial Si–tips [61, 62]. Despite the frequently reported increase of measurement sensitivity in the imaging of magnetization patterns in general, the lateral magnetic resolution is far from the goal of 20 nm resolution. The best values were reported by Utke *et al.* who claimed a 40 nm magnetic resolution with their FEB deposited Co–nanorod super–tips [62].

A drawback of all methods is the small throughput of tip fabrication due to the serial methods used. Ideally, MFM cantilevers should be easy to fabricate in large quantities which involves the usage of parallel methods like sputtering or thermal evaporation of the magnetic layer(s). In addition, the tips should be sensitive even for small magnetic wavelengths in order to image even smallest magnetic objects with a satisfactory signal to noise ratio.

In this chapter, the magnetic imaging properties of three groups of cantilever was investigated and compared. The first group contained pyramidal shaped Nanoworld Pointprobe^{TM} Si cantilever (further denoted by *PP*) [59]. The second group comprised cone–shaped Si cantilevers from Team Nanotec [60]. Two types were tested: SC^{TM} and ISC^{TM} cantilevers (further denoted by *SC* and *ISC*). All tips from the first two groups were coated by inclined thermal evaporation in UHV from one side of the taper, usually the side facing the cantilever chip (backside), with a 2 nm palladium and a 4 nm cobalt layer. The evaporation method is explained in detail in [9, 17]. The last group in this test were cantilevers fabricated by Utke *et al.* by FEB deposition of Co–rods [62].

Each tip was magnetized along the tip axes in a 2.0 T field, then an image of 5×5 μm with 512×512 pts as well as an image of 1.5×1.5 μm with 256×256 pts was taken on the calibration sample from Seagate Research Center. All measurements were performed with the low temperature microscope SFM described in chapter 2.3.
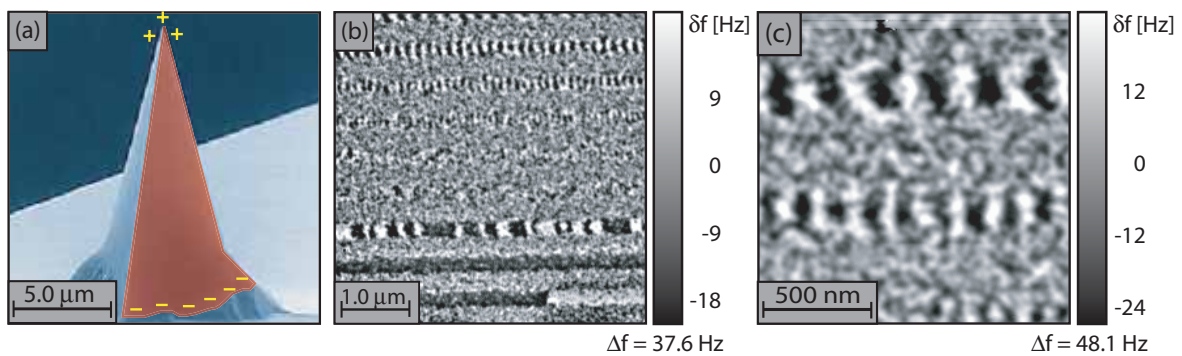

Fig. 3.2.7: SEM image (panel (a)) and typical MFM images of the Nanoworld PP tip. Panel (c) shows a zoom on two of the tracks in panel (b). The geometry of the magnetic layer is depicted in panel (a) by the red surface.

Figure 3.2.7, panel (a) shows a scanning electron microscope (SEM) image of a typical Nanoworld PP cantilever. The shape is pyramidal with three side faces. The cantilever tip has a length of 10 μm to 15 μm, an apex radius of less than 20 nm and a half cone angle of less than 15°. The aspect ratio of the tips is typically less than 1:10. Coating this kind of

tip from one side will at least cover a whole facet of the taper and create a magnetic film of extended geometry [14] as shown in red in panel (a). Consequently, the distribution of the magnetic charges at the top and bottom of the taper will be broad. Panels (b) and (c) show an overview image and a zoom measurement on the calibration sample from Seagate Resarch Center.
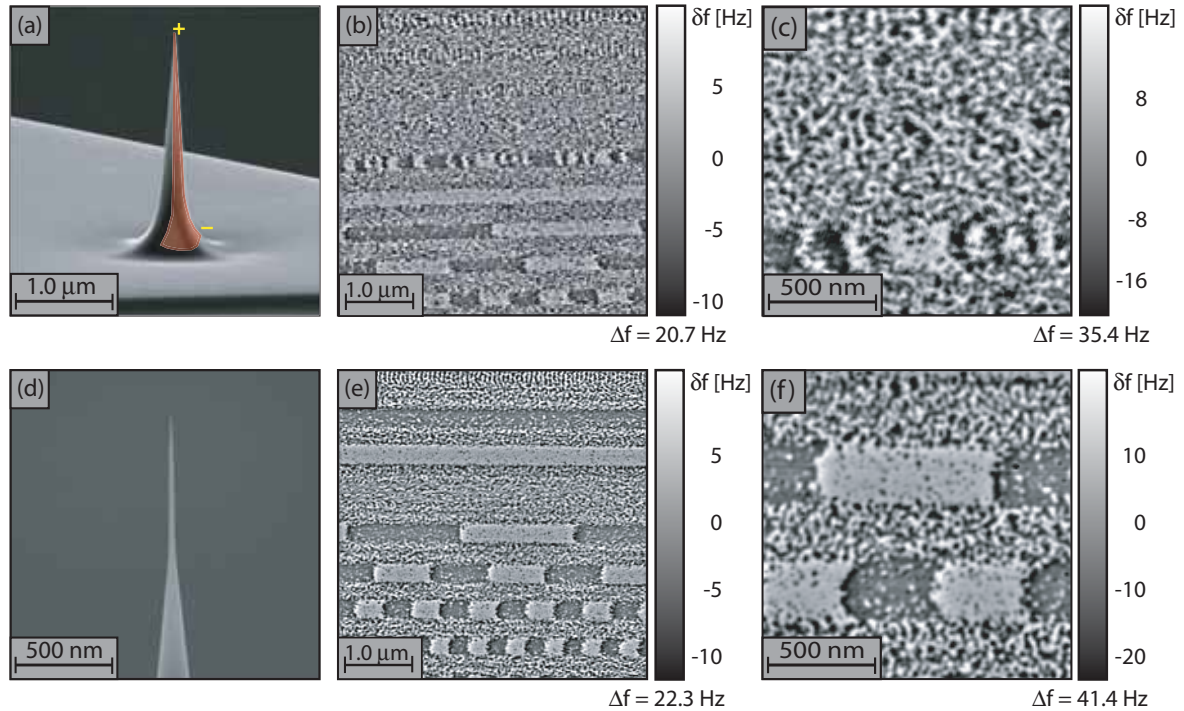

Fig. 3.2.8: SEM images (panels (a) and (d)) and typical MFM images of the Team Nanotec SC and ISC tips. Panels (c) and (f) show zooms on two of the tracks in panels (b and e)). The geometry of the magnetic layer is depicted in panel (a) by the red surface.

Figure 3.2.8, panel (a) shows a SEM image of a typical Team Nanotec SC cantilever. The shape is cone–like with a length of about 10 μm and a high aspect ratio of 1:20 to 1:50. The apex diameter is less than 15 nm and the full opening angle of the cone less than 15°. Panel (d) shows a SEM image of a typical Team Nanotec ISC cantilever. The shape is also cone–like with a length of about 10 μm, but it has a higher aspect ratio of 1:50 to 1:70. The apex diameter is less than 7 nm and the full opening angle of the cone less than 8°. Coating these tips from one side as explained above, results in a very narrow, almost line–like magnetic film along the taper of the tip as indicated in red in panel (a). Thus the magnetization inside this layer will point along the cone of the tip, the nucleation of a domain wall or the formation of a magnetic vortex are not possible [14]. The magnetic charge is confined to the upper and lower end of the layer, approximately forming a probing dipole for large magnetic wavelengths and a monopole for small wavelengths. Panels (b), (c) and (e), (f) show overview images and zooms on the calibration sample from Seagate Resarch Center.

Figure 3.2.9, panels (a) and (d) show SEM images of the tip end and the taper of MFM tips produced by Utke *et al.* They deposited a cobalt rich amorphous carbon matrix on top of a conventional Nanoworld PP cantilever by field electron beam (FEB) deposition. By moving the focus of the beam, they managed to built a rod–like structure on the apex of the Si–tip. The cobalt arranged itself in 2 nm to 5 nm sized Co-particles in a cubic ferromagnetic phase. The rods have a width of 40 nm to 80 nm and a length of 0.5 μm to 2.0 μm, resulting in
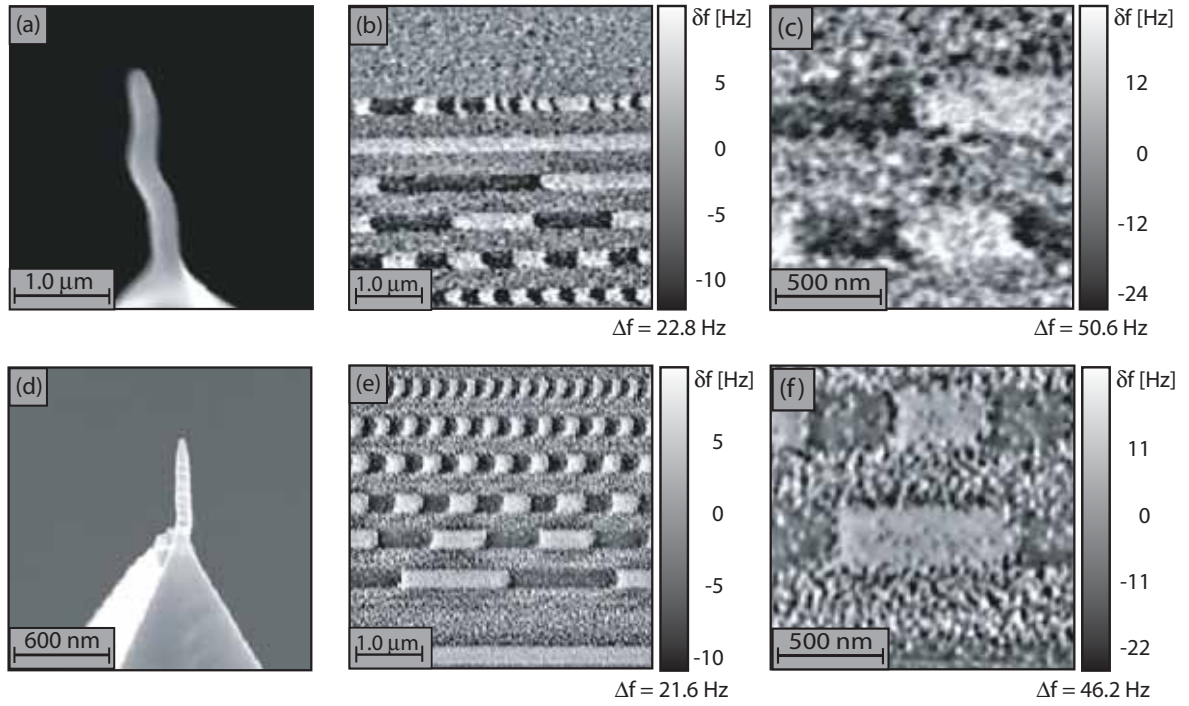
Fig. 3.2.9: SEM images (panels (a) and (d)) of the tip end and typical MFM images of the cantilevers produced by Utke *et al.* In the remainder of this chapter, the tip shown in panel (a) is called tip No1 and the one depicted in panel (d) tip No2. Panels (c) and (f) show zooms on two of the tracks in panels (b) and (e).

a high aspect ratio. However, the FEB deposition was not easy to control which sometimes resulted in crooked rods (panel (a)). In the remainder of this chapter, the tip shown in panel (a) is called *tip No1* and the one depicted in panel (d) *tip No2*. Panels (c) and (f) show zooms on two of the tracks in panels (b) and (e).

In an MFM measurement, the resulting image is a convolution of the sample stray field and the magnetization of the tip (cf. chapter 1.2). In order to carry out a quantitative comparison of the imaging properties of the cantilevers, the tip transfer function must be extracted. This is achieved using the cantilever calibration process described in chapter 1.3. After computing the tip transfer functions, their Fourier spectra can be compared. This is done by averaging the frequency components of different directions but same wave-vector k as described in [9, 17]. The averaged frequency components can be plotted and compared as a function of the wave number. The resulting spectrum is called a *sensitivity spectrum*. Figure 3.2.10, panel (a) depicts the result for all tested cantilevers.

The colour coded curves represent the various tips as shown in the key of figure 3.2.10. Values taken from the curve for a certain tip, show the magnetic imaging sensitivity for a given wave-vector k. k corresponds to a spatial wavelength λ of a magnetization pattern by $\lambda = 2\pi/k$. The spatial wavelength is related to a measurable magnetic resolution by $\lambda_r = \lambda/2$. In the ideal case of a monopole configuration of the magnetic charges $q_{tip}(\mathbf{k}) = q_0$, all magnetic wave vectors are imaged with equal sensitivity. The sensitivity function in this ideal case would resemble a horizontal line in figure 3.2.10. A gradual decrease of the Fourier component values with increasing k approximately represents a monopole imaging behaviour of the magnetic tip.

The two Team Nanotec cantilevers have best imaging sensitivity for magnetic wavelengths
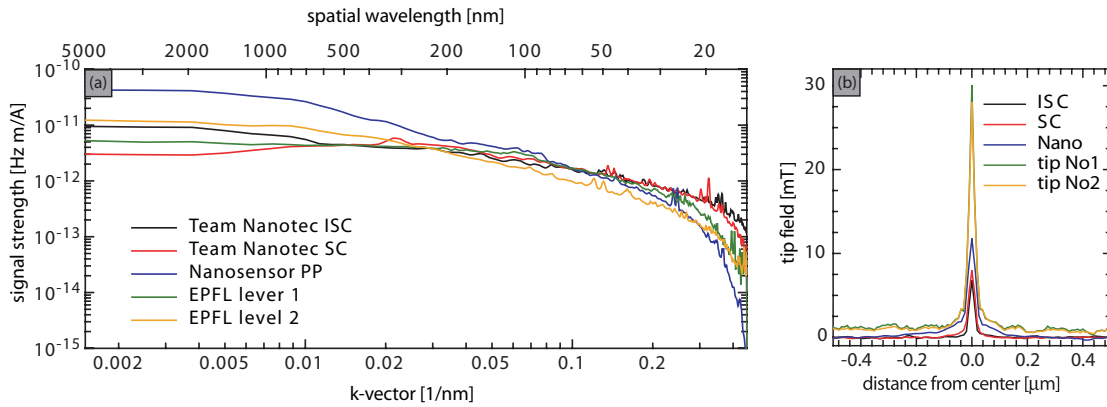
Fig. 3.2.10: Sensitivity spectrum of the tip transfer functions (panel (a)) and tip stray field cross sections of the tip stray field distribution (panel (b)) of the tested cantilevers. The black, red, blue, yellow and green curves denote the ISC, SC, PP, tip No1 and tip No2 from Utke *et al.*, respectively.

smaller than 100 nm. They only diverge at 38.5 nm. For smaller wavelengths, the ISC tip exhibits a gentle curve slope while the SC tip curve decreases more steeply. The PP tip has the worst imaging properties: Already at a magnetic wavelength of 40 nm, it is a factor of 4 worse than the Team Nanotec tips, at 30 nm the curves differ by an order of magnitude. The imaging properties of the two cantilevers from Utke *et al.* lie in between those of the Team Nanotec and Nanoworld levers. Tip No1 shows the worst imaging sensitivity for magentic wavelengths down to 40 nm. Beyond this, it images better than the PP tip, but is still a factor of 5 worse than the ISC cantilever. Tip No2 has slightly better imaging properties comparable to the Team Nanotec levers down to a magnetic wavelength of 50 nm, but then the yellow curve falls off more rapidly and meets the green curve.

Panel (b) in figure 3.2.10 shows cross sections of the cantilever stray field distributions in a plane touching the apex of the tip, computed from the tip transfer functions. Three groups can be identified corresponding to the three groups of cantilever tested. The two Team Nanotec cantilevers have a weak field of less than 8.1 mT and the field distribution is very confined around the center axes of the taper with a full width at half maximum (FWHM) of 26.3 nm. The PP cantilever shows a higher field of almost 12 mT. In addition, the FWHM is larger (42.5 nm) than for the SC and ISC tips. This might be due to the broader geometry of the magnetic layer of the PP tip which usually covers at least one facet of the pyramidal taper. Tips No1 and No2 from Utke *et al.* have the highest fields of 24.1 mT and 30.4 mT, reflecting the amount of magnetic material in the rods. The field distribution is also very confined around the vertical axes of the taper, the FWHM being only slightly larger (34.2 nm for tip No1 and 29.8 nm for tip No2) for the Team Nanotec cantilevers.

In order to obtain high lateral magnetic resolution in an MFM experiment, the magnetic flux should be large in a small area close to the apex of the tip. On the other hand, the magnetization should be fixed and the magnetic flux emanating from the tip should be small enough to prevent non–negligible modifications of the sample. The analysis of figure 3.2.10 panel (a) and (b) reveals that the Team Nanotec cantilevers together with the coating procedure [9, 17] are most suited for high resolution MFM. Their imaging properties are best, especially for small magnetic wavelengths, being almost an order of magnitude better than the tips from Utke *et al.* for a wavelength of 28 nm. In addition, the stray field of the tips is very small, so non-negligible modifications of hard magnetic samples will be unlikely. The Nanoworld cantilever has the least good imaging properties. The imaging sensitivity for a magnetic wavelength of 28 nm is more than two orders of magnitude weaker than for the Team Nanotec tips. The

Co-rich rod–like tips from Utke *et al.* show intermediate imaging properties. The tips seem to have a confined magnetic flux at the tip apex. However their stray fields are large and could influence the sample non–negligibly. The slightly worse imaging properties of the tip No1 could arise from the bending of its Co-rod but could also be caused by the larger rod diameter.

3.3   Imaging degradation study of cantilever tips and coating

Two of the key factors for hr-MFM are the geometry of the tip and its magnetic coating. In operation, the tip–sample forces arising from an accidental or intentional physical contact between the tip and the sample, may damage the tip apex and its magnetic coating. In this chapter, the degradation of the imaging properties of MFM tips with various geometry are quantified. The degradations may arise from common experimental scan–modes and accidental cantilever–sample interactions. The following experimental procedures were performed with a Team Nanotec SC^{TM}, Team Nanotec ISC^{TM} and a Nanoworld PP^{TM} tip. In the remainder of this section, the cantilevers are denoted *SC*, *ISC* and *PP* respectively.

1. When the MFM is operated in a true non–contact operation mode, the energy dissipated from the oscillating cantilever can be limited to avoid an accidental contact of the tip with the sample. This is usually achieved by retracting the tip to a safe distance from the sample when the dissipation exceeds a preset limit (dissipation security). In this test, the limit was set to 1.5× the value required to maintain a constant amplitude of the free oscillating cantilever. This configuration is usually used in high resolution MFM.

2. The MFM was again operated in a true non–contact mode, but the excitation limit of the dissipation security was set to 3× the energy needed to maintain a constant amplitude of the free oscillating cantilever.

3. MFM measurements with a high lateral resolution require that the tip is initially approached from a macroscopic distance to a tip–sample separation of around 10 nm. The last part of the approach, when the tip–sample distance is reduced from a few 100 nm down to 10 nm is critical, because the interaction forces at distances above a few tens of nanometers are extremely small. Assuming that electrostatic and magnetic forces can be neglected, the tip–sample interaction is due to van der Waals (vdW) forces. VdW forces between sharp tips and samples were investigated by various groups, e.g. Lantz *et al.* [50, 51]. The authors found that the vdW force, F_{vdW} varies with the tip–sample separation, z, as

$$F_{vdW} = \frac{C}{z^2}, \tag{3.3.13}$$

   for a conical tip geometry and a plane surface. At $z =$1 nm, a force of approximately 0.1 nN is expected [50], therefore the constant C can be calculated. For a tip–sample distance of 10 nm an equivalent force of 1 pN is found. By computing the force gradient dF/dz of equation 3.3.13 and using $\Delta f = -f_0/2c_L \cdot dF/dz$, a frequency shift of 3 Hz is expected for a cantilever with a spring constant of 1.0 N/m and a resonance frequency of 30 kHz. However, a further decrease in z of only 1-2 nm, increases the interaction force and therefore the frequency shift dramatically, due to the slope of the vdW curve for small tip–sample separations [51]. Due to the large integral gain used to perform

the approach in a suitable short time, an overshoot to much larger negative frequency shifts and therefore a near–contact with the sample may occur.

In the experiments, the tip was approached towards the sample from 500 nm by activating the z–feedback until a frequency shift of -3 Hz was obtained.

4. In many MFM experiments, the local tip–sample distance is controlled using previously recorded topographic data of the scan area (lift mode). This data is mostly acquired in an intermittent contact mode. Due to the strong van der Waals forces between the tip–apex and the sample, the tip and its coating may suffer damage. In this test, an image was scanned in intermittent mode before an MFM image was taken.

5. As already mentioned in point three, the forces between a sharp tip and sample are very small above a tip–sample separation of 10 nm, but increase steeply during the last few nanometers. Therefore, an approach of the cantilever to the sample based on only monitoring the frequency shift might be dangerous. It may result in a crash of the cantilever into sample with the coarse positioning system upon approach.

In this test, the cantilever was retracted from an initial position of 10 nm above the sample surface to a distance of 350 nm and then approached in one step of 500 nm with the coarse positioning system. Then the cantilever was retracted one step of 500 nm and normally approached to a z-feedback set–point of -3 Hz.

All tests were performed with each cantilever type using the hr-MFM described in chapter 2.3. The tips were coated from one side of the taper with 2 nm of Pd and 6 nm of Co and magnetized in a field of 2.0 T prior to the measurements. After each procedure, three images of 1.5 μm $\times$ 1.5 μm size with 256 $\times$ 256 data points were taken on the perpendicular hard disk calibration sample of Hitachi GSD (cf. chapter 1.3). After each scan, the distance to the sample was measured.

The images in figure 3.3.11 contains the tracks of 4 to 12 bits/μm density of the Hitachi GSD calibration sample taken with SC tip. They were calculated to have exactly the same tip–sample separation of 17.3 nm. The degradation of the imaging properties of the cantilever throughout the test series is qualitatively apparent. In an image taken before the first test (original image), as shown in panel (a), the lateral magnetic resolution is excellent. The bit transitions as well as the speckle stray field pattern between the tracks are clearly resolved. The images in panels (b) to (f) are taken after tests one to five. In the test procedures the tip and its magnetic coating has been damaged, namely the apex has become blunter being less sensitive to short spatial magnetic wavelengths. In addition, the enlarged apex increases the van der Waals interaction between tip and sample; therefore, topography artifacts become more pronounced. This is visible by the numerous black spots in the images, indicated in panel (d) by red circles. However the bit transitions are still visible. After tests number four and five, depicted in panel (e) and (f), the resolution has decreased significantly. The tip magnetization has become unstable, multiple changes of the magnetic charge configuration at the apex are visible, especially in panel (f).

In an MFM measurement, the resulting image is a convolution of the sample stray field and the magnetic tip charge (cf. chapter 1.2). In order to carry out a quantitative comparison, the function describing the cantilever has to be extracted. This is done in the cantilever calibration process described in chapter 1.3. However, this procedure is time consuming. A quick comparison of the cantilever imaging properties can also be performed, if the images are taken on the same sample area. In the test series, all measurements were taken on the tracks of 4 to 12 bits/μm. Therefore, the function describing the sample is almost identical in all images. This allows a comparison of the image Fourier spectra, in order to gain values
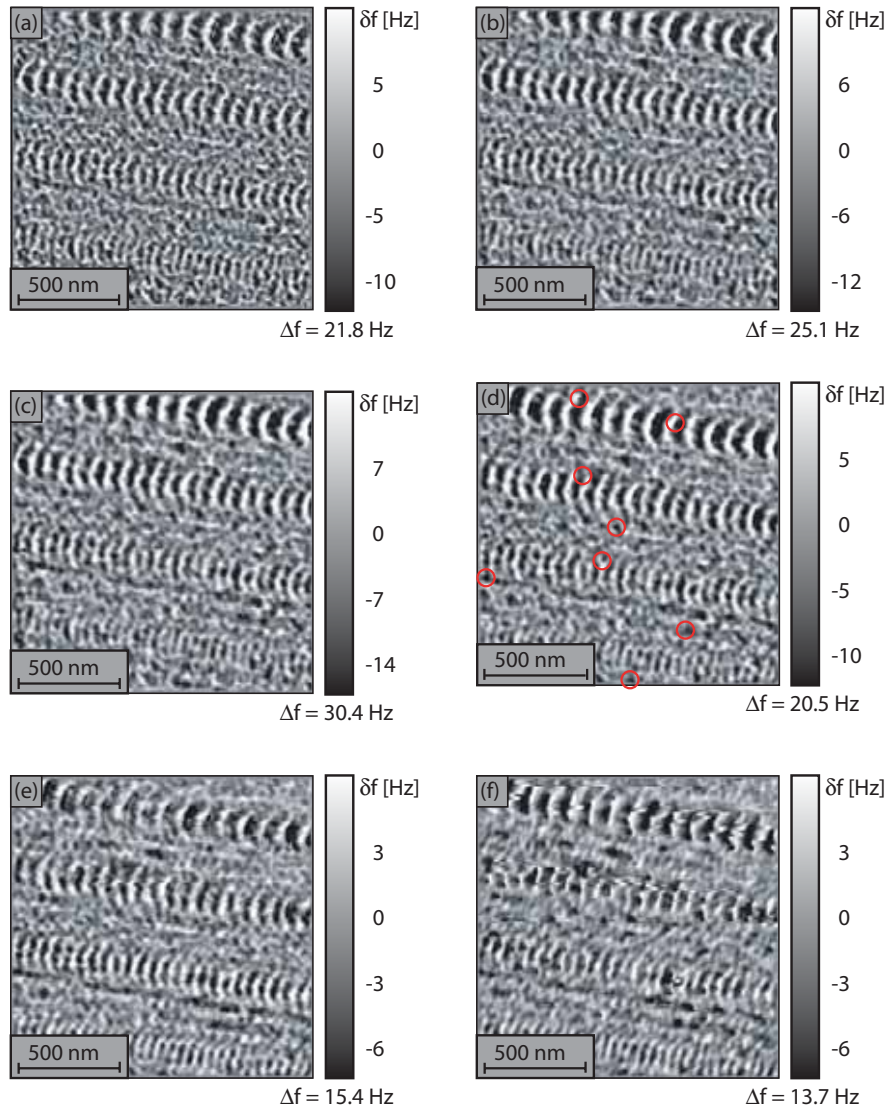
Fig. 3.3.11: Series of MFM images taken with the Team Nanotec SC tip. Panel (a) was taken before the first test. The subsequent panels (b) to (f) were acquired after tests one through five. In the last two images, the degradation of the imaging properties are clearly visible.

for the magnetic resolution and the magnetic imaging sensitivity.

These values are calculated by averaging the frequency components of different directions but same wave number k in Fourier space as described in [9, 17]. The averaged frequency components can be plotted and compared as a function of the wave number. The resulting spectrum is called *sensitivity spectrum*. Figure 3.3.12 shows the result for the SC cantilever. The solid black curve corresponds to the original tip, the solid curves in red and blue curve show the result for the tip after test procedure two and four respectively. Any given value in the curves, shows the magnetic imaging sensitivity of the tip for a given wave vector k which corresponds to a spatial wavelength λ via $\lambda = 2\pi/k$. The spatial wavelength is related to a measurable magnetic resolution by $\lambda_r = \lambda/2$. Any given value on the curves shows the sensitivity of the magnetic tip to image a corresponding wave vector k of the sample stray field. A more gradual decrease of the Fourier component values with increasing k represents a better imaging sensitivity of the tip for small magnetic objects.

The original tip shows the most gentle slope, meaning its imaging properties are best. Already

after procedure two, the tip has lost in magnetic imaging sensitivity for wavelengths smaller
than 105 nm and after test four, the overall imaging properties have become worse by a factor
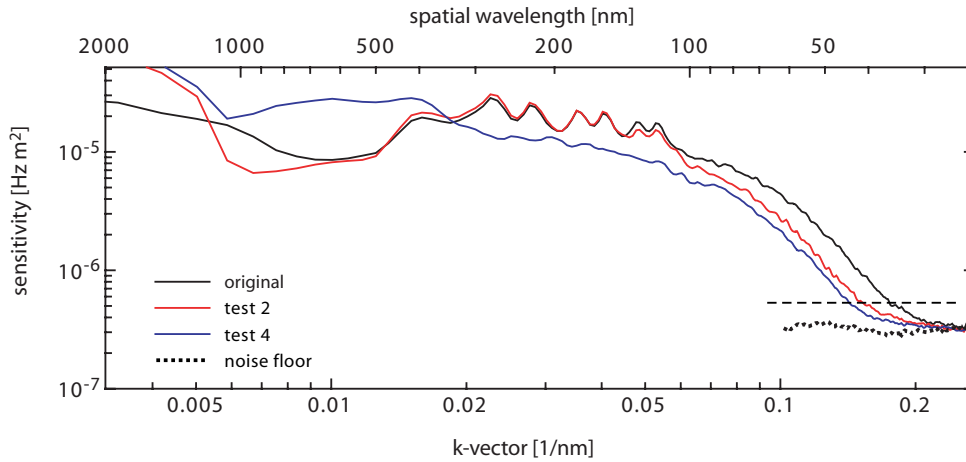of 3.5.

Fig. 3.3.12: Averaged frequency components of MFM images taken with Team Nanoworld SC
cantilever. The solid black curve denotes the original tip, the solid red and blue curves correspond
to images taken after test two and four, repectively. The black dotted and dashed lines show the
noise floor and its 3 dB higher average value.

In order to extract the maximum lateral magnetic resolution of the tips, the curves of the
averaged frequency components are compared to the noise floor in the measurements. The the
dotted black line in figure 3.3.12 was calculated in the same fashion as described above from
a so called *noise image*, measured by setting the dimensions of the scan field to zero. The
dashed black line is computed to lie 3 dB over the noise floor. The maximum magnetic lateral
resolution of the tip is calculated from the wavelength corresponding to the intersection of
the solid lines with the dashed black line. Following this analysis, 18.0 nm maximum lateral
resolution is calculated for the original SC tip, 21.5 nm for the tip after test two and 23.1 nm
after test four.

A more accurate, but time consuming, evaluation of the tips' imaging properties and its
magnetic lateral resolution can be performed by calibrating the cantilever after each test
procedure. It allows to completely extract the tip transfer function from the MFM image.
This has been done for all three types of cantilevers. The calibration procedure was the same
as described in chapter 1.3. Again, sensitivity spectra were calculated, this time from the
two dimensional tip transfer functions. The results for the Team NanoTech SC cantilever
are plotted in figure 3.3.13 as solid lines. Hereby, the different coloured curves correspond
to the original tip and the tip after test two to five respectively, as shown in the key of the
figure. After each test, the imaging properties of the cantilever become worse, reflected by
the steeper negative slopes of the curves. For a wavelength of 37 nm for example, the imaging
sensitivity has already decreased by a factor of 2.2 after test two and even by a factor of 5.9
after test five. However, after test three, the imaging sensitivity seems to be slightly better,
possibly resulting from a reconfiguration of the magnetic material at the apex of the tip.

The maximum lateral magnetic resolution of the tips was found by first calculating the
standard deviation of the tip transfer functions after each test procedure and then compute
their sensitivity spectra. The black dotted curve in figure 3.3.13 depicts such a histogram
for the original SC cantilever, the black dashed correlates with the value 3 dB higher than
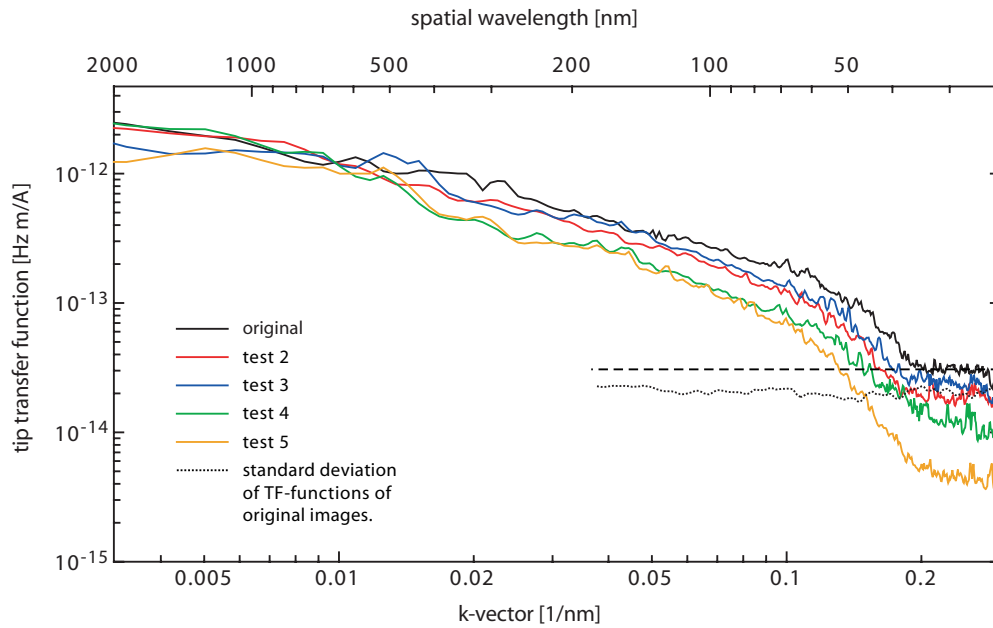the dotted curve. The wavelength corresponding to the intersection of the solid curves and

Fig. 3.3.13: Sensitivity spectra of Team Nanoworld SC cantilever transfer functions. The solid
black, red, blue, green and yellow curves correspond to the original tip and the tip after test two
to five, respectively. The dotted and dashed black curves shows the sensitivity spectrum of the
standard deviation of tip transfer functions computed after each test and its 3 dB higher value.

the dashed line is again used to compute the maximum lateral magnetic resolution. For the
original tip, maximum resolutions of 15.2 nm , for tests two and five, 17.3 nm and 25.1 nm
are extracted. In comparison to the values calculated above, the maximum lateral resolution
value determined after all tests is about 3 nm smaller.

Another very interesting aspect is the change in magnitude of the tip stray field and its geom-
etry during the test procedures. For high resolution MFM it is essential that the geometry
of the tip field has a circumferral symmetry and that it is confined closely about the center
of the tip apex. From the tip transfer function, a two dimensional map of the stray field in
a plane touching the apex of the tip, can be calculated. The curves in figure 5.4.18, show a
typical line section across the tip apex. Panel (a) depicts the tip stray field for the PP can-
tilever, panel (b) and (c) the SC and ISC levers respectively. The different coloured curves
correspond to the original tip and the tip after test two to five repectively, as shown in the
key of the figure.

A striking observation is the broadening of the ISC tip field after test four to almost double
size. The field is reduced by a factor of 5.5. Already after test two, the tip geometry and field
strength have altered. The SC tip, being less fragile shows almost no change in geometry
and magnitude of the tip field after test two. However, also after the tapping mode test, the
width of the field distribution at half maximum (full width at half maximum, FWHM) has
broadened from initially 35.2 nm to 59.6 nm and the value of the field is reduced to half from
12.1 mT to 5.9 mT.
Least affected by all test procedures is the Nanoworld cantilever. The degradation of the
imaging properties is less strong, which can also be observed in a less stark drop of the stray
field values throughout the tests. Even operating it in tapping mode has a smaller influence
on the tip geometry and the stray field. The FWHM of the field distribution only broadens
by a factor of 1.5. For the SC and especially for the ISC tips it increases by a factor of up to
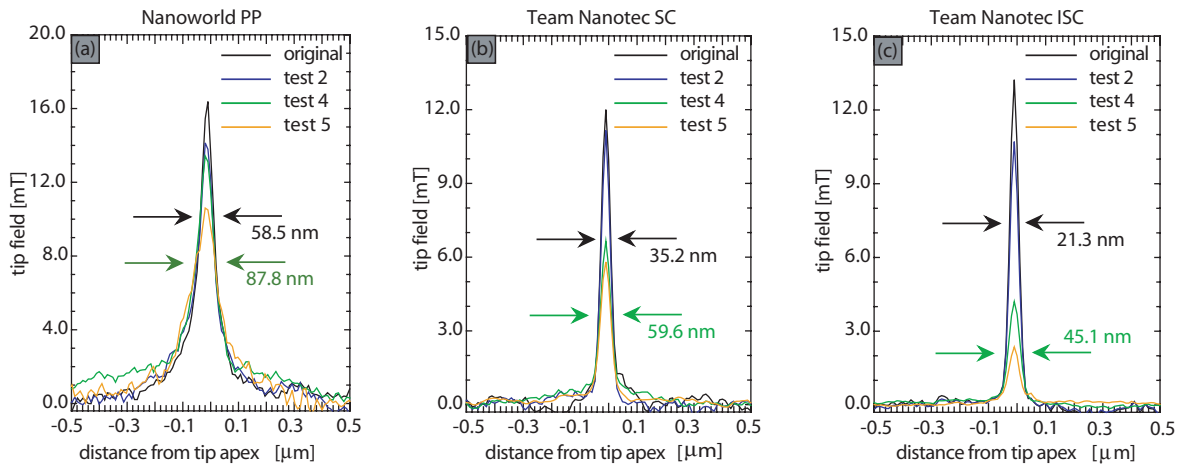2.1 due to their fragile nature resulting from their high aspect ratio and small cone angle of

Fig. 3.3.14: Cantilever stray fields of the Nanoworld PP (panel (a)) and the Team NanoTech SC (panel (b)) and Team NanoTech ISC (panel (c)) cantilevers. The solid black, blue, green and yellow lines correspond to the original tip and after test two, four and five. After test four the stray field of all cantilevers has diminished by almost half.

the tip apex (cf . figure 3.2.8, panels (a) and (d)).

The maximum lateral magnetic resolution as well as the maximum value of the tip stray field of all tests are summarized in table 3.3 for all cantilevers.

	Nanoworld PP		Team Nanotech SC		Team Nanotech ISC	
	res [nm]	field [mT]	res [nm]	field [mT]	res [nm]	field [mT]
Original	21.0	16.4	15.2	12.0	11.2	13.2
Test 1	21.7	14.1	15.6	11.1	11.6	10.7
Test 2	22.8	12.2	17.3	9.1	13.7	9.6
Test 3	23.7	13.4	17.9	10.0	15.5	8.9
Test 4	28.2	10.6	23.8	5.8	21.3	4.2
Test 5	33.4	10.2	25.1	4.9	26.7	2.5

Table 3.3.1: Summary of the results from the test procedures of the three different cantilever types. For each tip, the maximum lateral magnetic resolution is shown in the first column and the equivalent stray field of the tip in the second column. Resolution is abbreviated as *res.*

The table shows that the imaging properties of all cantilevers after test one are still very good. The reduction of the lateral resolution is small, less than 1 nm. This proves that high resolution MFM measurements are achievable in a true non-contact mode with a dissipation security set to a limit only slightly higher than the excitation needed to maintain a constant amplitude of the free oscillating cantilever. In addition, the degradation of the imaging properties is negligible. However, doubling the value for the dissipation security limit from $1.5\times$ to $3\times$ (test two) shows a significant impact on the fragile tips of Team Nanotec. The Nanosensor tip is less affected by this procedure.

Test four, in which the cantilevers were subjected to ten lines of intermittent contact mode, shows a dramatic degradation of the imaging properties of all three cantilever types. The lateral magnetic resolution decreases by almost 6 nm for the Team Nanotec cantilevers and by 4.5 nm for the Nanoworld tip. In addition, the maximum stray fields of the tips has diminished by a factor of 1.3, 2.1 and even 3.1 for the Nanoworld PP^{TM}, Team Nanotec

SC^{TM} and the Team Nanotec ISC^{TM} cantilever respectively. This clearly shows that tapping mode operation strongly influences the imaging properties of the cantilevers in a negative way. It follows, that this type of scan operation is not suitable for high resolution MFM measurements.

Crashing the cantilever tip into the sample (test five), a common operational mistake when manually approaching the cantilever to the sample, has a destructive impact on the tips. The lateral magnetic resolution decreases dramatically, for ISC^{TM} cantilevers from an initial 11.2 nm to 26.7 nm. This is only possible when a larger part of the tip apex or even a part of the cantilever taper has broken off. As can be seen in the MFM image in figure 3.3.11, panel (f), the magnetic layer at the end of the tip has an uncontrolled geometry and imaging conditions become unstable.

Chapter 4

MFM on hard disk recording media

4.1 Introduction

Magnetic data storage began with the invention of magnetic recording in 1898 when V. Poulsen attempted to record his own voice on a steel wire placed inside the gap of a electromagnet which was attached to a microphone [63, 64]. The invention was a success even though the longitudinal fringing fields of the electromagnet recorded the wire instead of the perpendicular fields, as Poulsen described in the patent. L. Mayer demonstrated perpendicular contact writing in 1958 using a permanently magnetized tip of steel wire which was dragged on the surface of a high coercitivity MnBi film having perpendicular magnetic anisotropy [65]. D. L. A. Tjaden showed the first non-contact longitudinal writing of bits in 1963 [66]. In the following years, only longitudinal magnetic recording was developed, until in 1977, S. Iwasaki invented the first practical implementation of perpendicular magnetic recording suitable for high densities [67].

In recent years, the hard disk (HD) has become the most used device for mass storage on a magnetic bases. It combines large storage space with fast access times and cheap manufacturing costs. In this way, it has outrun the magnetic tape and floppy disks in the last 10 years. Also compared to optical storage devices such as CDs and DVDs, the hard disk is a reliable and faster accessible medium. Only in terms of data archivation it is outlasted by optical media which can store data reliably up to 10 to 15 years compared to 7 to 10 years for HDs [68].

However the exponential increase in information that is following the prediction of Moore's law, has generated a need for increased storage space. The necessity to maintain the stored information efficiently, paired with the possibility to machine magnetic thin films precisely on a sub-micrometer scale has led to an increase in storage density on the hard disk by a factor 2.5×10^7 since the first presentation of the RAMAC 350 drive in 1956 [69, 70]. At present day, a data density of 40 to 80 GBit/in^2 equaling a bit length of 75 nm to 38 nm is used for common server and mobile product hard disks respectively.

The hard disk itself consists of a stack of several platters, sputter coated with a multilayer of magnetic and non-magnetic materials on both sides (see figure 4.1.1, panel (a)). Over every single platter surface flies a read and write head element which writes, reads and erases the information[1]. The elements sit on arms that can be positioned with sub-micrometer precision

---

[1]One single information is stored in a magnetic domain with uniform magnetization direction. Its is called a *bit*. These bits are disposed in concentric circles named *tracks*. This is shown in figure 4.1.1, panel (a).

over the platter. The flying height of the heads in a hard disk of todays mobile computers is less than 10 nm. The stability of the flying height and head–media separation, which is of great importance, can only be guaranteed by the maximum disk surface roughness of less than 3 nm to 2 nm and an advanced design of the underside of the head which makes it possible to hover on an air cushion. At present, several types of data storage on a magnetic hard disk are
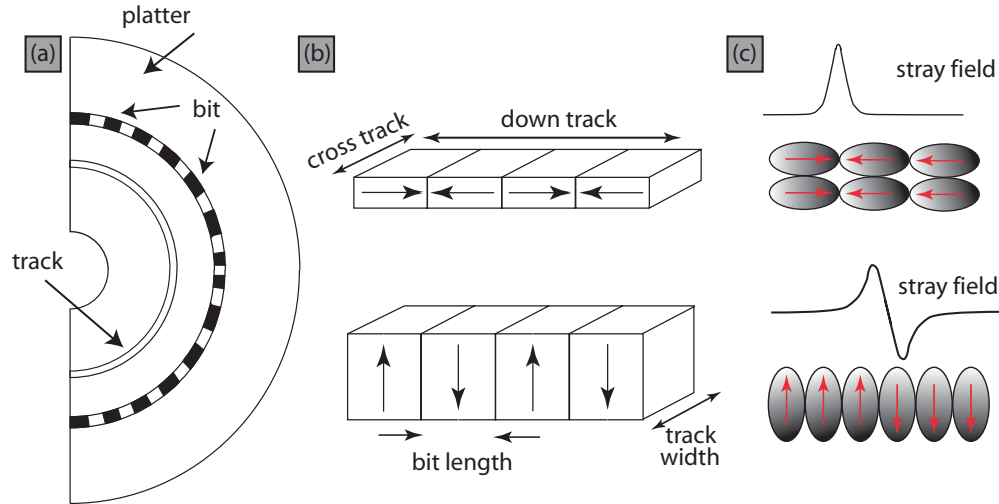

Fig. 4.1.1: Panel (a) shows the sketch of a hard disk platter. Single informations is stored in bits which are ordered along concentric tracks. The thin films for the two different major storage methods and the magnetization direction inside the bits are depicted in panel (b). The upper two sketches show the media for the in-plane storage method and the lower sketch shows the media for out-of-plane storage. In panel (c) the orientation of the magnetization in the sputtered grains is depicted. In in-plane storage, this directions lies in the film plane whereas for out-of-plane media, the axis lies perpendicular to the film plane.

used. The historically first exploited method is the so called in-plane method (longitudinal magnetic recording, LMR) where bits are stored with a magnetization direction within the film plane as shown in figure 4.1.1 (b) and (c) in the upper sketch. A recent improvement of this method is the antiferromagnetically coupled (AFC) in-plane media which has an under-layer in which the domains align antiferromagnetically to the written bits in the top layer [71, 72].

A completely different approach to store bits is the out-of-plane method where the magnetization direction of the bits lies perpendicular to the film plane (perpendicular magnetic recording, PMR), visualized in figure 4.1.1 (b) and (c) in the lower sketch. This method dates back to the ADF project at IBM begun in 1955; it was abandoned because of insufficient quality of the media and the write heads [70] but in recent years the out-of-plane storage method has been revived due to the possibility to be a candidate for ultra high storage density.

Depending on the storage method, the multilayers on the platters are differing. The layers are always sputter coated on either side of a SiO_2 or Al substrate. Common layers are a seed layer which ensures a very flat surface and ideal growth conditions. On top, a nonmetallic buffer layer is grown. For LMR media, a thick hard magnetic layer with in-plane anisotropy follows, for PRM media, a thick soft magnetic underlayer and a hard magnetic top layer are used. They are separated by a so called exchange breaking layer which effectively suppresses the magnetic exchange coupling of the two layers. All multilayer systems are topped by an amorphous carbon layer and a lubricant polymer to prevent the magnetic layers from oxidation and mechanical wear from the read/write head. The sputter process normally creates polycrystalline layers. Within the magnetic layers the sputtered grains are small

enough to only carry one domain and have a columnar form along their easy anisotropy direction. Furthermore the material in the write layers consist of an alloy of magnetic and non-magnetic elements. The latter tend to diffuse to the grain bounderies in a subsequent tempering phase, magnetically decoupling the grains to a certain extend.

In order to increase the storage density, the volume of the bit has to be decreased. There are several factors which can be improved, the most obvious of which is the bit length. The width of the bit as well as the space in between the tracks cannot be reduced much. The first is lower bound by the width of the read head element and distortions of the down-track sides of the bit due to fringe fields from the write head. The latter spacing cannot be made smaller than the cross-track fringe fields of the write head due to a possible erasure of neighboring tracks.

Decreasing the size of the bit implies decreasing the number of grains or their volume. Reducing the number of grains may lead to a fractured outline of the bit which especially at the transitions makes the read-back of the bit difficult. Decreasing the size of the grains seems more feasible at first. However there is a limit to this. As the volume V of a grain with anisotropy K_U is decreased, its magnetization is more and more prone to reversal by thermal activation of energy $k_B T$. In the so called *superparamagnetic limit* the magnetization direction of the grain starts to fluctuate due to the thermal excitation. In an extensive work, Charap *et al.* considered the anisotropy barrier necessary to maintain the stability of a written bit at different storage densities. For a lifetime of ten years it is necessary to have a ratio of $K_U V / k_B T > 42$ for a storage bit density of 10 GBit/in^2. This number rises rapidly with increased data density due to the increased demagnetization fields arising from shorter bits and the bits placed more closely together. Thus for 100 GBit/in^2, Charap *et al.* estimated the ratio to be $K_U V / k_B T > 100$ [73, 74]. The minimal size per grain is calculated to be about 8 nm to 10 nm. To reduce the grain volume further without endangering the stability, the anisotropy value K_U could be increased which is technically possible. However this implies that the maximum write field strength, needed to flip the magnetization of the grain into the intended direction, increases beyond an accessible limit. If the write field exerted by the maximum write current in the write element does not suffice to flip all grains in the domain, the resulting bit will be distorted. Several ways were found to circumvent this dilemma: Heat induced writing[2] or AFC media[3]. The AFC media type is now widely used in HDs even that the origin of the domain formation in the magnetic layers and their interplay is not fully understood yet [75, 74].

The most investigated possibility in recent years to circumvent the superparamagnetic limit, is the out-of-plane storage method. Using this technique, the volume can be kept large via the thickness of the film while the length of the bit can reduced. Moreover the anisotropy axis of the material now only has a one dimensional distribution while in in-plane media it is two dimensional. The distribution of the grain easy axes around the ideal direction gives rise to local stray field inhomogeneities commonly referred to as *noise*. This can deteriorate the recording performance.

One of the main technical difficulties in having the anisotropy axis of the grains perpendicular to the film plane is that the bit has to be written perpendicular to the gap field of the write

---

[2]Using this method, the thermal energy is enhanced locally by a laser heat pulse in the writing stage. Together with the field generated by the energized write element, the coercitivity of the medium is overcome.

[3]In this method, the antiferromagnetic coupling of the upper write layer (UL) to the lower layer (LL) keeps the magnetization stable even that the UL by itself would be superparamagnetic. However because the magnetization of the LL is antiparallel to the UL, the stray field at the bit transition is weaker and the sensitivity of the read head element must be improved to ensure a sufficient signal to noise ratio.
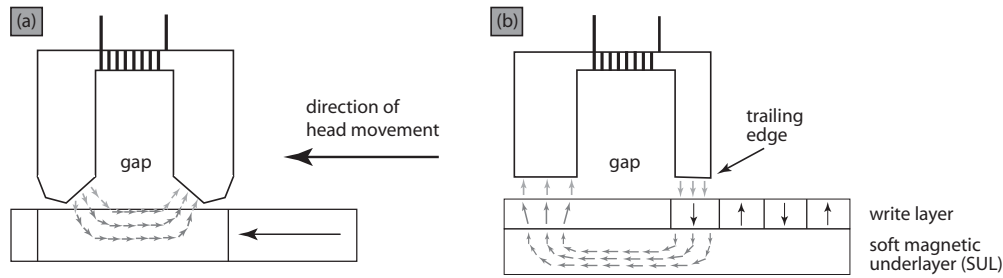
Fig. 4.1.2: Illustration of the different recording techniques for in-plane and out-of-plane media. For the in-plane media (panel (a)), the bit is written with the gap field. The media and the write head form a closed flux structure. For out-of-plane media, the bit is written with the fringe field of the head which is much weaker. Due to the perpendicular anisotropy of the write layer, a soft magnetic under layer is required which can close the flux structure.

head[4]. The bit is only written by the fringe field of the trailing edge of the write element (see figure 4.1.2 (b)) which is weaker compared to its deep gap field. Moreover in LMR, the writing layer formed part of the closed flux structure. To maintain a closed flux structure at the stage of writing in PMR, a *soft magnetic underlayer* (SUL) with ideally no anisotropy is needed, which closes the flux in the write process. In other words, the write head magnetic charges create mirror charges in the SUL and by that the write layer lies again inside an effective gap field.

4.2   Qualitative analysis

One of the key issues in pushing the storage density to higher values, is the tailoring of new materials which can support a higher density of written bits. The material parameters, like the hysteresis loop, are routinely measured by superconducting quantum interference device (SQUID) or magneto-optical Kerr effect (MOKE) devices. The write performance is usually investigated with a *spin stand*. The machine resembles an open hard drive in which the platter, the read and write head can easily be exchanged. The arm holding the heads can arbitrarily be positioned on the disk with high precision. The drawback is, that the read head reads an averaged stray field of minimum the head geometry (in laboratory demonstrations nowadays about 50 nm by 70 nm), only producing a one dimensional signal in down-track direction. If the signal cannot be read-back there is little way to test what has gone wrong.

MFM overcomes these problems by imaging the bit structure non-destructively on a local scale in real space. This makes it possible to image even details of bits and investigate the magnetic structure on the scale of the sputtered grains. It opens up a chance to qualitatively decide about writing or reading failures in the spin stand and judge if the problem has to be attributed to the media or the head. For this MFM has always been an analytical tool in the disk media industry. However, the recent decrease of the bit size has been orders of magnitude faster than the improvement of the average MFM resolution. Only recently with the development of high resolution MFM (hr-MFM) techniques and instruments, it is possible to investigate the bit details on the size of the grains of the material.

---

[4]In in-plane storage the magnetization of the bit was always parallel to the gap field direction and also inside the gap as depicted in figure 4.1.2 (a).

4.2.1   In-plane media

In order to test a certain material, tracks with successively higher dibit[5] densities are written into the material. Thereafter, the bits can be read-back in the spin stand or imaged with MFM. In figure 4.2.3 (a), a typical overview scan of such a track sequence is shown. The bit density depicted here, spans from 1.1 flux changes per micrometer (fc/μm) to 12.8 fc/μm. The width of the tracks is 450 nm. The data was measured with the hr-MFM prototype (cf. chapter 2.3). It should be pointed out, that the granular structure visible in the images is due to local stray field fluctuations on the length scale of the magnetic grains and not caused by the noise of the MFM measurement. The measurement noise is not visible in the images.

Apart from the strong repulsive or attractive interactions at the bit transitions, black and white spots are visible inside the bits and between the tracks. The first are due to grains inside the bit which are not fully saturated in the bit magnetization direction and are referred to as *bit noise* or *DC (erasure) noise*. One reason for this type of noise is mocaicity of the grain anisotropy axis. Therefore after writing, the grain magnetization direction can rotate out of the intended magnetization axes of the bit back into its local easy direction. Another reason is that the write field might be not large enough to overcome the coercitivity of the grain and it has simply not switched into the preferred direction. The local stray fields decrease the signal to noise ratio in a read-back process. However, an inspection of the bit areas in between the transitions on the low bit density tracks, almost no bit noise is visible. The spots at the side of the track have a similar physical origin. However, it is also possible, that they have aligned in the fringe field of the write element. This is usually referred to as *trailing edges* of the bit.
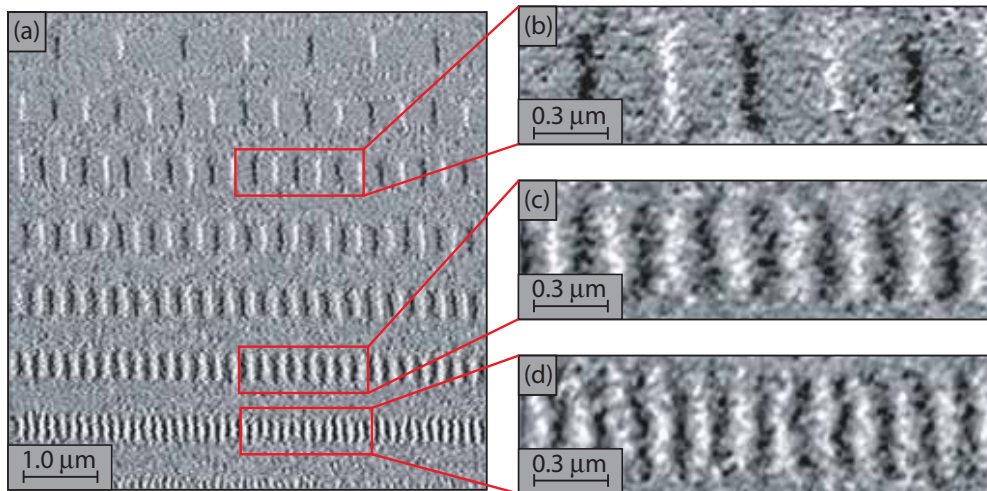

Fig. 4.2.3: Images of bits in an in-plane hard disk material. Panel (a) shows an overview of tracks with bit densities of 1.1 fc/μm to 12.8 fc/μm. The width of the tracks is 450 nm. Panels (b) through (d) show zooms on tracks with 3.3, 8.8 and 12.8 fc/μm.

Panels (b) through (d) show zooms of tracks with 3.3, 8.8 and 12.8 fc/μm bit density. The areas are marked with red boxes in panel (a). In all three zoomed images the ragged and

---

[5]A dibit is usually referred to a 1-0 bit combination. A sequence of these dibits forms an alternating magnetic charge distribution at the bit transitions. They produce a stray field which makes an attractive or repulsive interaction with the MFM tip. A repulsive interaction between a transition and the tip is imaged by a positive frequency shift (white transition) whereas an attractive interaction is produces a negative frequency shift (black transition).

grainy structure of the transition is visible. In panel (b), several fragmented transitions are visible. This so called *transition noise*, has its origin in the clustering of the grains due to exchange coupling and the mocaicity of the anisotropy axis. However, if these clusters are not too large compared to the size of the read element, they are not influencing the read-back process of the bit, because the read element averages over these bit defects. Moreover the transitions are clearly distinguishable in all tracks, the material can carry even the highest bit density imaged here.

Figure 4.2.4 shows tracks on a different in-plane media. Panel (a) is a 3.5 μm × 2.0 μm scan of a track with a random bit pattern. Clearly a difference in transition width and length is visible for the small and large bits. The large ones have long and wide transitions and vice versa for the small bits. This could be due to a non uniform development of the write field from the write element when it is energized. By this, the field in the middle of the head has reached the full magnitude faster than on its sides, making it possible to immediately saturate the grains only in the middle of the track. On the sides, the grains are only fully saturated in the large bits.
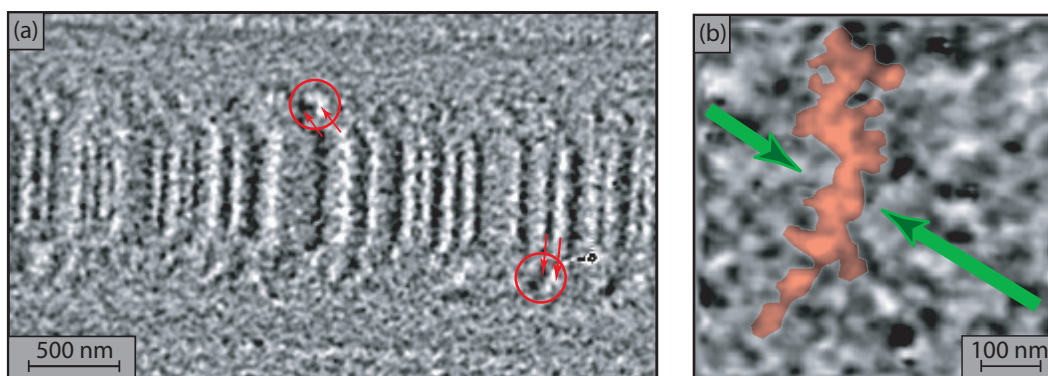
Fig. 4.2.4: Images of bits in an in-plane hard disk material. Panel (a) shows a 3.5 μm × 2.0 μm scan of a track with a random bit pattern which consists of large and small bits. Clearly a difference in transition width and length for both types is visible. The down-track borders of the track show enhanced noise which could indicate rests of a strong transition curvature due to a large fringe field of the writing head. The full developed curvature is not seen due to an erase effect of the writing head when writing the next bit (red circles and arrows). Panel (b) shows a high resolution zoom on a single transition which is highlighted in red. The image dimensions are 500 nm × 500 nm. The very ragged nature of the transition can be seen.

Another interesting observation is that the noise at the track edge is much higher than the noise further away from the track. This could indicate rests of strong trailing edges due to a large fringe field of the writing head. The full developed edges are not seen on all bits due to an erase effect when writing the next bit. However some magnetic clusters have survived, indicated in panel (a) with red circles. The arrows show which transitions they belong to. Panel (b) shows a high resolution zoom on a single transition on the same media. The transition itself is marked in red to make it better visible, the magnetization direction in the adjacent bits is marked by arrows. The ragged form of the transition can be observed, also its width is not constant, indicating that the grains tend to agglomerate due to the intergranular exchange coupling or dipole interaction.

4.2.2 Out-of-plane media

Major research has been dedicated in the last years to out-of-plane recording. Here the magnetization lies perpendicular to the film plane, giving rise to surface charges and a stray field over the whole area of the bit. As mentioned in the introduction, the length of the bit can be decreased more easily than in LMR while still keeping a bit volume large enough to not run into the super-paramagnetic limit. In addition the dispersion of the anisotropy axes of the grains and with it the DC noise can be better controlled. However, the writing process for high bit densities still poses a challenge. Figure 4.2.5, panel (a), shows a typical out-of-plane media with bit densities of 13 fc/μm to 35 fc/μm, a DC magnetized track and a track with bits of random length. Panels (b) through (d) show zooms of 0.8 μm $\times$ 3.0 μm of
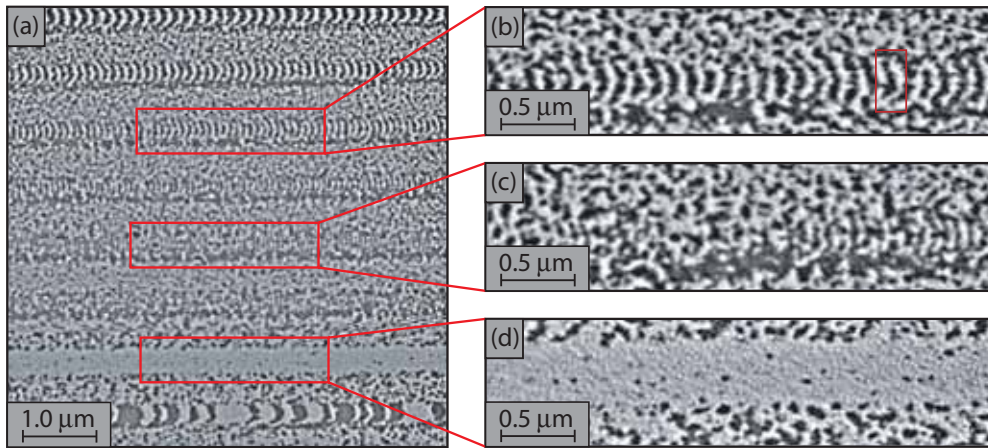
Fig. 4.2.5: MFM images of bits in an out-of-plane media. Panel (a) shows an overview of several tracks with densities in the range of 13 to 35 bits/μm, a DC magnetized track and a track with bits of random length (from top to bottom). Panels (b) though (d) show zooms of the tracks with densities 22 and 31 bits/μm and the DC erased track. The bits of the track in panel (b) are still distinguishable whereas the ones of the track in panel (c) have already merged or reordered. The DC magnetized tack in panel (d) shows a distinct white granular structure probably due to single grains with a higher stray field than neighboring grains. Also, some grains with opposite magnetization direction (black spots) are visible.

the tracks with densities 22 bits/μm and 31 bits/μm and the DC erased track. The bits of the track in panel (b) are still distinguishable whereas the ones of the track in panel (c) have already merged or reordered. This suggests that the media can not support a bit density of 31 bits/μm and higher. The reorientation of the grains may be due to thermal excitation of the domains as well as exchange or dipole interaction from neighboring magnetic clusters, which can be strong enough to switch the magnetization of single grains.

A striking feature is the black "line" on the lower down-track side of the tracks. From panel (a) it can be seen that it is very pronounced at high frequency bit patterns but completely absent in the DC erase track and only visible for small bits in the random bit length track. Such a behaviour may indicate a problem of the writing element for high writing frequencies. Panel (d) finally shows a distinct white granular structure probably due to single grains with a higher stray field than neighboring grains. This granular structure can not arise from topographical artifacts because these would be imaged as black spots with a sharp change from white to black contrast due to the attractive nature of the van der Waals interaction (cf. chapter 3.1). Also, some grains with opposite magnetization direction (black grains) are visible. Their small number shows a strong exchange coupling between the grains.

Another very often observed feature in out-of-plane media recording is a pronounced curvature of the transition[6]. If the curvature is strong and the bit length small, it could occur that the curvature of one bit extends forward into the next bit (see rectangle in panel (b)) effectively surrounding it. This can give rise to read-back errors because the net stray field of the curvature of one bit and the center of the other bit, can average out over the area of the read element.
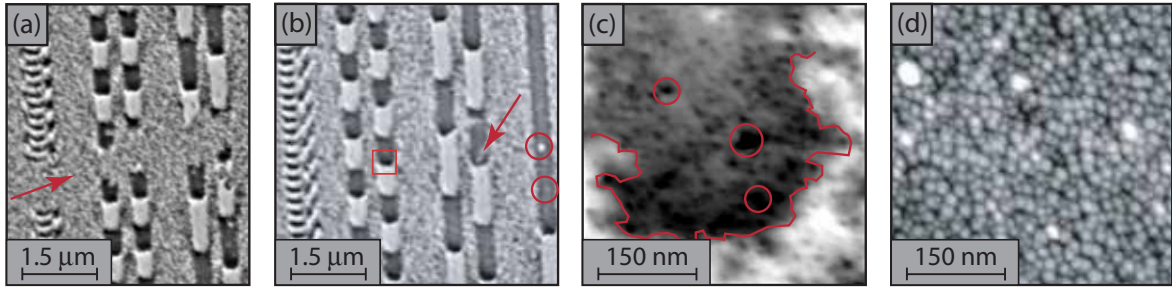

Fig. 4.2.6: Images of bits on another out-of-plane hard disk material. Panels (a) and (b) show defects in bits, namely a large demagnetized zone in panel (a) which could be due to a problem in the soft magnetic under layer and trailing edges of a high density bit pattern in the left most track. In the left most track in panel (b) these trailing edges are even more pronounced but only visible on the right side of the track. The encircled area shows a cluster of grains with reversed magnetization which occur in large bits. Panel (c) shows a high resolution zoom on one of the transitions (indicated in panel (b) with by a red square). The ragged transition line and the curvature can be seen. Panel (d) finally shows a typical topographic image of the magnetic grains on a out-of-plane media. The roughness distribution is about 3 nm.

Figure 4.2.6 shows more MFM images of tracks on PMR media. The image in panel (a) depicts an area of the disk where all tracks are disrupted (see arrow). Nevertheless, the material in this area is magnetic which can be seen from the speckle of magnetic clusters and grains with up or down magnetization. This phenomena may be explained by a very unhomogenous soft magnetic underlayer. If this layer is too thin in these particular areas or even has an own (small) domain structure, the bit is not written properly and thermal relaxation can lead to a reorientation of the grains. Panel (b) taken on the same media shows the same kind of erasure feature in the second track from the right (see arrow). However, the defect area is smaller.

An interesting observation can be made in the large bit on the right side of the image. It contains some small and one big domain of reversed orientation. This is due to the demagnetization field arising from magnetic surface charges as illustrated in the sketch on the left side of figure 4.2.7. The demagnetization field is largest in the center of the bit (cf. figure 4.2.7, lower right graph) and decreases towards the bit transitions. It is directed opposite to the magnetization direction within the bit[7] (cf. upper right graph). The demagnetization energy together with thermal activation energy, can reverse grains with a low anisotropy value in the middle of large bits. Such grains can become a nucleation center for the formation of larger reversed domains.

It is noteworthy, that in a low density pattern, the demagnetization field is large and causes

---

[6]This curvature arises mainly from the form of the writing head. Unlike in LMR, the PMR writing head has a single pole design with a rather round shaped geometry. When the head is energized, this leads to a sphere symmetrical field outside the head and to a curved bit transition.

[7]Consequently, the stray field outside the bit volume is smallest in the middle of the bit and largest at the transitions as shown in the upper right graph in figure 4.2.7.

the large magnetization decay, but the magnetization near the transitions decays very little. In the high density bit pattern, the demagnetization field is generally smaller and further reduced by the fields of the adjacent bits. This induces smaller decay throughout the area. Consequently, grains or clusters with reversed magnetization are almost never to be seen in high density tracks in perpendicular recorded bits. However, the effect is reverse for LMR bits. They become more severely demagnetized at high densities by the same effect.

In the high bit density tracks visible on the left side in panels (a) and (b) of figure 4.2.6, trailing edges are observable on the left and right border of the track and solely on the right side respectively. This indicates that the write head does not perform as intended at high writing frequencies. The trailing edges extend over several neighboring bits, effectively destabilizing them. Note, that similar, but less pronounced tailing edges are also visible in the lower bit density tracks in the same images.

Panel (c) shows a high resolution zoom of 500 nm × 500 nm on one of the bit transitions indicated in panel (b) with by a red square. The transitions indicated by the red line is very ragged. The black dots occurring in the black bit are artifacts caused by the non-flat topography of a sputtered, grainy layer. When a grain is higher than its neighboring grains, the tip scanning at constant average height will come closer to the sample and thus experience a larger attractive van der Waals force. Consequently, the frequency shift will become more negative and the contrast of the MFM image appears darker.

Finally, panel (d) shows a typical topographic image of an out-of plane media taken in constant frequency shift mode. The grains have a columnar form. The roughness of the layer is about 3 nm.
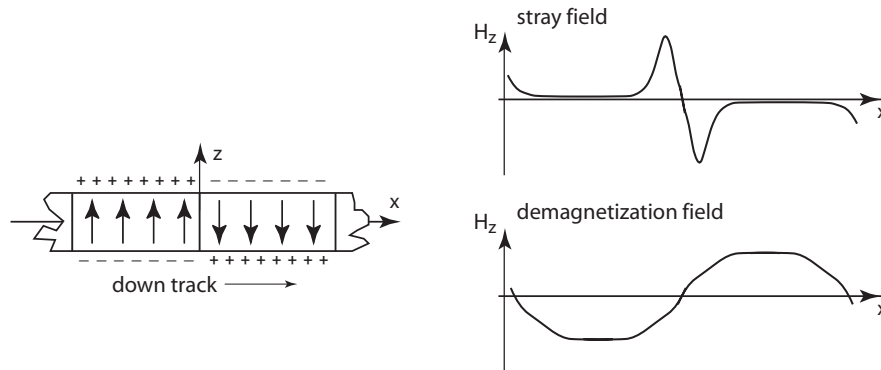
Fig. 4.2.7: Illustration for the description of the demagnetization field and the resulting decay of the stray field above the center of a large bit.

4.3   The stray field of a bit transition

As discussed in chapter 1.1, the stray field of an arbitrary three dimensional magnetization pattern can easily be calculated from the surface and volume charge distribution. This is favourably done in Fourier space. A disadvantage of this method is the lack of an analytical solution. However, for a simplified magnetization structure such an analytic solution may be found which still describes all the important features of the stray field. For both, in-plane and out-of-plane media in magnetic recording, the magnetization in cross-track direction is rather uniform. Thus, the initial three dimensional problem can be fully described in two dimensions if no explicit analysis of finite track effects are desired. The coordinate system

comprises the down-track direction (x-axis) and the direction perpendicular to the surface of the media (z-axis). Therefore, equation 1.1.1 in chapter 1.1 can be integrated in cross-track direction (y) assuming no variation in the magnetization to yield [76]:

$$\mathbf{H}(\mathbf{r}) = -\frac{1}{2\pi} \int_S d^2 r' \nabla \mathbf{M}(\mathbf{r}') \frac{\mathbf{r} - \mathbf{r}'}{|\mathbf{r} - \mathbf{r}'|} + \frac{1}{2\pi} \int_P dr' \mathbf{n}' \mathbf{M}(\mathbf{r}') \frac{\mathbf{r} - \mathbf{r}'}{|\mathbf{r} - \mathbf{r}'|}, \qquad (4.3.1)$$

with $\mathbf{r} = (x, z)$. The first integral is performed over the surface area S, the second integral is a line integral P around the area of integration. A useful simplification of equation 4.3.1 occurs for fields from plane surfaces (straight lines in 2D as shown in figure 4.3.8) with constant pole density. Let the edge lie along the z direction, let the vector $\mathbf{r} - \mathbf{r}'$ be described by
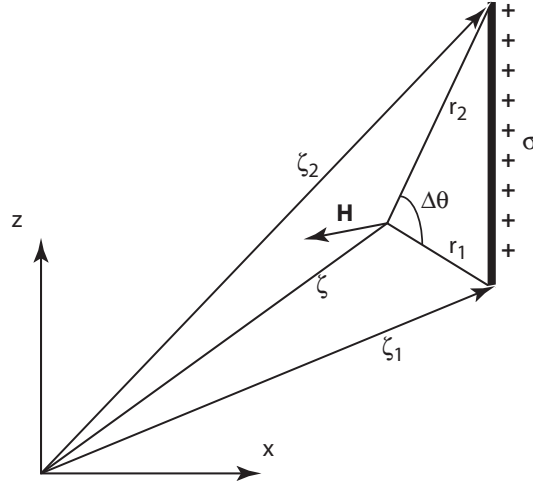
Fig. 4.3.8: Illustration for the calculation of the vector field from a 2D line source of constant charge σ.

the complex variable $\zeta = re^{i\theta}$ and let σ denote the surface charge density, the field can be rewritten as [76]:

$$H(r, \theta) = -\frac{\sigma}{2\pi} \Big[\Delta\theta + i \ln\Big(\frac{r_2}{r_1}\Big) \Big], \qquad (4.3.2)$$

which can be separated in a normal and tangential field component H_n and H_t respectively. r_1 and r_2 are the distances from the upper and lower surface and points to the observation point and $\Delta\theta$ is the in-between angle as shown in figure 4.3.8.

$$H_n = -\frac{\sigma \Delta\theta}{2\pi},$$
$$H_t = -\frac{\sigma \ln(r_2/r_1)}{2\pi}. \qquad (4.3.3)$$

The field tangential to the edge varies logarithmically with the distance ratio. Thus, the tangential field vanishes at any point along the centerline of a surface and becomes infinite at the corners.

Magnetized recording media produces fields by divergences in the magnetization. It can be assumed without loss of generality, that the magnetic pattern extends infinitely far in down-track direction and posses a finite thickness or magnetization depth which does not vary down-track.

For in-plane media, the field at a single perfectly sharp transition can readily be calculated from equation 4.3.3 if the demagnetization field is neglected. The volume charge for the case

of a perfectly sharp transition is equivalent to the surface charge of $\sigma = 2M_r$ at the transition center ($x = x_0$) extending from $-d/2 < z < d/2$ with d being the thickness of the media. The coordinate system (x, z) is centered in the middle of the medium at the transition center. The field for an in-plane media at the transition between two bits (cf. figure 4.3.9, panel (a)) becomes:

$$H_x^{IP}(x, z) = \frac{M_r}{2\pi} \ln \frac{(z + d/2)^2 + (x - x_0)^2}{(z - d/2)^2 + (x - x_0)^2}. \tag{4.3.4}$$

The field at the transition is either positive or negative depending on the sign of the magnetic charge. It vanishes infinitely far from the transition and reaches a maximum at the transition center as shown in the schematic drawing of the stray fields below the sketch in panel (a). The
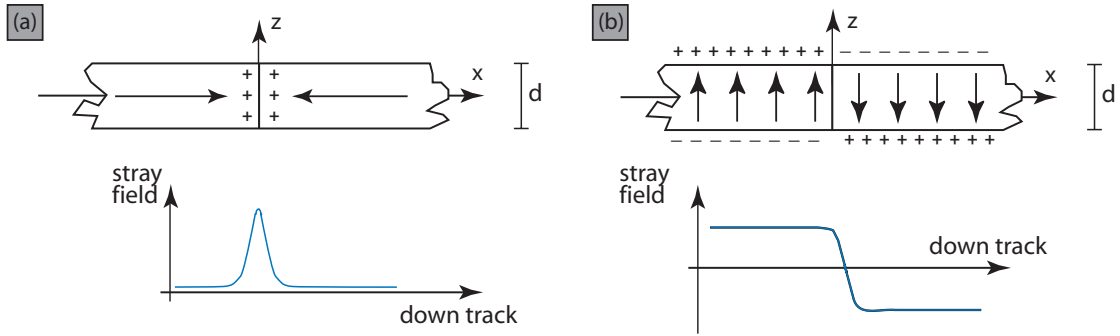
Fig. 4.3.9: Panel (a) shows the charge distribution for a perfectly sharp transition of longitudinal magnetization, panel (b) the charge distribution of a perpendicular magnetization. Below the sketches the schematic progression of both stray fields is shown.

field from a single, sharp transition of out-of-plane magnetization can also be derived from 4.3.3 but here four separately charged surfaces have to be taken into account (cf figure 4.3.9, panel (b)). Each possesses a surface charge of $\sigma = M$, but here, the sign varies. The net field component in down-track direction above the transition is equal to:

$$H_x^{OP}(x, z) = \frac{M_r}{\pi} \left(tan^{-1} \frac{x - x_0}{z + d/2} - tan^{-1} \frac{x - x_0}{z - d/2} \right). \tag{4.3.5}$$

The field always changes its sign at the bit transition. It always opposes the magnetization, vanishes at the transition center and becomes largest far from the transition as shown in the schematic drawing of the stray fields below the sketch in panel (b). There, the medium resembles a thin plate with maximum demagnetization factor. Thus, the field is equal in magnitude to the magnetization M_r.

If the transition is not sharp, the field patterns are broadened. The new field expression can be written as a convolution of the step transition fields and the normalized derivative of the down-track variation of the magnetization. If

$$F(x) = \frac{1}{2M_r} \frac{\partial M(x)}{\partial x} \tag{4.3.6}$$

with M_r being the saturation magnetization far from the transition, the field may be written as

$$H(x, z) = \int_{-\infty}^{\infty} dx' H^{step}(x - x', z) F(x'), \tag{4.3.7}$$

where $H^{step}(x - x', z)$ represents the field due to step transition given in equations 4.3.4 and 4.3.5. For example, if the magnetization has an arctangent form of

$$M(x) = \frac{2M_r}{\pi} tan^{-1} \frac{x - x_0}{a}, \tag{4.3.8}$$

where a represents the *transition length parameter* then $F(x)$ is given by

$$F(x) = \frac{a}{\pi(a^2 + (x - x_0)^2)} \qquad (4.3.9)$$

and the field in down-track direction finally writes:

$$H_x^{IP}(x, z) = \frac{M_r}{2\pi} \ln \frac{(a - d/2 + z)^2 + (x - x_0)^2}{(a + d/2 + z)^2 + (x - x_0)^2}. \qquad (4.3.10)$$

This is readily the field for an in-plane media transition. The field for an out-of-plane media transition is calculated in the same way by using a logarithmic magnetization form and yields:

$$H_x^{OP}(x, z) = \frac{M_r}{\pi} \Big[tan^{-1}\Big(\frac{x - x_0}{a + d/2 - z}\Big) - tan^{-1}\Big(\frac{x - x_0}{a + d/2 + z}\Big) \Big]. \qquad (4.3.11)$$

The total field emanating from a sequence of dibit transitions can be written as superposition of the individual transitions according to

$$H_{total}(x, z) = \sum_n (-1)^n H(x - nl, z) \qquad (4.3.12)$$

where l denotes the spacing between the transitions.

4.4   Quantitative analysis

The performance of a media/head combination for magnetic recording, is commonly tested by means of a so called *spin stand*. This instrument can roughly be described as an open hard disk drive in which the media and the read- and write-head can easily be exchanged. The control software and electronics of the spin stand allows the writing and read-back of an arbitrary bit pattern. Commonly the following procedure is used for media characterization: In a first step, various tracks are written into previously AD or DC demagnetized media, using one or more write heads. In addition, the write parameters, such as the flight-height and speed and the write head current can be varied. In a second step, the written data is read back by a special read head. This head generally has a width smaller than the width of the previously written tracks. In the read-back process a large number of transitions is read. This allows to carry out a profound statistical analysis which is used to determine parameters such as the general readability and the transition position jitter, that is the average misfit between the written bit and the clock pulse which times the energizing of the write element. There are also possibilities to extract the transition width and in limited cases, the curvature of the transitions. Also the evaluation of the AC and DC erasure noise can be performed. An in depth coverage of this topic can for example be found in [76].

A major disadvantage of the spin stand experiments is the lack of magnetic resolution on the length-scale of single magnetic grains or clusters. The read head always averages the local stay fields both in down-track and cross-track direction. In fact, the read head element stretches over more than two thirds across the track. It only outputs an integral information of the measured property[8]. Thus, the micromagnetic cause of the measured signal is not directly accessible. Another disadvantage arises from the statistical methods used to derive

---

[8]It is important to note that in general, many functions (distributions of magnetization) result in the same integral (measured response of read head).

the desired properties, which seemed to be advantageous at first sight. The detail of the single transition measurement is lost in the statistical averaging process. Thus the desired property can be extracted, but the cause of a non-expected value cannot be determined from the measured data. In order to explain such a value, micromagnetic simulations based on the parameters of the experiment have to be used.

In an MFM experiment, an average over the local stray field of the sample is performed as well, but on a much smaller scale. While the area over which the MFM tip averages in down-track direction may be comparable to that of the read head element, the cross-track averaging occurs on a much smaller scale. Therefore, the MFM image also reveals details of a transition in cross track direction, whereas the measurement signal in the case of the spin stand is only one dimensional in down-track direction.

The interpretation of the averaged physical properties of the media/head combination obtained from a spin stand experiment is well established in hard disk research. Thus, it is important, to extract similar averaged properties from the MFM images that can directly be compared to spin stand data. In a second step, high resolution MFM images have to be acquired and analyzed to reveal the micromagnetic origin for properties measured with the spin stand. Hence, in MFM imaging, procedures must be implemented to enable a comparison of the MFM results with spin stand results. The ultimate goal is, to bring the top-down (spin-stand) and bottom-up (MFM) approaches together [78, 77]. In the remainder of this chapter, several analysis methods are presented in order to extract important properties about the media and the write head from MFM data.

4.4.1 Extraction of the transition position

For the analysis of the MFM data, an MFM image of several tracks with different bit densities of an in-plane medium was acquired. From this image, two tracks were selected and suitable sub-images cut out of the raw data. The frequency shift images of two tracks are depicted in figure 4.4.10. The track in panel (a) has a bit density of 4.2 bits/μm, the track in panel (b) has a bit density of 13.0 bits/μm. The images were further subdivided into line sections in down-track direction. From these line sections, the transition centers were extracted as a function of the cross-track and down-track position[9].
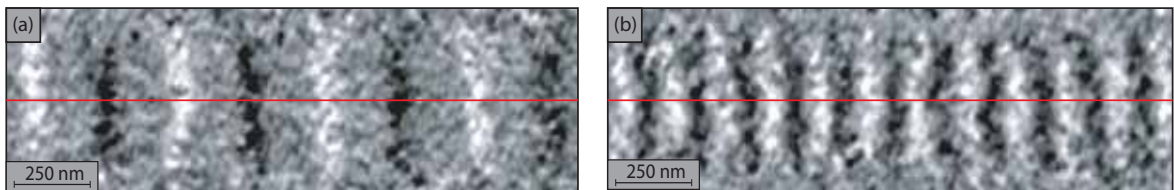

Fig. 4.4.10: Tracks on in-plane media chosen for the quantitative analysis. The track in panel (a) has a bit density of 4.2 bits/μm, the track in panel (b) has a bit density of 13.0 bits/μm. The line sections presented in figure 4.4.11 are taken along the red lines.

It is noteworthy, that the signal measured by a spin stand or by MFM is always a convolution of the stray field emanating from a magnetization distribution of the sample with the sensitivity function of the sensor. Thus, the measured data does not reflect all local variations of the magnetization structure, but only an average over a certain length scale. However, the data

---

[9]Note, that in a spin stand experiment, only the statistical average of the down-track transition position can be determined.

is still of value, because it reflects the quantity important to the intended application, namely to write and read information stored in the magnetic media. Nevertheless, in the following, the frequency shift data measured by MFM is fit by a function describing the stray field of multiple bit transitions. Even though the relation between the frequency shift and the stray field is not straight forward, the fit is assumed to be appropriate [79][10]. Equation 4.3.10 in combination with equation 4.3.12 was used for the fit. Therefore, only three parameters a, M_r and x_0 (further denoted here x_0^{MFM}) have to be found for each transition. All other values, namely $z = d_{ts}$ and d are known. Although the fitting procedure determines the position of the transitions $x_{0,i}^{MFM}$ precisely (cf. figure 4.4.11), the values of the other fit parameters are not equal to the correct values of the magnetization M_r and the transition length parameters a. This is due to the fit of frequency shift data with a function describing the stray field.

In order to reduce the number of free fit parameters, the same magnetization M_r and transition length parameters a was used for all transitions. Only the center position $x_{0,i}^{MFM}$ was fit for each transition individually. Therefore, the function fit to N transitions has $N + 2$ free parameters. In addition, suitable starting values and local search spaces were attributed to each position $x_{0,i}^{MFM}$.
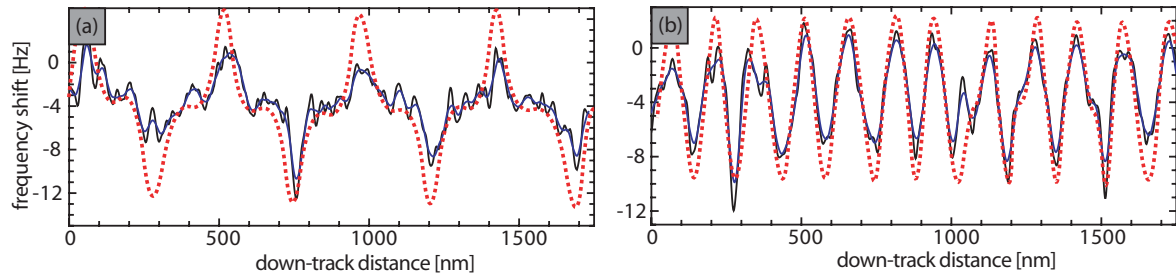
Fig. 4.4.11: Example of the fit of the transition positions to the two line scans marked with a red line in figure 4.4.10. The black, blue and red curves in both panels denote the original line section, the the smoothed line section and the fits according to equation 4.3.10.

Prior to fitting the data, the line section was smoothed by a running average over three measured data points which has the advantage of averaging out frequency shift noise. The result of such a smoothing (blue line) and the following fit (red line) of a line section (black line) for both tracks is depicted in figure 4.4.11. The black lines correspond to the line sections in figure 4.4.10. Note, that a better agreement for the intensity of the transition can be achieved, by fitting M_r for each transition as well.

The fit procedure was repeated for each line section taken along the tracks. In figure 4.4.12, the determined transition positions in cross-track and down-track direction are overlaid with the original MFM image. Panels (a) and (b) show the results for the low density track and the high density track, respectively. For clarity, a black line indicates the positions for a white transition (repulsive interaction between tip and sample), while a red line denotes the position of a black transition (attractive interaction between tip and sample). As can be observed, the fit transition positions are in excellent agreement with the transitions in the MFM images. However, there might be a difficulty in the determination of a transition center if the bit transition extends over several grains in the down-track direction. The fit-routine always chooses the data point with the peak intensity as the transition center, within the

---

[10]The correct approach would consist of the calibration of the MFM tip and the subsequent deconvolution of the tip transfer function from the MFM image in order to calculate the stray field of the sample. This was not done in the present analysis.
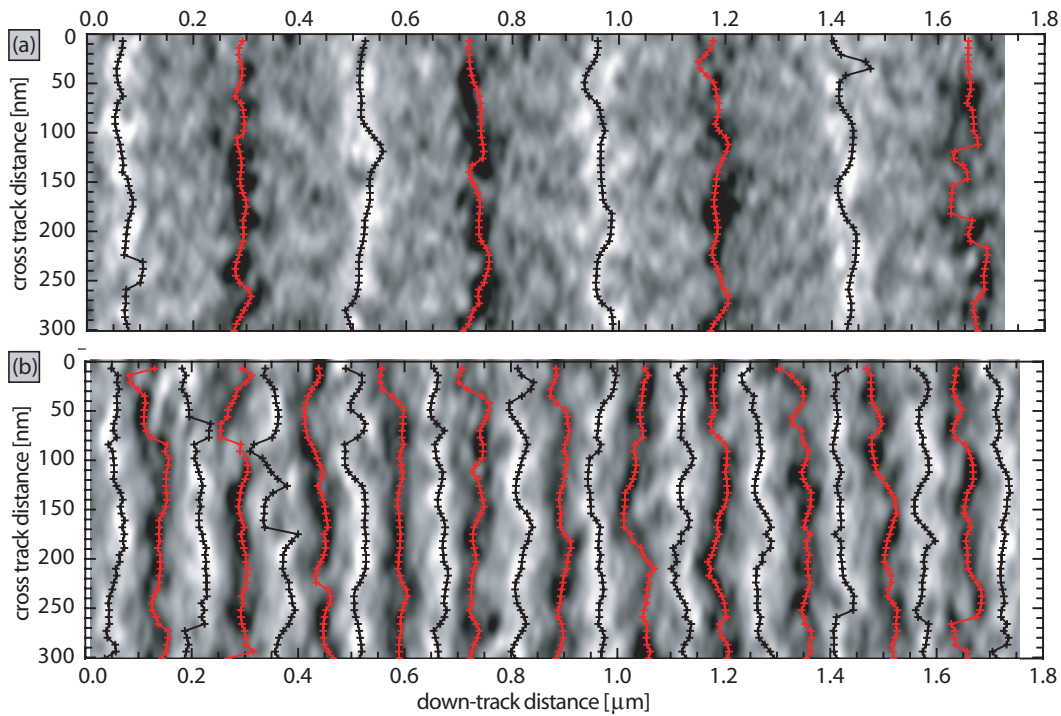
Fig. 4.4.12: Fit of transition centers for the tracks with 4.2 fc/μm (depicted in panel (a)) and one with 13.0 fc/μm (depicted in panel (b)) overlaid with the actual MFM measurement. Fitted transition values of white transitions are marked in black whereas centers of black transitions are marked in red.

given search space. The fit cannot decide, if the peak value is due to the transition center, clustering of grains nearby the transition, or random DC noise in large bits. Therefore a cautious examination of the transition positions has to be performed.

From the fitted transition positions, various properties, important for the characterization of a recording media/head combination can be extracted. Among these are the *transition position jitter*, the *transition jitter*, the *skew angle*, the *transition curvature*, the *cross-track form* of the transition, the *percolation* or the *DC* and *AC noise*. In this chapter, the focus was set on the first four properties[11].

4.4.2   Transition position jitter

The inter-bit spacing is determined by the properties of the media and the writing head, as well as the timing of the head energization. An ideal media/head combination and a perfect clock timing would therefore lead to a constant inter-bit spacing. While the timing of the head write current can be assumed as extremely precise, the evolution of the head stray field with time may deviate from the intended form causing a deviation from the actual bit transition position from the "clocked" position. In addition, the spacial anisotropy distribution of the media will lead to a deviation of the local bit transition position from the expected locations. Furthermore, the coercivity of the grains is depending on the sweep rate of the local stray field from the write head. Therefore, different bit sizes written into the same hard disk media, will generally lead to different bit characteristics.

---

[11]It is important to note, that these four properties can also be extracted from a spin stand experiment.

While the first position deviation, the *transition position jitter* (TPJ), is due to the write head, the latter, the *transition jitter* (TJ), arises from the media. The calculation of the first property is pursued in this section, the latter will be discussed in section 4.4.4.

In order to determine the TPJ, the following procedure was applied:

1. For each transition position $x_{0,i}^{MFM}$, the average down track position $\overline{x_i}^{MFM}$ (*averaged actual position*) was calculated. This was carried out by cross-track averaging the transition positions within each transition.

2. In order to determine the *expected ideal* position of the transitions, x_i^{ideal}, a fit function similar to the one used above, but with an inter-bit distance equal for all transition pairs was applied here. The value of the inter-bit distance as well as the average transition position was optimized in the fit, to obtain the least deviation from the measured data. In figure 4.4.13, the individually fitted transition position centers are overlaid with the averaged actual and expected ideal position of the transitions. The inter-bit distances
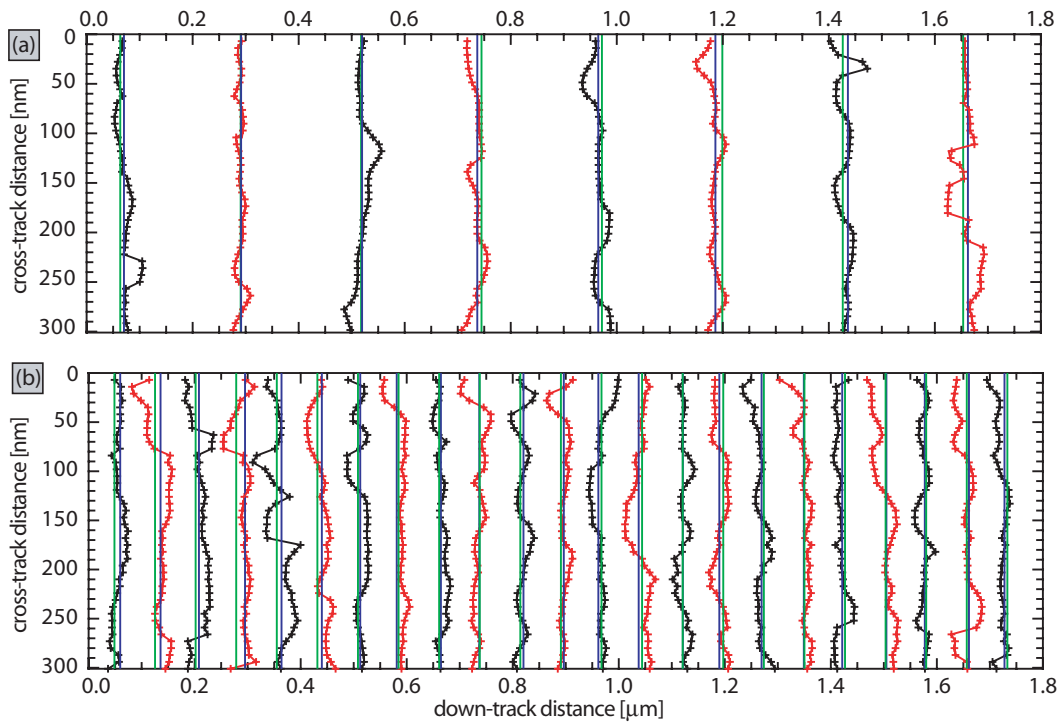
Fig. 4.4.13: Overlay of the average actual down-track transition position as calculated from the fit individual positions (blue lines) with the expected ideal transition positions (green lines). Panel (a) and (b) depict the results for the low and high bit density track, respectively.

found in the fit of the expected ideal transition position were 228 nm and 75 nm for the low and high density track, respectively. These values can be compared to the inter-bit spacing of the averaged actual transition positions of 233 nm and 77 nm. The values are in good agreement with the theoretical bit distance of 238 nm and 76 nm for a 4.2 fc/μm and 13.0 fc/μm track, respectively. The difference between the values of $\overline{x_i}^{MFM}$ and x_i^{ideal} for each transition is shown in figure 4.4.14.

3. In order to calculate a single figure of merit which can be compared to other bit densities as well as other head/media combinations, the standard deviation of the averaged actual
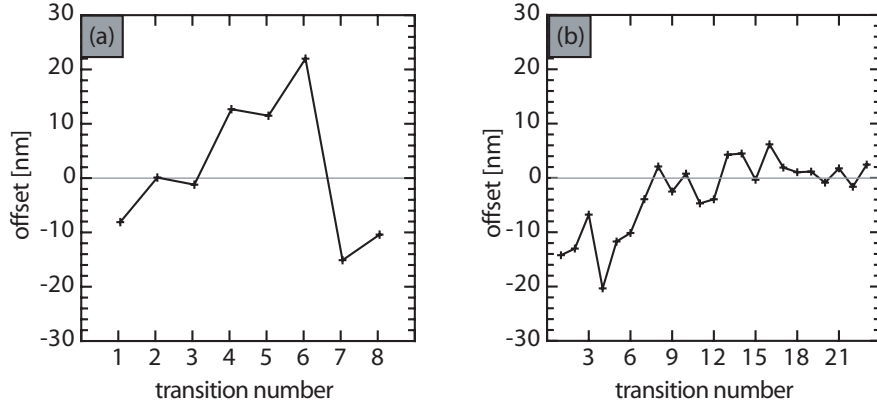
Fig. 4.4.14: Difference between the values of $\overline{x_i}^{MFM}$ and x_i^{ideal} for each transition. Panels (a) and (b) show the results for the low and high bit density track, respectively.

transition positions and the expected ideal down-track transition positions

$$TPJ = \sqrt{\frac{1}{N}\sum_{i=1}^{N}(\overline{x_i}^{MFM} - x_i^{ideal})^2} \qquad (4.4.13)$$

was calculated. For the low and high density tracks, the TPJ was found to be 10.3 nm and 8.9 nm, respectively. This value is on the order of the single grain size of the media.

The TPJ-values computed for the low and high density track should be equal under the following assumptions: the position deviation of a single transition is not influenced by the nearest-neighbor transition and the energizing behaviour of the write head is the same for different bit densities. Any difference of the TPJ-values must be attributed to the limited statistics.

4.4.3 Skew angle and transition curvature

In order to derive media properties from the fitted transition positions, it is essential to remove the influence of the write head, such as the geometry of the write field exerted from an energized head. Two distortion of the bit transitions are commonly attributed to the write head: the *skew angle* which describes, the angle α between the down-track direction and the axes of the bit transition in cross-track direction (cf. figure 4.4.15, panel (a)) and the *transition curvature* which describes any geometric distortions of the transitions from a straight line (cf. figure 4.4.15, panel (b))[12].

The following procedure was used to calculated the skew angle and the transition curvature:

1. The difference $\Delta x_{i,0}$ for every transition position $x_{0,i}$ and the averaged actual down-track average position $\overline{x_i}^{MFM}$ was calculated for each transition.

---

[12]The transition curvature has a significant impact on the read-back performance [80, 81], because the read head element might experience an averaged field at the center of one bit and the track edge curvature part of the neighboring bit. There have been continuous efforts in experimentally characterizing the transition curvature by using either spin stand testing [82] or magnetic force microscope techniques [77, 84].
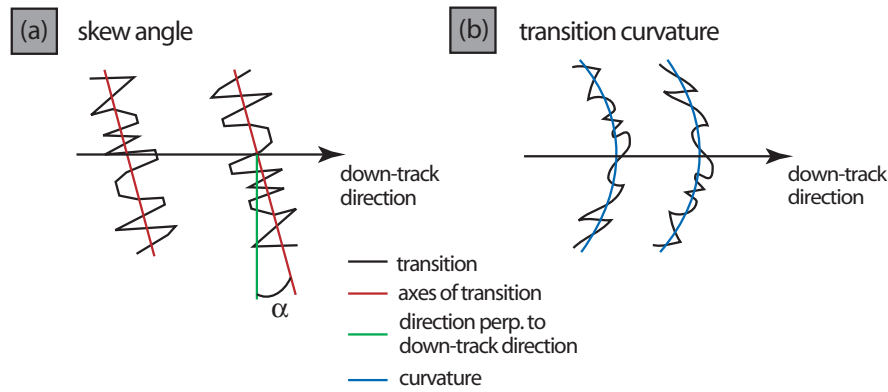
Fig. 4.4.15: Illustrations for the definition of the skew angle (panel (a)) and the transition curvature (panel (b)), two common distortions of an ideally straight transition, caused by the write head.

2. By averaging the $\Delta x_{i,0}$ in down-track direction over all imaged transitions, a *cross track profile* of an average transition was computed.

3. In order to calculate the skew angle α, a polynom of first order was fit to the average transition. From the fit, the angle could be determined (cf. figure 4.4.15, panel (a)).

4. The transition curvature can be described in most cases by a parabola of second order which was fit to the cross track profile (cf. figure 4.4.15, panel (b)) previously corrected for the skew angle.

Figure 4.4.16 shows the calculated cross track profiles (black solid lines) and the skew angle corrected profiles (dotted black lines). The red lines denote a parabolic fit into the corrected profile for the low and high bit density track in panel (a) and (b) respectively. The low bit
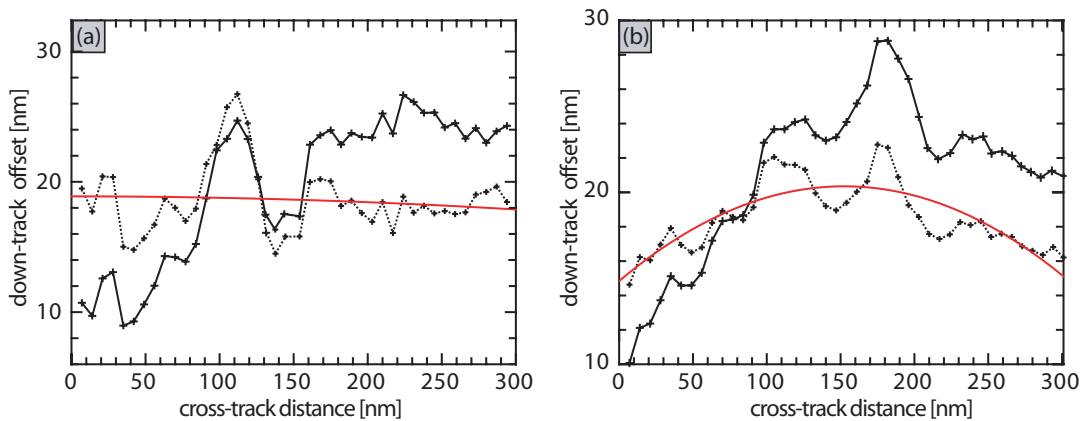
Fig. 4.4.16: Down-track averaged transition positions, the skew angle corrected transition positions and a parabolic fit of second order of the transition curvature for the low density track (panel (a)) and high density track (panel (b)). The original transitions are shown as a black solid line, the skew angle corrected transitions as a black dotted lines and the transition curvature fit as a solid red line.

density track has a skew angle of 1.8^o, the high density track a skew angle of 2.6^o. After the correction for this angle, the transition profile is more aligned in the cross-track direction. For both bit densities, the center of the curvature coincides with the cross-track center of the track. However, in panel (a), the curvature is almost negligible whereas in panel (b), the

curvature is pronounced and the difference between the middle of the track and the track border is 5.2 nm. Considering that for 100 GBit/in^2, the down-track length of the bit will be 15 nm, a transition curvature of this amount will have a significant impact on read-back performance.

4.4.4 Transition jitter

The transition jitter is due to a spatial distribution of the grain anisotropy and size in the vicinity of each transition. Thus a homogenous spatially well located head field will still generate a ragged bit transition. After the distortions of the transition profiles by the write head were removed, the analysis of the transition jitter was carried out by:

1. Calculating the standard deviation, σ_i, of the fitted transition positions, $x_{i,0}$, from the averaged actual down-track transition position, $\overline{x_i}^{MFM}$, for each individual bit transition.

2. Averaging the standard deviation σ_i in down-track direction over all measured transitions.

For the two analyzed tracks, the values are $TJ_{low} =$13.1 nm and $TJ_{high} =$13.5 nm for the low and high bit density track, respectively. This value is slightly higher than the average magnetic grain size of the media indicating a clustering of grains in the vicinity of the transition. Again, the values found for the two tracks should be identical, because they reflect a media property, as long as the cross-track position of the bit transition is not influenced by its nearest neighbors. Any variation of the numbers are due to the limited statistics.

Chapter 5

MFM on exchange bias multi-layers

5.1 Introduction

The balance between exchange, anisotropy and dipolar energy usually determines the domain structure of a ferromagnet (FM). However, coupling the FM to an antiferromagnet (AF) can significantly alter its magnetic behaviour, e.g. the hysteresis process or the domain structure. This is due to an additional FM–AF exchange interaction across their common interface. The most prominent effect found in these magnetic multi-layers is the shift of the hysteresis loop of the FM, called the *exchange bias shift*. In the last ten years, there has been considerable interest in exchange-biased ferromagnetic films. The hysteresis loop shift can be useful to control the magnetization in devices which sense changing magnetic fields by the giant magnetoresistance effect [85, 86], such as spin valves [87]. Read heads based on this effect are widely used nowadays in magnetic disk storage devices.

The change in magnetic properties arises from an established order in the antiferromagnet in the presence of a FM while cooling the AF below its ordering temperature (Néel temperature, T_N). By itself, the antiferromagnet can order in any one of its degenerate energy minima. When it is coupled to a ferromagnet, however, it chooses the state that minimizes the energy due to the coupling to the ferromagnet. Furthermore, the antiferromagnet is only weakly coupled to external magnetic fields, so it retains a "memory" of the ferromagnetic direction at the time when the antiferromagnetic order was set, even when the ferromagnetic magnetization is later rotated. This coupling is often thought of as a unidirectional anisotropy or as a fixed magnetic field acting at the interface. The shift in the hysteresis loop is not the only effect that is found in exchange-biased magnetic layers. Almost all FM–AF multi-layers show an increase in the coercivity, even when the sample is prepared in a state that does not show a bias.

The first experimental evidence of the exchange bias shift was published by W. H. Meiklejohn and C. P. Bean [88, 90] who compared the hysteresis loop of freshly prepared cobalt particles to cobalt particles they had stored in air for a while. Their model[1] explained the effect qualitatively correctly, however their quantitative predictions were two to three orders of

---

[1] Meiklejohn and Bean assumed that the Co-particles they had stored in air were covered by a thin layer of CoO due to oxidation processes, rendering it a FM–AF system. They concluded correctly that the bias of the FM hysteresis loop has its origin in the uncompensated interfacial spins of the antiferromagnetic layer. However, they assumed that the interface was ideally flat and consisted of a complete layer of uncompensated spins.

magnitude too large. Recent advances in theoretical models of the FM–AF interface try to close the gap between experiment and theory by the introduction of domains in the AF–layer [91], random fields due to the roughness of the interfacial layer [92, 93], an interdiffusion layer with reduced magnetic moment between the FM and AF–layer [94, 95] and spin flop configuration between both layers [96, 97, 98].

Apart from explaining the correct order of magnitude for the uncompensated spin density at the FM–AF interface, the models also have to explain the direction of the loop shift and the different domain reversal mechanisms for increasing and decreasing fields reported for several systems [99, 100, 101]. It follows that the average of the two reversal fields is not a reliable measure for the size of the unidirectional anisotropy.

Historically, the first experimental methods to study the exchange bias were based on tools that measure the magnetic hysteresis loop of a sample, such as a vibrating sample magnetometers (VSM) or superconducting quantum interference devices (SQUID) [103, 104]. In order to measure anisotropy directions, the samples were rotated in high fields and the torque was measured as a function of the angle [100, 105, 106]. An alternative technique to address the magnetic anisotropy is ferromagnetic resonance (FMR). The ferromagnetic resonance condition depends on the energy with respect to angular variations of the magnetization direction [107]. This is used to precisely measure the anisotropy direction of the FM in the multi-layer.

Only recently, methods exploiting x-ray magnetic circular dicroism were applied to exchange bias samples and in some cases, the uncompensated spin density at the AF–FM interface could be determined [108, 109, 110]. While XMCD and XMLD (x-ray magnetic linear dicroism) measure element specific magnetic moments, SQUID and VSM reveal the overall macroscopic magnetization.

In contrast to these methods, MFM measures a signal, that can be related to the stray field arising from a local magnetization distribution. A major advantage of MFM is the possibility to acquire real space images of the sample magnetic stray field in applied magnetic fields with a lateral resolution down to 10 nm in a very short time. This enables the study of domain structure evolutions in fine field steps, thus revealing a rather complete understanding of the micromagnetic properties of the investigated sample. In contrast to XMCD and XMLD, MFM only measures the combined stray field of all magnetic layers (FM and AF). Thus, the stray field emanating from the magnetic charges generated by the FM layer will generally dominate that from the AF layer. However, while the domain formation in the FM layer depends on an applied external field, its influence on the AF layers can be neglected. Therefore, the externally applied magnetic field is an experimental tool to distinguish between the stray field components originating from the FM and AF layers.

The calibration of the MFM tip (cf. chapter 1.3) further enables the quantitative determination of the magnetic stray field from a measured MFM image. The imaging properties of the MFM tip determined in the calibration process are then used as basis for models relating the magnetic stray field with the magnetization distribution of the sample.

Another experimental parameter that allows the distinction of the stray field components is the temperature. For a multitude of FM–AF systems, the Néel temperature is substantially lower than the Curie temperature T_C (ordering temperature of a ferromagnet). Therefore, the order of the AF layers can be switched off, if measurements are performed at temperatures T of $T_N < T < T_C$.

Although high magnetic field MFM experiments on exchange biased multi-layers have already been performed before, e.g. in [112, 113, 114], the combination of measurements with high lateral resolution at low temperatures and suitable quantitative data analysis have not been shown before.

For all the experiments presented in this chapter, the UHV low temperature scanning force microscope (LTSFM), described in chapter 2.2 was used. The temperature for all measurements was 8.0 K and the base pressure 2×10^{-10} mbar. With the aid of the superconducting solenoid, housed in the cryostat, the external magnetic field was varied between -7 T and 7 T perpendicular to the interface to explore the domain formation of the FM and AF–layers within the hysteresis loop.

5.2   Sample preparation and properties

As a model system with perpendicular anisotropy of the FM and AF–layers, a CoO/(Co/Pt) multi-layer sandwich sample with CoO/Co interfaces was chosen. Thus in the multi-layer system only two elements are present at the interfaces. These kind of binary ferromagnetic–antiferromagnetic samples are difficult to investigate with methods like XMCD or LMCD, because the chemical species at the interface do not differ from those within the FM– or AF–layers[2]. The perpendicular easy axes in the FM–layer is obtained via the high surface anisotropy of the five Co layers.
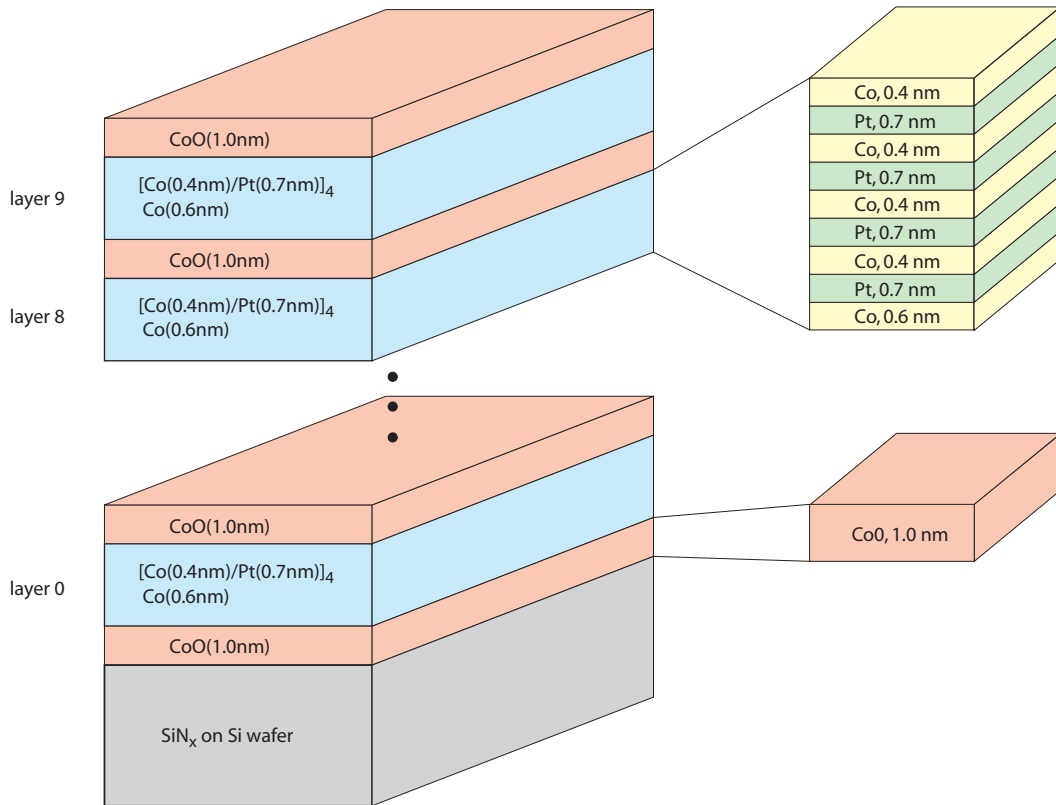
Fig. 5.2.1: Schematic layout of the sample used in the experiment. It consists of alternating layers of ferromagnetic Co/Pt packages and antiferromagnetic CoO interlayers. The Co/Pt packages have 5.0 nm total thickness and consist of 5 layers of Co, the lowest one being 2Å thicker than the other 4 due to the method by which the CoO interlayers were grown.

---

[2]Furthermore, the x-ray absorption peaks of metallic and ionic cobalt differ only slightly in energy. The resulting fine structure of the Co absorption peak is energetically very difficult to resolve with a high enough intensity making it almost impossible to distinguish contributions to the interface from the the FM– and the AF–layer using X-ray produced by present day synchrotrons.

The sample was prepared at Hitachi Global Storage Technologies (San Jose, USA) by DC magnetron sputtering on a Si wafer with a Si_3N_x over-layer and a seed layer of Pt. The deposition was performed at room temperature under an argon pressure of 2.3 mbar (3 mTorr). The magnetic multi-layer consist of sandwiched Co/CoO layers of the form CoO(10 Å){[Co(4 Å)/ Pt(7 Å)]$_4$ Co(6 Å)CoO(10 Å)}$_{10}$. The CoO layers were formed by natural oxidation of 16 Å thick Co layers in an oxigen rich atmosphere for 10 minutes. A bi-layer system of 10 Å CoO and 6 Å Co resulted (cf figure 5.2.1). As determined from XRD, the Co/Pt multi-layers are (111)-textured with an off-axes distribution (mocaicity) of 10° towards the [111]-normal (cf. figure 5.2.2, panel (c)). The sample is similar to those described in reference [115]. Figure 5.2.2, panel (a) shows the primitive cell structure of CoO. The Co^{2+} cations sit on the
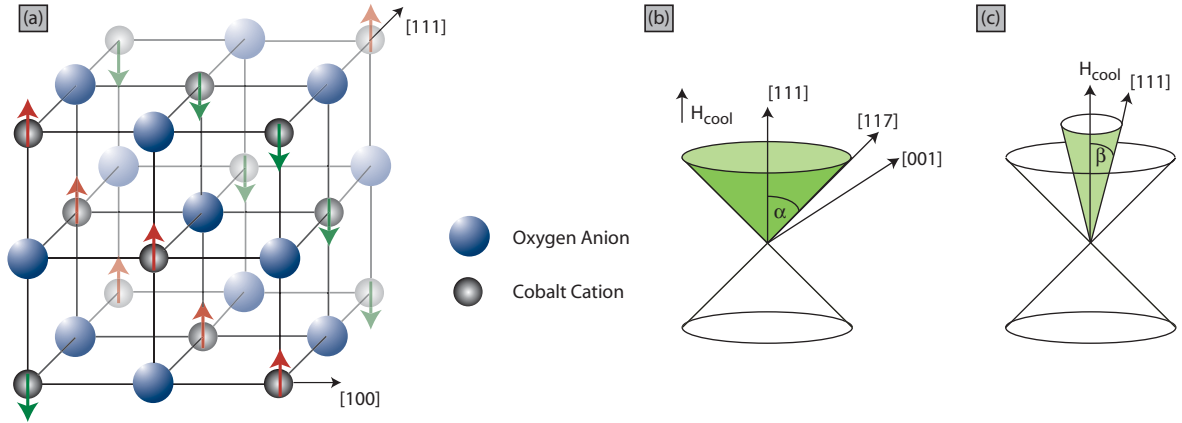
Fig. 5.2.2: Panel (a) shows the primitive cell of CoO (NaCl structure). The Co^{2+} cations sit on the corners of a cube and in the center of its sides, the O^{2-}-anions sit in the center of its edges. Ferromagnetic sheets of Co^{2+} are stacked in alternating antiferromagnetic order in [111]–direction coupled by super-exchange interaction via the O^{2-} ions. Panel (b): Upon cooling through T_N, the interfacial CoO spins freeze into their easy axes which is closest to the direction of the applied external cooling field. If H_{cool} is parallel the [111]–direction the CoO spins will be distributed on a cone defined by the <117> directions and the [111]-direction (half cone angle is $\alpha = 43.3^o$). Panel (c): The sputtered grains have a mocaicity of 10° of their [111]–axes towards the cooling field H_{cool} [111].

corners of a cube, the O^{2-}-anions in the center of its faces. For the whole analysis, the bulk spin structure of CoO is assumed, where the spins are aligned in ferromagnetic (111) sheets and point in <117> directions [126, 128, 130]. The spins in successive planes are antiferromagnetically coupled by super-exchange interaction via the oxygen ions.

Upon cooling through T_N in a field perpendicular to the sample plane, the interfacial AF spins are "frozen-in" to the spin anisotropy axes that are closest to the applied field. In the case of measuring the multi-layer perpendicular to the sample plane, the CoO spins of various AF domains will be distributed on a cone surface with half-apex angle 43.3^o if a perfect (111) texture is assumed [111]. The angle of 43.3^o is given by the [111] surface normal and the [117], [171], and [711] spin easy axes of CoO, which are closest to the [111] normal, as shown in 5.2.2, panel (b). Panel (c) shows the distribution of the [111] grain axes in the AF–layers.

5.3 Hysteresis loop measurements

The hysteresis loops shown in figure 5.3.3, panel (a) were obtained by SQUID magnetometry of the same sample at 50 K[3]. The magnetization loop measured after field cooling in 1.0 T is shifted by 105 mT in the direction of the applied cooling field direction. The coercitivity field was determined to be 375 mT. Previous studies on these samples have shown that the magnetic reversal of the field-cooled sample in saturation is almost symmetric. Deviations arise from the loop shift and differences in the nucleation behavior of the ascending and descending branches of the loop [115]. It is generally found that the spin structure of the AF–layer is determined during cooling mainly by the local ferromagnetic order within the domain. Thus, for samples cooled in a demagnetized stripe domain state, this pattern will be imprinted in the CoO layers. Then, no macroscopic bias is expected, but the sample will have locally biased regions depending on the local magnetic direction of the spins [103]. Indeed, the hysteresis loop after cooling the sample in zero field (figure 5.3.3, panel (a), red open squares) shows no apparent exchange bias. In addition, the nucleation behaviour on both branches of the loop is similar.

The loop shift in the field cooled samples, strongly depends on the temperature. The evolu-
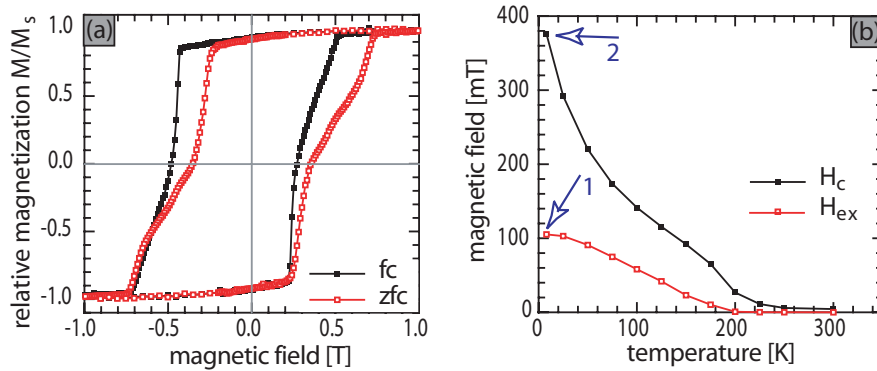
Fig. 5.3.3: Panel (a) shows the measured hysteresis loop after field cooling the sample in 1.0 T that saturates the sample in the positive field direction. The resulting hysteresis loop shows an expected bias field of -105 mT with a coercive field of 375 mT. Cooling the sample in zero field shows no apparent exchange bias. Panel (b) shows the temperature evolution of the exchange bias and the coercitivity. The loss of exchange bias identifies a blocking temperature of 200 K while the coercive field enhancement suggests a somewhat higher Néel temperature of about 250 K similar to that shown in reference [111].

tion of the coercitivity field and the exchange field versus temperature is shown in panel (b). The loss of exchange bias identifies a blocking temperature of 200 K while the coercive field enhancement suggests a somewhat higher Néel temperature of about 250 K, similar to that shown in reference [111]. At room temperature, both fields have vanished and the magnetic properties of the multi-layer system depends on the Co/Pt layers only. Due to the strong perpendicular anisotropy of Co/Pt, a demagnetized sample will show a maze–like domain pattern. However, the details of the domain structure morphology depend on the history of the applied magnetic field.

Cooling exchange bias samples in different domain states has been studied by a variety of authors [103, 104, 116, 117, 118, 119]. For the experiments performed in this thesis, the do-

---

[3]The room temperature magnetic properties (above the ordering of the CoO layers) of the samples are described in reference [103].

main structure of the Co/Pt layers was prepared using two different experimental procedures described below.

5.4   Sample cooled in saturation field

In order to study the evolution of the domain structure giving rise to the field-cooled loop (black filled squares in figure 5.3.3, panel (a)), the sample was cooled to 8.0 K, well below the Néel temperature of the AF layers. While cooling, a field of 2.0 T, well above the saturation field of the FM layer, was applied perpendicular to the sample surface. One of the virtues of this procedure is the possibility to study the impact of a naturally aligned AF on the FM–layer in the hysteresis loop.

All data were acquired using the same cantilever (ISC, Team NanoTec) coated with 2 nm of Pd and 6 nm of Co from one side of the taper of the tip. The cantilever had a resonance frequency of 61473 Hz, a spring constant of 0.5 N/m and a quality factor of 68150. The cantilever was oscillated at its resonance frequency with a constant amplitude of 5 nm. The tip-sample distance was held constant at 39 nm±2 nm for all images. Before analysis, the tip-sample distance was adjusted in MFM images to 39 nm.

5.4.1   The hysteresis loop cycle

After field cooling the sample in 2.0 T down to a temperature of 8.0 K, the field was reduced to zero. Then, a large amount of MFM images were taken in fields from 0 mT to -1200 mT and from 0 mT to +1200 mT. In the following, only a fraction of all measured data is shown. The presented images were selected to be representative for a specific magnetization state of the sample. The image are displayed in figures 5.4.4 to 5.4.10.

As expected from the squareness of the magnetization loop, no domain pattern is visible at 0 mT, after having field cooled in 2.0 T. Nevertheless, a weak granular contrast and stripe–like features are visible in figure 5.4.4, panel (a). The origin of this contrast will be discussed later. After acquiring the image in panel (a), the external magnetic field was increased against the direction of the cooling field[4]. At -664 mT, domain nucleation occurs suddenly. The image in panel (b) is scanned from left to right (fast scan direction) and bottom to top (slow scan direction). The nucleation of the domains occured when the tip was scanned near the middle of the image (see arrow). The growth of the reversed domains then appears faster than the tip velocity in the slow scan direction. The next image (panel (c)) measured in the same field was scanned from top to bottom. In the top left corner, the same domain pattern is visible, but below the position where the sudden nucleation occurred in panel (b), a similar looking distribution of reversed domains has appeared. In addition, another domain nucleation process is observed at the location indicated by arrow one. Note that the domain pattern visible in panel (c) differs from that of a conventional Co/Pt multi-layer sample. In such a sample, similar reverse domains would be observed, but the measured frequency variation will be identical for similar sized domains. Here, this is not the case. Arrow two indicates a domain which generates a much smaller frequency shift than the domain highlighted by arrow three. This may be an indication that the domain giving the weaker contrast (arrow two) is not present in all Co/Pt multi-layer sheets throughout the sample thickness. At a field of -674 mT (panel (d)), the domain nucleation has further proceeded

---

[4]In this experiment the positive field direction was defined to be the direction of the cooling field.
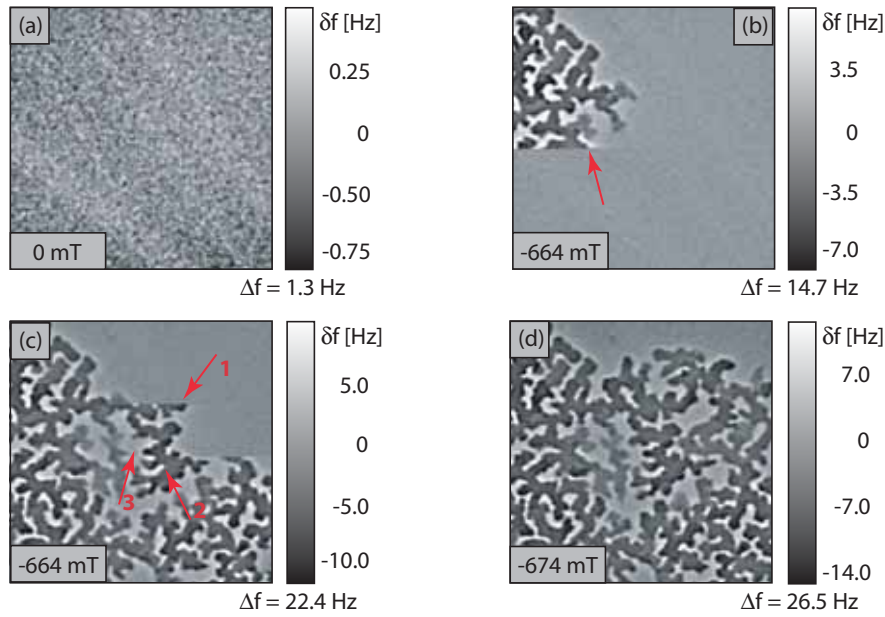
Fig. 5.4.4: MFM images of a full field cycle. Panel (a) is taken in zero field. Images in panels (b) and (c) are recorded in -664 mT. The domain nucleation, once started spreads through the image area without further increase of the external field. Panels (d) at -665 mT shows the stable domain configuration after nucleation. All images are 5 μm × 5 μm.

into the previously uniformly magnetized areas. Again, various levels of contrast within similar sized domains are visible. This is further illustrated by showing the measured data in parallel with an image with color coded contrast levels in figure 5.4.5. From a comparison of
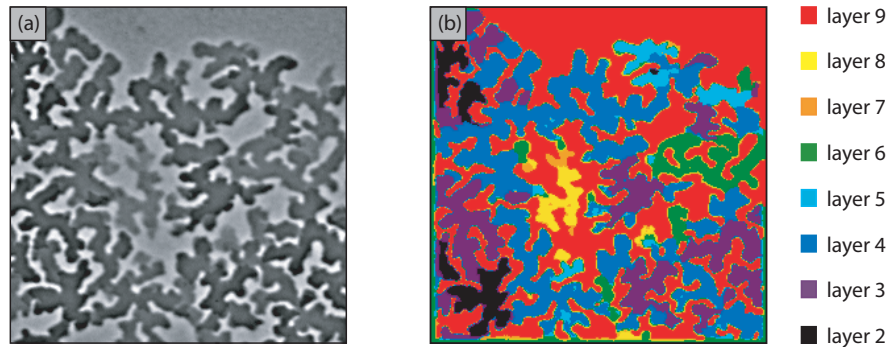
Fig. 5.4.5: The raw MFM image in panel (a) has been color coded in the image in panel (b) to elucidate the different contrast levels. The red, yellow, orange, green, light blue, dark blue, violet and black color denotes the levels two (darkest contrast level) to nine (brightest contrast level).

the indicated color levels in panel (b) with the original data (panel (a)), it is apparent that eight different contrast levels are visible. Here, the colors represent the different FM layers as indicated in the key of figure 5.4.5, panel (b). Level two represents the darkest contrast level and level nine the brightest contrast level in the raw data in panel (a). The observation can be explained by domains existing only in a limited number of the ten Co/Pt multi-layers in the sample.

Figure 5.4.6 shows the domain evolution in fields of -703 mT until -803 mT. At -703 mT (panel (a)), the large uniformly magnetized domain in the upper right corner of the image

has broken up into smaller domains. In addition, the area of domains with a magnetization opposite to the direction of the external fields has considerably decreased. Line–like domains are formed out of the more extended two-dimensional domains.

At -768 mT (panel (b)), the line–like domains become more pronounced. However, new two-
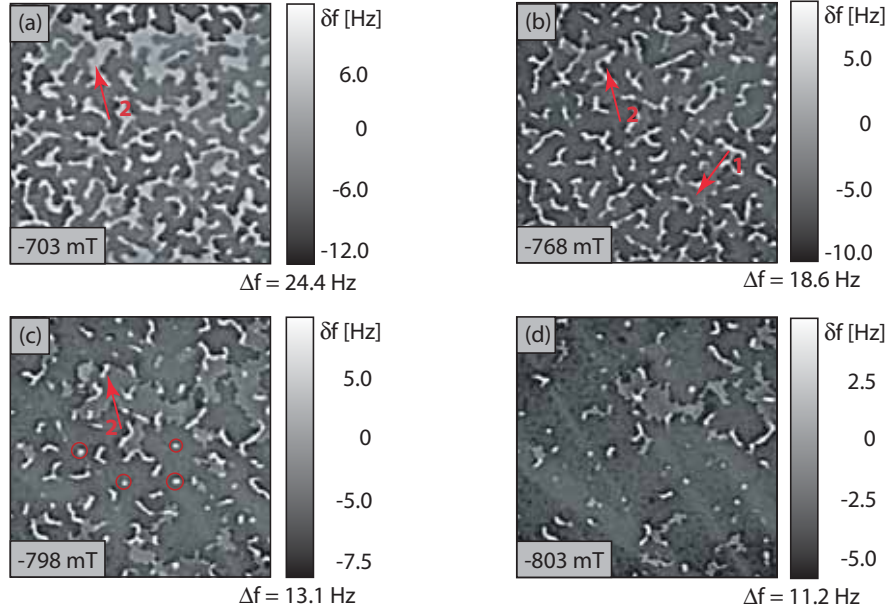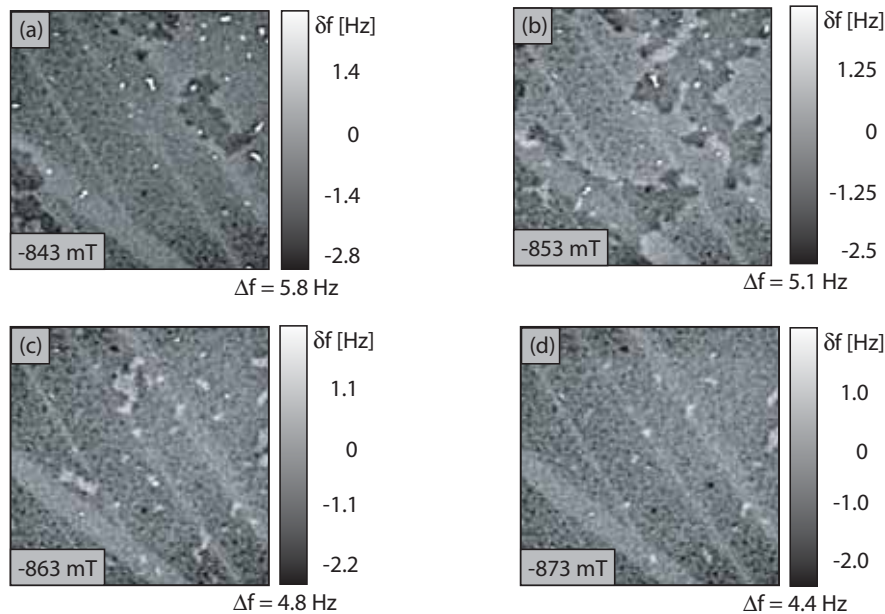

Fig. 5.4.6: MFM images of a full field cycle (*continued*): Panels (a) to (d) are taken in -703 mT, -768 mT, -798 mT, -803 mT respectively. All images are 5 μm × 5 μm.

dimensional domains with weaker contrast have appeared (see arrow one). Panel (c) shows an image taken in -798 mT field. The line–like domains have either become shorter (see arrows two in panel (b) and (c)) or have broken into several shorter pieces. In addition, many point–like domains have appeared (see red circles). At -803 mT (panel (d)), most line–like domains have disappeared and the image is dominated by point–like domains. Furthermore, the total area of two-dimensional domains of weak contrast that have appeared in a field of -798 mT has strongly decreased.

In the following, the formation of the line–like domains from their two-dimensional predecessors is discussed. The domains nucleating in the increasing external field have a magnetization parallel to the field and perpendicular to the surface of the sample. The large perpendicular anisotropy strongly favours Bloch walls between domains of opposite magnetization[5]. The magnetization vector thus rotates from a direction parallel to the external field into a direction antiparallel to the applied field when going from a nucleated domain via a domain wall to a location with the initial magnetization direction (cf, figure 5.4.7, panel (a)). The Bloch wall will have an in-plane magnetization direction. The domains with a magnetization opposite to the external field will shrink with increasing field to reduce their Zeemann energy. Thus, two initially well separated Bloch walls will approach each other (panel (b)). When two wall pieces come into close proximity, two different cases have to considered as shown in panels (c) and (d): In the first case, the two Bloch walls have the same in-plane magnetization direction (panel (c)) whereas in the second case, they have opposite magnetization directions

---

[5]In general, Bloch walls have reduced surface charges in thin magnetic films with perpendicular magnetization. In addition, they do not create volume charges; unlike Néel walls, they are divergence free.
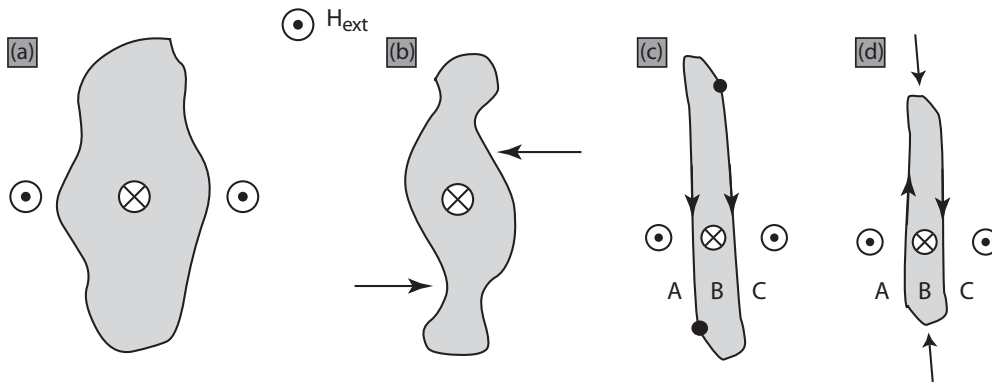
Fig. 5.4.7: Panels (a) and (b) show the evolution of domain formation in an increasing external magnetic field. Panels (c) and (d) depict the formation of unstable and stable line–like domain configurations.

(panel (d)). In the second case, the magnetization vector rotates 360 degrees when going from domain A via domain B into domain C, whereas in the first case, it only rotates to 180 degrees and then turns back. Consequently, domain B in panel (c) will easily annihilate in a sufficiently large external field. In the contrary situation, the two domain wall pieces in panel (d) can be compressed into an extremely small space but domain B cannot annihilate without breaking the formed spin-chain. Thus, domain B in panel (d) will only shrink by a reduction of its length, indicated by the arrows. The shrinking process depends strongly on the number of pinning centers (crystal defect, grain bounderies etc.) in the sample. The domain wall will be trapped until the Zeemann energy determined by the external field will exceed the energy needed to overcome the pinning center. Then the domain wall moves very quickly though the sample until it is stopped at another pinning center.
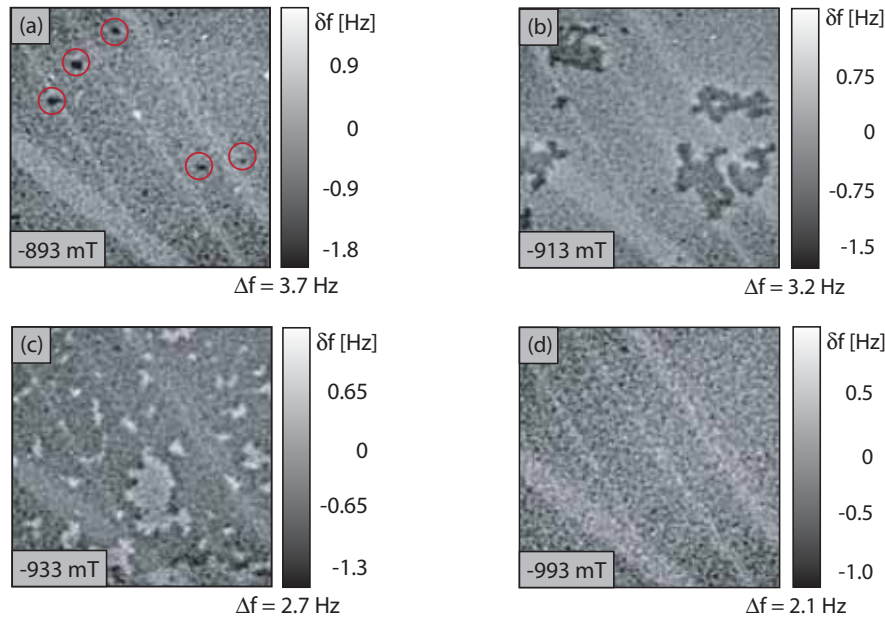

Fig. 5.4.8: MFM images of a full field cycle (continued): Panels (a) to (d) are taken in -843 mT, -853 mT, -863 mT, -873 mT respectively. All images are 5 μm $\times$ 5 μm.

Eventually, in a high enough field, the line–like domain will collapse into the point–like domain as indicated in panel (c) of figure 5.4.6. This kind of domain is very stable against annihilation and only vanishes in very high fields of more than -900 mT (cf. figure 5.4.9, panel (a)). Figure 5.4.8 shows the domain evolution in fields between -843 mT and -873 mT. In an external field of -843 mT, the line–like domains have collapsed into a few point–like domains (panel (a)). Surprisingly, new two-dimensional domains with an even weaker contrast have appeared.

At -853 mT (panel (b)), the total area of domains with a magnetization parallel to the applied field (dark domains) is about equal to that of domains antiparallel to the field (bright domains). In panel (c) an MFM image taken in -863 mT applied field is depicted. The bright domains have almost disappeared. Interestingly, only a few line–like domains have formed. This may be due to the initially smaller number of domain nucleation centers per unit area. It also indicates that the line–like domains are less stable because their ends are not well pinned. At -873 mT (panel (d)), the domains nucleated in a field of -843 mT (visible in panel (a)), have almost disappeared.

Surprisingly, in the MFM image taken at a field of -893 mT (cf panel (a) of figure 5.4.9), another domain structure is nucleated. Depicted in the images in panels (b) to (d) is the growth (panel (b) and (c) taken in -913 mT and -933 mT respectively) of these domains and finally the disappearance. This is shown in panel (d) at -993 mT field. The structure

Fig. 5.4.9: MFM images of a full field cycle (*continued*): Panels (a) to (d) are taken in -893 mT, -913 mT, -933 mT, -993 mT respectively. All images are 5 μm $\times$ 5 μm.

visible in the image of panel (d) again shows the same granular and line–like structures as already observed in figure 5.4.4, panel (a), measured in zero field after initially cooling down the sample. Raising the field to higher values, up to -1200 mT, does not show any further domain nucleation.

In figure 5.4.10, the evolution of the domain structure in fields parallel to the cooling field direction is presented. As expected from the shifted hysteresis loop, the exchange biasing leads to nucleation of domains in a weaker external field. The domains nucleate already at +440 mT as depicted in panel (a), as compared to the -664 mT on the negative field branch.
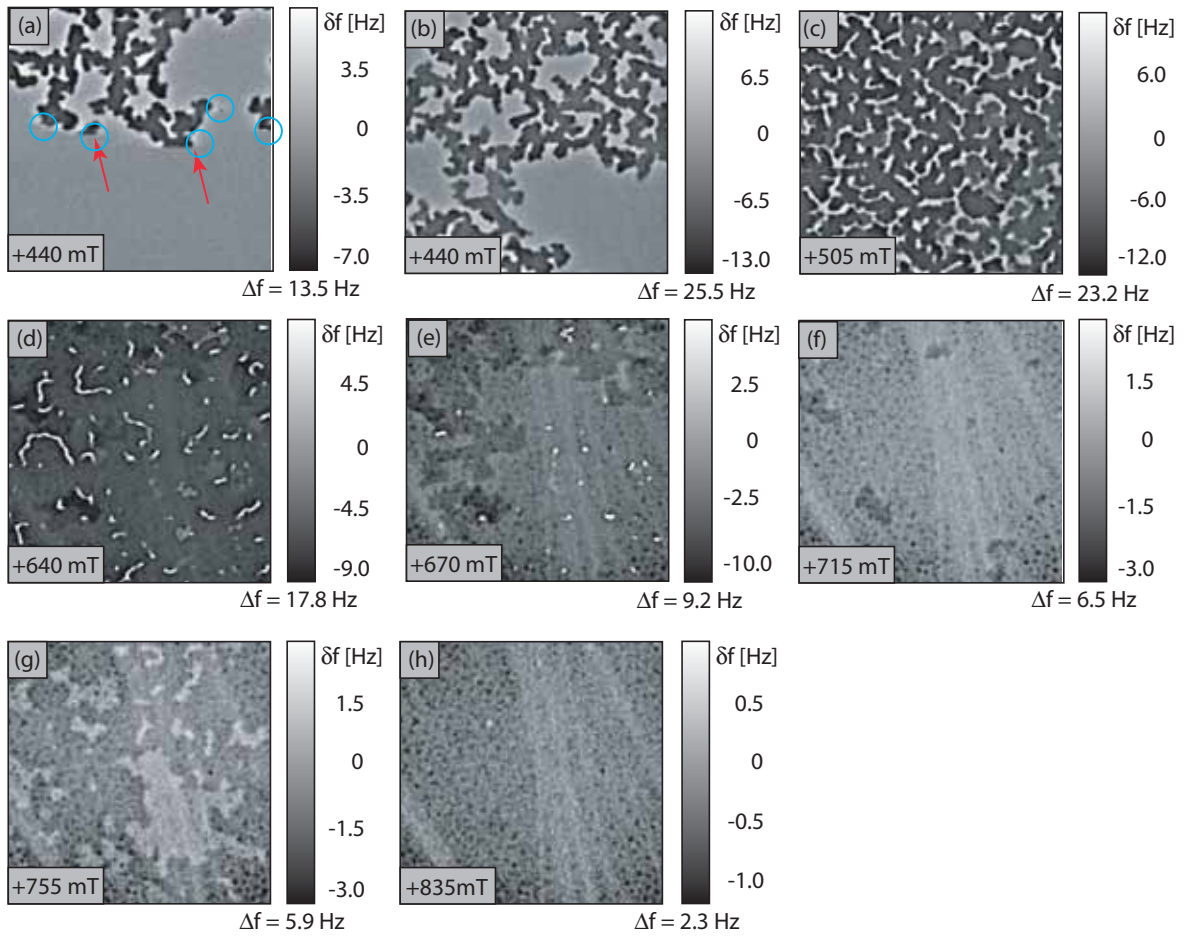
Fig. 5.4.10: MFM images of a full field cycle (*continued*): Panels (a) to (h) are taken in an external field of +440 mT, +505 mT, +640 mT, +670 mT, +715 mT, +755 mT and +835 mT respectively. All images are 5 μm × 5 μm.

Surprisingly, the nucleation is not as avalanche-like as on the negative field branch. There, the system advanced very fast from nucleation to an almost even distribution of domains with a magnetization parallel and antiparallel to the external field without changing the field. On the positive branch, at the field of domain nucleation a much smaller fraction of the total magnetization has switched into field direction (cf figure 5.4.4, panel (d) and figure 5.4.10, panel (b)). This confirms the SQUID loop measurements which predicted a rapid change of magnetization magnitude after nucleation in an external field directed antiparallel to the cooling field and a slow change in magnetization in an external field parallel to the cooling field. For clarity, this is shown in figure 5.4.11 where the two onsets of nucleation in the hysteresis loop of figure 5.3.3, panel (a) have been overlaid. The black squares show the nucleation for the negative branch, while the red squares represent the onset for the positive field branch. Clearly, the black curve has a sharper kink and is much steeper than the red curve.

In increasing fields, the sample passes through the same stages of domain nucleation and reversal described for the negative field branch. This is depicted in panels (b) to (d) at fields of +475 mT, +505 mT and +640 mT. In panel (a), the tip was scanned from the bottom to the top, nucleating the domain marked by the arrows. In panels (b) and (c), the two-
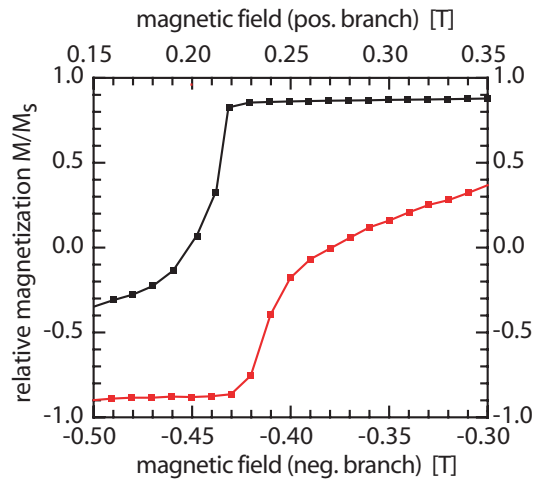
Fig. 5.4.11: Enlargement of the hystereses loop around the nucleation of the negative and positive field branch. It can be observed that the onset of nucleation on the negative branch (black squares) is much sharper than on the positive field branch (red squares).

dimensional domains of strong contrast slowly reduce into line–like domains. In panel (d) at +640 mT, most of these line–like domains have vanished or collapsed into point-like domains. Again, the formation of two-dimensional domains with weak contrast is visible. The reversal of these two-dimensional domains is depicted in the images in panels (e) and (f) in fields of +670 mT and +715 mT respectively. In panel (f), the nucleation of domains with an even weaker contrast is visible. The gradual reversal of these domains and the complete saturation of all FM–layers is depicted in panels (g) and (h) in fields of +755 mT and +835 mT. Raising the field to higher values up to +1200 mT does not show any further domain nucleation, as expected from the discussion of the images on the negative loop branch.

The two different onsets of nucleation for the negative and positive field branch suggests an exchange bias field of 112 mT[6] which agrees extremely well with the bias field determined from SQUID magnetrometry (see arrow one in figure 5.3.3, panel (b)). Note that the loop shown in figure 5.3.3, panel (a) was measured at 50 K and shows a smaller exchange field. Similarly, the nucleation fields at 50 K are smaller (-440 mT and +220 mT) than the ones determined from the MFM measurements (-664 mT and +440 mT). Thus a coercive field of 554 mT is calculated from the MFM data for 8.0 K, which compares well with the value measured by SQUID at lower temperatures (see arrow two in figure 5.3.3, panel (b)).

In the following subsections, three questions are further addressed. The first subsection is dedicated to the weak contrast visible only when the multi-layer sample is saturated. In the second subsection, the MFM data showing the last two domain formation processes (figures 5.4.8 and 5.4.9) are quantitatively analyzed. In the last subsection, the various contrast

---

[6]In general, the exchange bias field is defined as being proportional to the difference of the two coercive fields in the hysteresis loop. The coercivity of a bidirectional, hard magnetic material defines a value of the applied magnetic field in which the total amount of magnetized volume in one easy axes direction equals exactly that of the other easy axes direction. While the coercivities can be easily extracted form a VSM or SQUID loop, these prominent points are difficult to locate in a series of MFM images taken in an external magnetic field. In the sample at hand, this is further complicated by the layered structure of the ferromagnet. Therefore, the definition of the exchange bias field was slightly altered, now incorporating the two onsets of domain nucleation. These two points can easily be found in the hysteresis loop as well in as in a series of MFM images. Due to the small distribution of the crystalline and interfacial anisotropies in the FM layers, the thus defined exchange bias field agrees very well with the value of the old definition.

levels visible at intermediate magnetization states (figures 5.4.4 and 5.4.6) are explained by domains penetrating through a distinct number of Co/Pt layers.

5.4.2 Origin of weak contrast in low external fields

The image depicted in figure 5.4.4, panel (a) was taken directly after cooling, when all FM–layers were still aligned in the cooling field direction. It shows a very weak and grainy contrast as well as stripe–like areas of brighter contrast. The FM–layers are still saturated in the cooling field direction and do not contribute to the measured signal. Initially, it is not clear if the measured contrast arises from the underlying topography of the sample or from interfacial magnetic moments of the AF–layers. CoO is an atomically layered antiferromagnet, thus the net moment of these layers is rather small. This may lead to the small magnetic signal observable in the image in panel (a). In order to clarify whether the grainy contrast was of magnetic origin, a topography image of the sample surface was acquired. The grain size distribution on the sample surface is between 15 nm and 50 nm, therefore an expressive topography scan could only be performed for a small scan area of 500 nm × 500 nm. In figure 5.4.12, the topography scan is compared to a similar sized MFM zoom taken from panel (a) in figure 5.4.4. The topography image shows a grain-size distribution of about
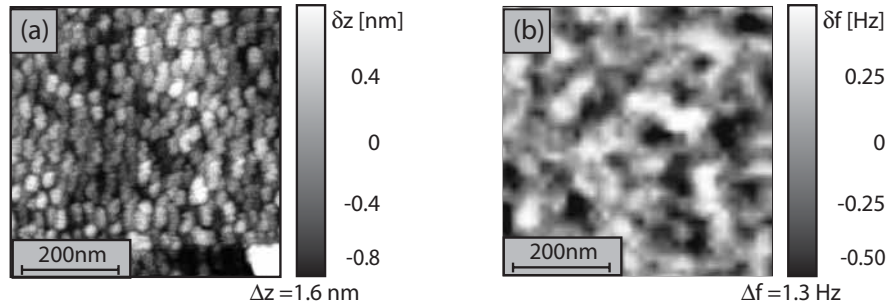
Fig. 5.4.12: Panel (a) shows the topography of the sample. The image has a size of 500 nm × 500nm. The grains have a size distribution of about 15 nm to 50 nm and a height distribution of 1.6 nm over the whole area. Panel (b) shows a similar sized MFM zoom taken from panel (a) in figure 5.4.4. The grainy features in the image have a larger length scale by a factor of about two.

15 nm to 50 nm and a maximum height difference of 1.6 nm over the whole area. The magnetic objects in the MFM zoom shown in panel (b) have a larger size by a factor of about two. This concludes that the grainy contrast seen in the MFM images is due to the uncompensated spins at the AF–FM interfaces. The large, stripe–like features with bright contrast visible in panel (a) of figure 5.4.4 may indeed by due to topography.

5.4.3 Origin of weak domain contrast in high fields

The domain formation process in high external fields above -843 mT and +670 mT shown in figures 5.4.8 to 5.4.10 is clearly differing from the domains nucleating and reversing in weaker external fields. Although the domain morphology is the same, the nucleation fields differ by almost 200 mT and the domains exhibit a much smaller stray field. In order to better understand this different behaviour, a quantitative analysis of the MFM–contrast in images of figure 5.4.8, panel (b) and 5.4.9, panel (b) was performed[7].

---

[7]The cantilever was previously calibrated in order to derive its magnetic and imaging properties (cf chapter 1.3). The calibration measurements were performed on the calibration sample provided from Hitachi

From a comparison of the different MFM–contrast levels in figure 5.4.5 it was found that eight of the ten Co/Pt-multi-layers[8] form the initial strong MFM–contrast in external fields below -843 mT and +670 mT respectively. Above these fields, the MFM–contrast of the nucleated domains becomes very weak leading to the assumption that this contrast is due to domain formation in the lowest two FM–layers of the sample, marked as layers zero and one in figure 5.2.1. In addition, the images of the MFM field loop clearly show a two step reversal process in these two layers.
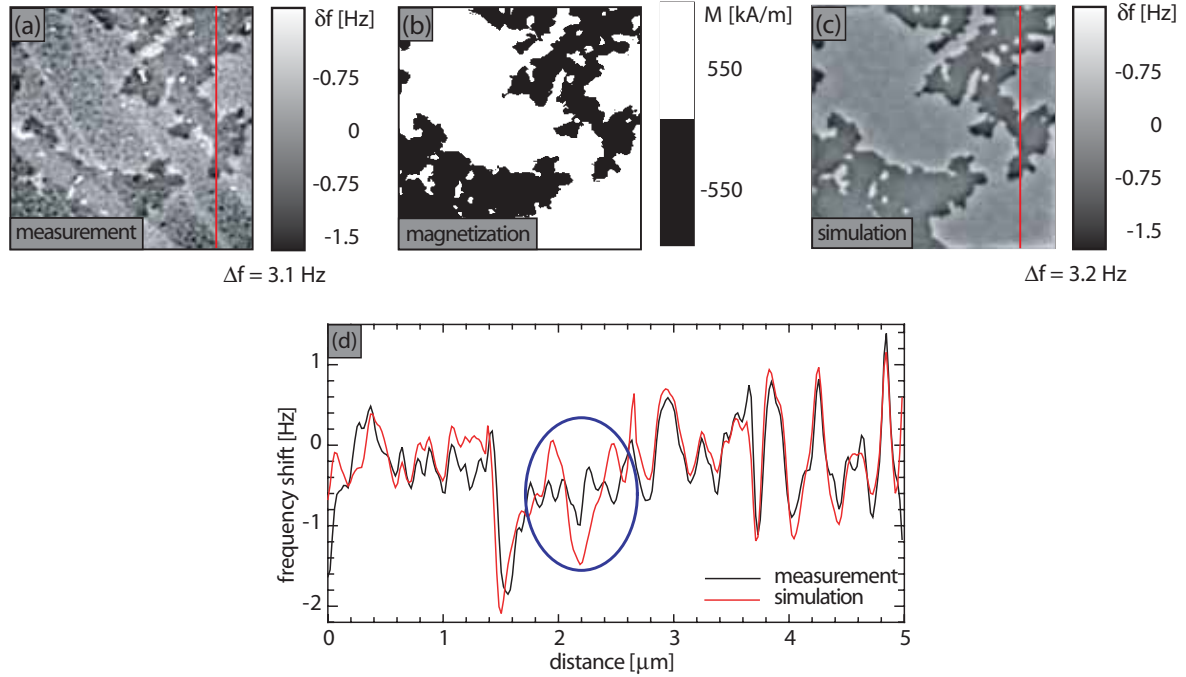
Fig. 5.4.13: Calculation of the MFM contrast arising from FM–layer one. Panel (a) shows the measurement, panel (b) the magnetization distribution derived by a discrimination process. Panel (c) depicts the MFM simulation. The domain pattern and the contrast range agree extremely well. However, the fine details of the domains of the measurements could not be obtained. This is visible in the line section depicted in panel (d), taken from the measured and simulated MFM images along the red lines.

The analysis for image 5.4.8, panel (b) is pursued first. For the calculation, it was assumed that the magnetization direction of the FM–layers two to nine was parallel to the external field direction over the whole scan area. This is fulfilled to a good approximation. When FM–layer one forms domains in the field direction, the magnetization of the last FM–layer was assumed to still be aligned against the field direction. Therefore, FM–layers zero and two to nine will not contribute to the measurement signal[9]. In addition, the contribution from the uncompensated spins at the AF–FM interfaces as well as the influence of the topography

---

Global Storage Technologies. Images of 5.0 × 5.0 μm with 256 × 256 pixels were taken in order to calibrate the tip for the same scan acquisition parameters as used for the field loop experiments. The maximum lateral magnetic resolution was found to be better than the data point resolution of 19.5 nm and the peak stray field at the tip apex was calculated to be 7.6 mT.

[8]Throughout the rest of this chapter, the Co/Pt-multi-layers will be simply called FM–layer.

[9]This is easily derived from the fact, that a homogenous, perpendicular magnetized thin film, extending infinitely in the directions of the plane, does not produce a stray field outside this plane. The sample at hand is clearly finite; however, it can be approximated to be infinite compared to the area relevant for the magnetic tip–sample interaction.

on the MFM–contrast was neglected.

In a first step, the magnetization distribution was computed from the MFM measurement, depicted in figure 5.4.13, panel (a), by a discrimination process. A saturation magnetization value of 550 kA/m was used as found by SQUID magnetometry measurements [102] performed at 10K. The magnetization image is depicted in panel (b). With the aid of equation 1.1.8 in chapter 1.1, the stray field of the sample could be computed at the tip–layer distance of the MFM measurement. The tip–sample separation was calculated from the distance between tip and sample surface and the location of layer one in the sample (87.5 nm). By calculating the convolution of the stray field with the tip transfer function determined in the calibration process, an MFM image was simulated. It is depicted in panel (c). The domain pattern and the contrast range agree extremely well with the measurement in panel (a). However, the fine details of the domains of the measurements could not be obtained. This is visible in the line section depicted in panel (d), taken from the measured and simulated MFM images along the red lines. The strongest deviations can be observed in the area marked in blue. The discrepancy is due to the procedure to obtain the magnetization pattern[10].

The same procedure was also performed for the image in 5.4.9, panel (b). Figure 5.4.14, panel (a) depicts again an MFM measurement, while panel (b) shows the magnetization distribution. Panel (c) shows the simulated MFM image. Again the domain pattern and the contrast range agree extremely well. In addition, the line sections of the measurement and the simulation in panel (d) are in very good agreement. Deviations, as found in panel (d) of figure 5.4.13, are not visible.

In figures 5.4.13 and 5.4.14, the simulated MFM images are in very good agreement with the measurement. However, a comparison of the contrast ranges in the measured and the simulated images of both FM–layers shows the same difference of 0.3 Hz. In addition, the signal to noise ratio is small in the MFM measurements. Therefore, it is essential to test whether the assumption about the location of these two layers within the sample is valid. In order to carry out the verification, the magnetization distribution of FM–layer zero and one was assumed to be in the location of layers zero to four in the sample. Again, the stray fields of the magnetization distribution were calculated at the tip apex. From the stray fields, MFM images were then simulated. In order to compare the calculated images with the MFM measurement, frequency shift histograms of the measurements and the simulations were computed. The histograms were fitted using a Gauss function:

$$f(x) = \frac{A}{\sqrt{2\pi}} e^{\frac{(x-x_0)^2}{2\sigma}}, \tag{5.4.1}$$

with A and $4 * \sigma$ being the height and the full width half maximum (FWHM) of the Gauss function. Figure 5.4.15 shows the result of the Gauss function fit for the MFM measurement (panel (a)) and the simulation (panel (c)) of layer one. For the simulation, its magnetization distribution was in the location of layer one. Panels (b) and (d) show the frequency histograms and the Gaussian fits. The black crosses denote the histogram points whereas

---

[10]In an MFM measurement of a domain pattern with either parallel (dark domains) or antiparallel (bright domains) alignment of the magnetization to the tip magnetization, two distinct contrast levels can be observed. In a histogram plot of such an MFM measurement, the two distinct contrast levels will be reflected in two well separated peaks. The peak at positive frequency shifts results from the bright domains whereas the peak at negative frequency shifts is caused by the dark domains. The discrimination level is then centered in between the two peaks. If the MFM–contrast weakens, because the tip–sample separation becomes larger or the sample stray field becomes weaker, the two peaks will approach each other and finally merge into one peak centered around zero frequency shift. For images showing only one peak in the histogram, it is sometimes difficult to find a suitable discrimination level. Therefore small variations of the MFM signal within a domain can lead to a wrong magnetization pattern in these areas.
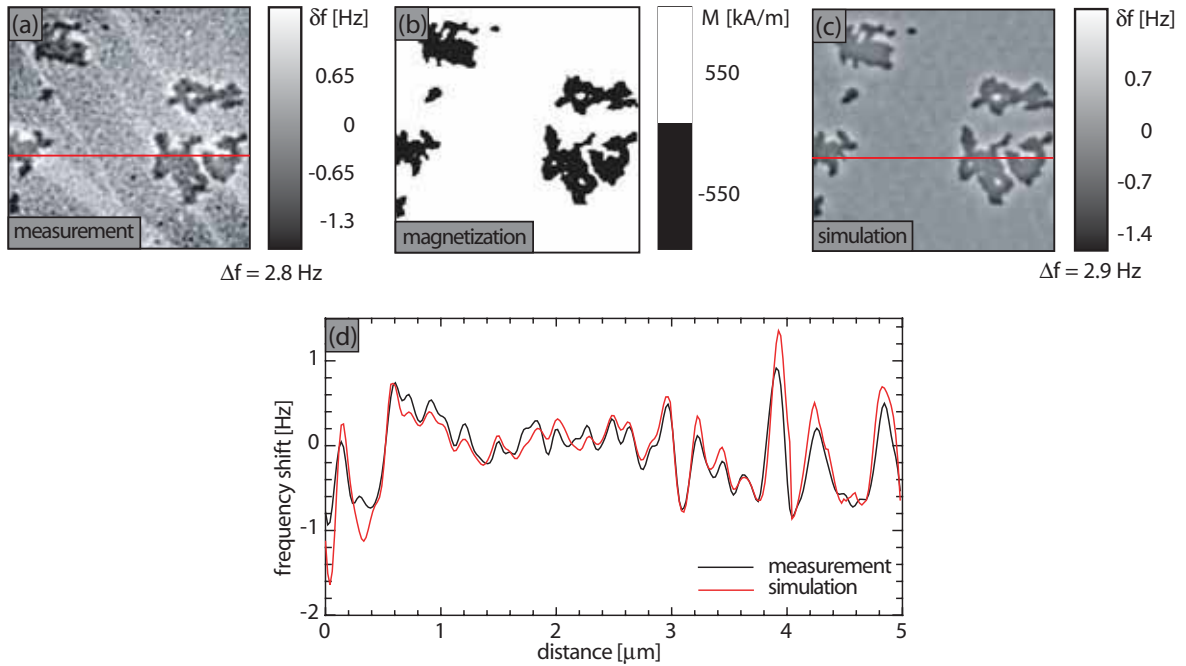
Fig. 5.4.14: Calculation of the MFM contrast arising from FM–layer zero. Panel (a) shows the measurement, panel (b) the magnetization distribution. Panel (c) depicts the MFM simulation. The domain pattern and the contrast range agree extremely well. Also, the fine details of the domains of the measurements could be reproduced. This is visible in the line section depicted in panel (d), taken from the measured and simulated MFM images along the red lines.

the red solid line shows their Gaussian fits. The FWHM of the Gaussian curves fitted to the measured and simulated histograms are in excellent agreement. For comparison, the solid green and blue curves denote the Gaussian fits for the frequency shift histograms calculated from the MFM simulations. the latter result from the magnetization distribution of layer one assumed to be in the location of layers zero and two. As expected, their FWHM values do not agree with the FWHM value of the Gauss curve fitted to the measurement histogram.

Table 5.4.3 shows the result of the location verification for FM–layer one. The notation *in level x* denotes the magnetization distribution of FM–layer one being at the location of layer x in the sample. As expected, the frequency shift range as well as the FWHM of the Gaussian fits increase with decreasing tip–layer distance. There is a very good agreement of the frequency shift range as well as the full width at half maximum value between the measurement and the simulation *in level* 1.

	Contrast range [Δf]	FWHM of Gaussian fit
measurement	3.1 Hz	1.09 Hz
in level 0	2.9 Hz	1.05 Hz
in level 1	3.2 Hz	1.11 Hz
in level 2	3.7 Hz	1.20 Hz
in level 3	4.4 Hz	1.37 Hz
in level 4	5.4 Hz	1.66 Hz

	Contrast range [Δf]	FWHM of Gaussian fit
measurement	2.8 Hz	0.99 Hz
in level 0	2.9 Hz	1.01 Hz
in level 1	3.3 Hz	1.12 Hz
in level 2	3.8 Hz	1.25 Hz
in level 3	4.6 Hz	1.38 Hz
in level 4	5.7 Hz	1.70 Hz

Table 5.4.1: Summary of the simulations for layer 1.   Table 5.4.2: Summary of the simulations for layer 0.
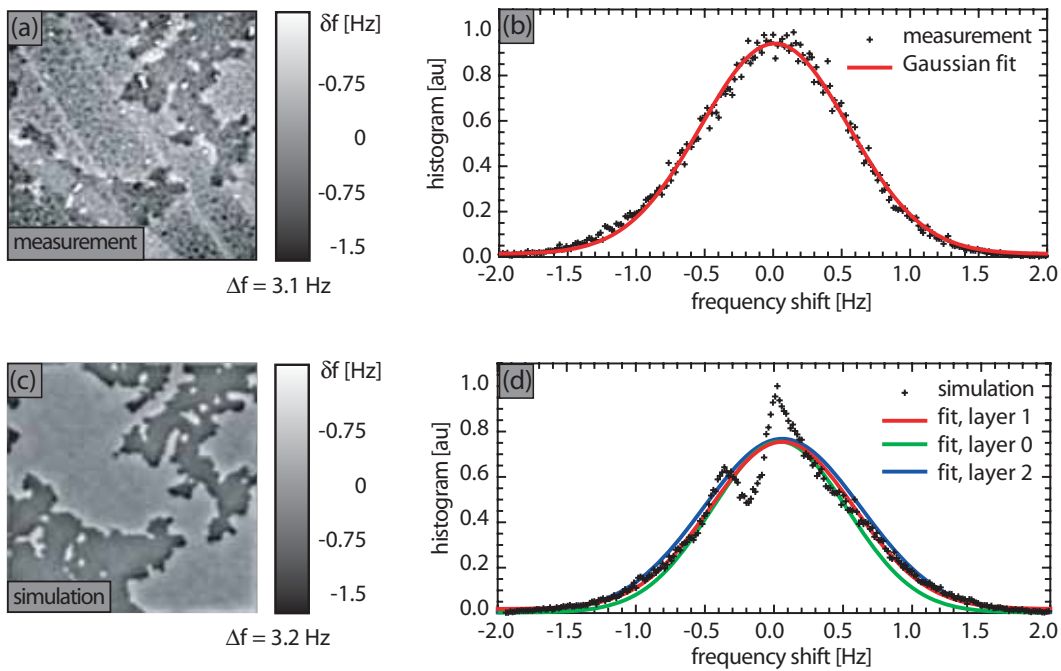
Fig. 5.4.15: Verification of the position FM–layer magnetization distribution in the sample. Depicted in panels (a) and (c) are the MFM measurement and the simulation with the magnetization distribution of layer one being in layer one. Panels (b) and (d) show frequency shift histograms (black crosses) of the images in panels (a) and (d). The red lines denote a Gaussian-fit with equation 5.4.3.

The same verification was performed for the magnetization distribution of FM–layer zero. Again, its magnetization pattern was assumed to be at the location of layers zero to four in the sample and simulated MFM images were calculated accordingly. The frequency shift histograms of the simulations were also fitted with the Gauss function in equation 5.4.3. Table 5.4.3 summarizes the results found for the frequency shift range as well as the FWHM of the Gauss function. The agreement of the FWHM of the Gaussian curve fitted to the measurement histogram with the one of the simulation *in level 0* is excellent.

The result clearly shows that the weak domain structure observable in panels (b) of figure 5.4.8 and 5.4.9 is formed in the lowest two layers of the sample, when an external field larger than -843 mT is applied. In order to make sure that the domain formation seen in the positive field branch above +640 mT is due to the magnetization reversal in the last two FM–layers, the verification was repeated. The two FM–layers reversing in high external fields were again identified as the lowest two layers in the sample.

5.4.4 Origin of strong contrast in intermediate fields

The calculations in the previous section have revealed that the weak MFM–contrast in the measurement appearing in fields larger than -843 mT and +640 mT respectively, is due to the formation of domains in the lowest two FM–layers of the sample. In order to understand the domain reversal of the whole magnetic multi-layer sample in the field loop, the origin of the MFM–contrast in external fields between -803 mT and +640 mT has to be analyzed. In order to carry out this analysis, the image taken in -674 mT field, depicted in 5.4.4, panel (d) was used. It shows a variety of line–like domains as well as large two-dimensional domains. These domains are situated in the upper eight layers of the sample, denoted by layer two to nine in

figure 5.2.1. For the calculation, it was assumed that the magnetization distribution of the lowest two ferromagnetic layers is still uniformly antiparallel to the field direction. Therefore, they are not contributing to the MFM–contrast. Furthermore it was assumed that the eight FM–layers do not reverse completely independent of each other. A layer can only start to reverse its magnetization in a certain area when all layers above it have already reversed their magnetization at this location.

The magnetization pattern of the eight different frequency shift levels were identified using
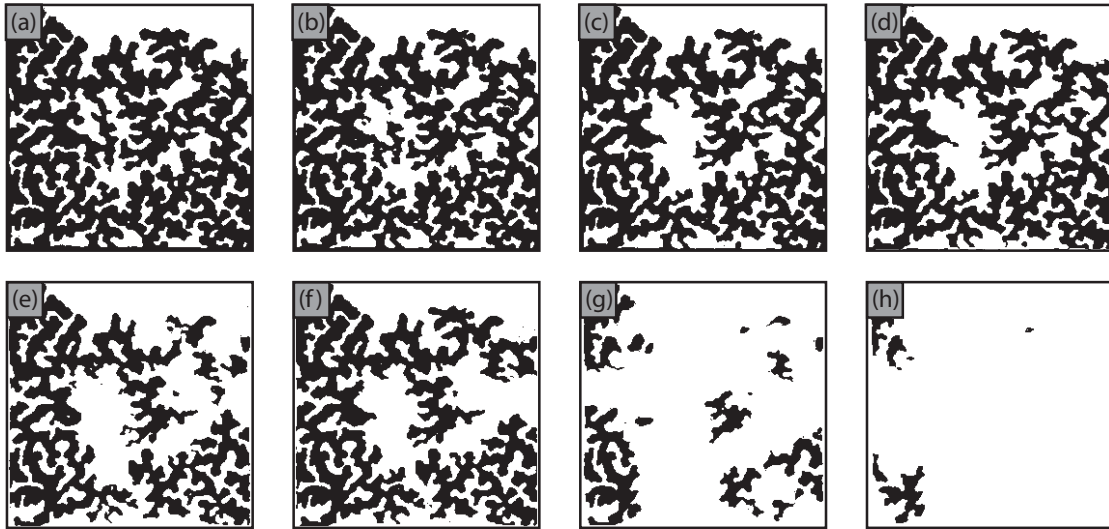
Fig. 5.4.16: Panels (a) to (h) depict the magnetization patterns for the eight different layers found by the discrimination procedure.

the same discrimination method as already applied in the previous chapter. They are depicted in figure 5.4.16, panel (a) to (h).

With the aid of the magnetization patterns and their locations in the FM–layers of the sample, a stray field image of the sample was calculated at the height of tip–sample separation in the MFM measurement (37.8 nm above the sample). In a second step, an MFM simulation was computed using the tip transfer function determined in the tip calibration process. The MFM measurement, along with the simulation, are shown in figure 5.4.17, panels (a) and (b). The agreement between the domain pattern and the MFM–contrast in both images is excellent. The frequency shift range only differ by 0.7 Hz which is less than 5% error. The reason for the remaining difference of measurement and simulation may be due to domain structures distributed into wrong FM–layers in the determination of the layer–wise magnetization patterns. Figure 5.4.17, panels (c) and (d) show a horizontal and a vertical line section through the measured (black curve) and simulated (red curve) MFM images respectively. The agreement is very good, the peak values and even the fine structures are reproduced. However, in one area in panel (c) and in three areas in panel (d), the agreement is not satisfactory. Here, the simulation is larger than the measurement. However, by remapping the domains in these areas, a much better agreement is obtained. This is indicated by parts of the blue dotted curve in both panels. In order to achieve better agreement between measurement and simulation in panel (c), the domain marked by arrow one was attributed to four instead of six FM layers. In panel (d), the domain indicated by arrows two was only attributed to seven instead of eight FM layers.
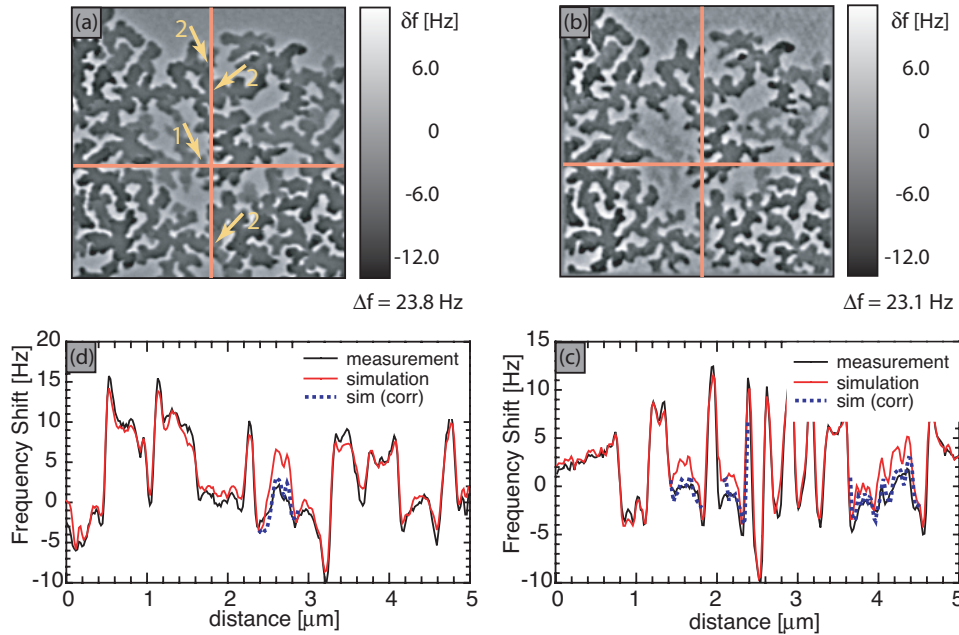
Fig. 5.4.17: Comparison of the original MFM measurement (panel (a)) with the calculated MFM image in panel (b). The domain features as well as the overall frequency shift range are very well reproduced in the simulation. Panels (c) and (d) show horizontal and vertical line sections through both images. In one area in panel (c) and three ares in panel (d), the agreement between the red curve taken from the simulation and the MFM measurement is not satisfactory. By remapping the domain structure at these positions into other FM–layers, a much better result could be obtained, depicted by the blue dotted curve in panels (c) and (d).

5.4.5 Discussion of the different nucleation behaviour in the sample

In the MFM images of the field hysteresis loop two distinct domain nucleation and reversal paths can be identified. Between fields of -664 mT and -803 mT and between +440 mT and +640 mT, domains nucleate and reverse in layers two to nine in the sample. The volume fraction of changed magnetization per FM–layer is small in each field step, but all eight layers contribute to the overall magnetization reversal. In fields larger than -803 mT and +640 mT, the magnetization of these eight FM–layers is almost completely aligned with the external field direction. Only then do the lowest two layers in the sample start to form domains, now with a large change of magnetization volume per field step. Therefore the change in domain reversal paths was not detected in the SQUID magnetometry measurements. At -664 mT and +440 mT, a sudden nucleation of domains occurs (panel (b)). This nucleation could be induced by the tip. From figure 5.4.18 it can be observed that the tip stray field at the position of the upper most FM–layer in the sample (layer nine) still has a magnitude of 3 mT. The coercitive field of the tip is much lower than the nucleation field of the sample, therefore the tip field and the external field are aligned in parallel. The tip field locally enhances the external magnetic field. The SQUID magnetometry measurements showed that the onset of nucleation is very sharp, therefore, a local change in the magentic field of 3 mT might be enough to trigger domain nucleation at a grain with a smaller anisotropy value[11] than the

---

[11] Due to the growth method of the layers, an anisotropy distribution formed in the sample. This distribution depends strongly on the pressure in the deposition chamber during sputtering as described by Pierce *et al.* [120].
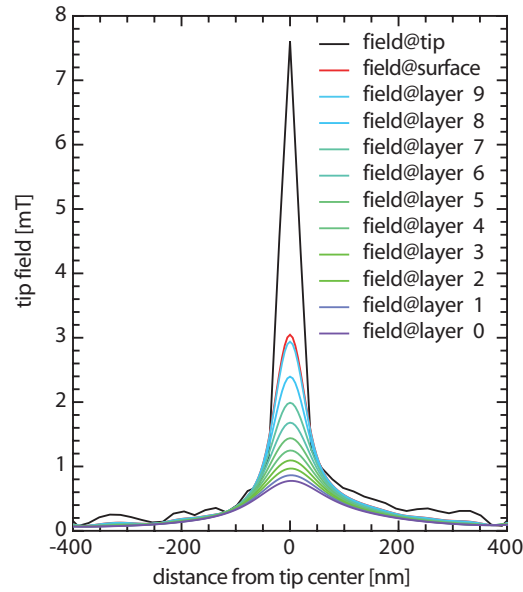
Fig. 5.4.18: Magnetic stray field of the tip at various distances from the tip apex. The black curve denotes the tip field directly at the tip apex as calculated in the calibration process of the cantilever. The red curve denotes the field at the surface of the sample, the blue and green shaded curves show the field at the position of the first eight FM–layers and the last two in the sample, respectively.

average value.

In order to determine the exact nucleation field, the stray field from the tip was disturbing. It was not possible to get a reliable value for the nucleation field with an error of less than 2 mT. More stable imaging conditions were expected by first ramping the external field up to a certain value and back to remanence and then performing the MFM measurement. In doing this, the tip stray field does not have any influence on the onset of domain nucleation during the scan. However, the values for the nucleation field found by this method had the same uncertainty of 2 mT. The determined nucleation fields were on average 2 mT to 4 mT larger. These values are in very good agreement with the field of the tip at the position of the ninth FM–layer in the sample and confirm the initial assumption about the nucleation of domains by the tip stray field in this FM–layer.

Once domains are nucleated at -664 mT and +440 mT, domain reversal proceeded horizontally (within the layers) and vertically (throughout the first eight layer). However, the vertical reversal stopped abruptly in the location of layer two on both branches of the hysteresis loop. In principle, there are three different reasons which could prevent the domain formation proceeding into the lowest two layers of the sample. Firstly, the tip field in alliance with the external field might be strong enough to nucleate domains in the first eight layers but too weak to overcome the anisotropy of the grains in the lowest two layers. However, the difference between the tip stray field at the second and first layer in the sample is very small, about 0.1 mT. If the tip stray field was strong enough to nucleate domains in layer two, this also would take place in in layer one.

The second reason is that the exchange bias from the antiferromagnetic layers is stronger for the lowest two FM–layers. This would result in a higher nucleation field on the biased side of the hysteresis loop, but conversely in a lower nucleation field on the other loop branch. Such behavior is not observed in MFM measurements. The lowest two layers in the sample form domains only in high fields on both branches of the magnetization loop.

Lastly the average anisotropy value in these layers might be larger than in the upper eight

layers. This could be connected to a more uniform growth condition for these FM–layers. As a consequence of this, the layers would have a smaller number of structural defects resulting in a smaller number of nucleation centers in the layers leading to a nucleation of domains in higher fields. Indeed, in figure 5.4.9, panel (a), only five nucleation centers can be observed in the whole image (red circles) whereas in the image in panel (a) of figure 5.4.10, already five nucleation spots can be seen in the upper half of the image (blue circles).

5.5   Sample cooled in zero field

In the last section, the sample was cooled down through its Néel temperature in a field high enough to saturate all ferromagnetic layers. As a consequence, the antiferromagnetic layers were not preset with a domain structure at the ordering temperature and adjusted themselves in one of their own energy minima. The result was a macroscopically noticeable exchange bias effect.

No exchange bias is expected, if the AF layers are preset with an equal fraction of domains with a magnetization direction parallel and antiparallel to the tip magnetization. Such a domain configuration can be obtained by demagnetizing the sample in an in-plane field at room temperature. The in-plane magnetic field couples to the in-plane component of the magnetization and aligns the domains in stripes parallel to the field direction. A structure of up and down domains with equal volume fraction emerges. Cooling the sample through T_N imprints this pattern into the CoO layers. One then expects that the sample will have locally biased regions depending on the local magnetic direction of the FM–layer [103], but no macroscopic exchange bias. Consequently, there is no hysteresis loop shift as shown in figure 5.3.3, panel (a) by the red open squares. The FM domain pattern was prepared at Hitachi Global Storage Technologies (San Jose, USA).

5.5.1   The hyteresis loop cycle

Upon cooling through the Néel temperature, the stripe domain configuration of the FM–layer was copied into the AF–layer. All experiments in this chapter were performed at 8.0 K with an average tip-sample distance of 30±2 nm in constant height mode. The field was varied between +7.0 T and -7.0 T[12] and a large amount of images were taken. Again, only a fraction of all measurement data is shown. The images were selected to represent different stages of the domain formation in the sample. They are depicted in figures 5.5.19 and 5.5.20. Figure 5.5.19 shows the domain formation on the positive field branch of the hysteresis loop in fields spanning from remanence to +7.0 T and back. The image in panel (a) was taken directly after cooling down the sample. As expected, the domain structure formed in the FM–layers by the demagnetization process, is visible. The domains have an average width of 85 nm and stretch over several micrometers in length. Upon ramping the field up to +500 mT in panel (b), the domains with a magnetization direction opposing the external field direction (bright domains) shrink reversibly in favour of the domains with magnetization direction parallel to the field direction (dark domains). At +650 mT, the bright domains additionally start to shrink in a non-reversible way by reducing their length. The reduction always starts at the end points of the domains, at sharp bends or at bifurcations (panel (c)). The circles one and two in panel (b) and (c) elucidate this behaviour. In a field of +700 mT, the length of the bright domains is further reduced. In addition, point like domains have emerged. These form out from the stripe domains, and are very persistent against annihilation.

In panel (e) at +800 mT, a sudden change in MFM–contrast is visible. The contrast range has dropped by a factor of more than 20 and the domain structure is much more grainy. In the remainder of this chapter, this kind of contrast will be called *AF–contrast* whereas the strong contrast in low external field is called *FM–contrast*. The grainy magnetic structures have a length scale of 50 nm to 80 nm and arise from the uncompensated spins at the AF–FM

---

[12]Here, a positive field is defined as being aligned with the initial magnetization direction of the cantilever tip.
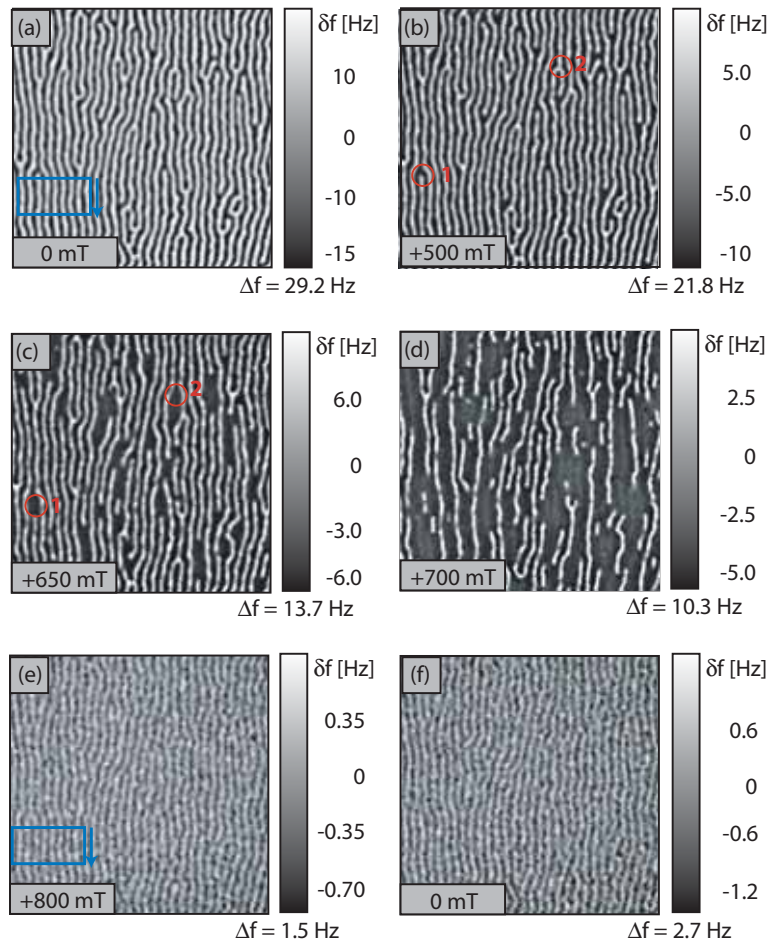
Fig. 5.5.19: Different stages of domain formation of the positive branch of the hysteresis. Panel (a) is taken in zero field directly after cooling, panel (b) in +500 mT. The width of the bright domains decreases. Panel (c) is measured in +650 mT and shows a contraction in length of the bright domains. In addition, point–like domains are forming, as shown in panel (d) at a field of 700 mT; in panel (e) at +800 mT field, only a weak and grainy MFM–contrast remains. Panel (f) finally, is taken in remanence; the weak contrast persists. All images have a size of 5μm $\times$ 5μm.

interfaces. The AF–contrast remains stable until high fields of 7.0 T, but the contrast range decreases by a factor of 3.5 throughout the next 6.2 T. The contrast persists when ramping the field back to remanence (panel (e)) only its contrast range increases again to 2.7 Hz.

Figure 5.5.20 shows different stages of domain formation on the negative branch of the hysteresis. Panel (a) is taken in a field of -66 mT. The grainy stripe domain contrast is reversed compared to the image in figure 5.5.20, panel (f) because the tip magnetization has flipped into the new field direction at -65 mT. Panel (b) measured in -300 mT shows again FM–contrast. Very large dark domains have formed in the FM–layers, their width being a multiple of the stripe domain width in panel (a) of figure 5.5.19. Due to the large demagnetization fields within these large domains, their stray field is reduced in the center. The faint grainy stripe contrast seen in the high field images becomes visible. It can be observed that the large FM–domains always cover an odd number of the stripes and are always bordered by dark stripes. The bright domains which have nucleated in the FM–layer have the same width as the original stripe domains and run on top of dark stripes. In a field of -400 mT (panel (c)), an even ratio of up and down domains has emerged again. The magnetization distribution precisely reflects the one in panel (a) of figure 5.5.19. This shows that unlike the domain
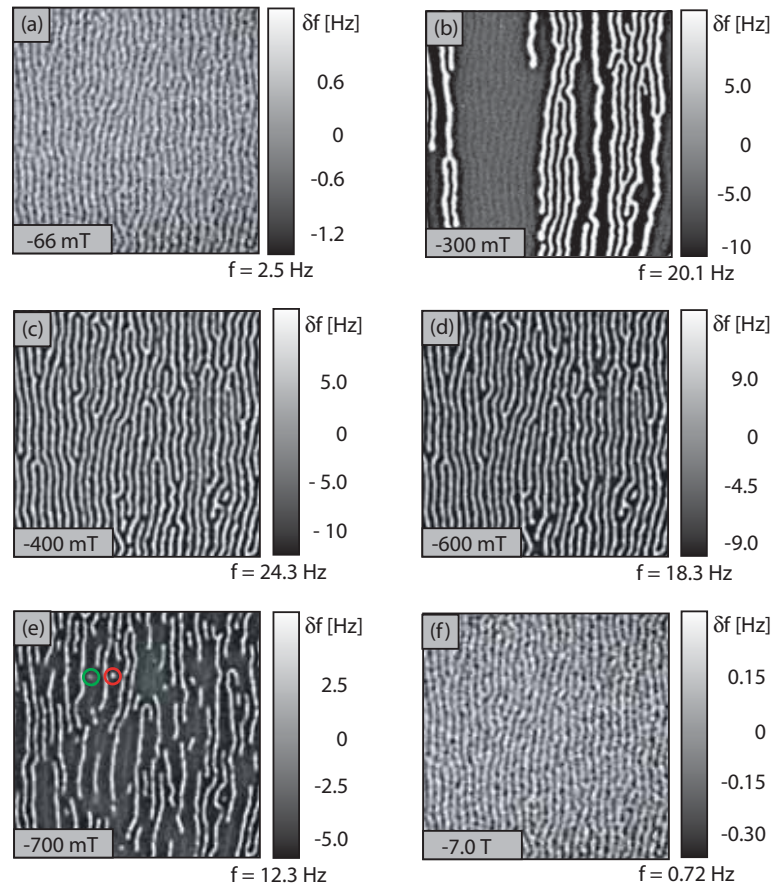
Fig. 5.5.20: Different stages of domain formation of the negative branch of the hysteresis. Panel (a) is taken in a field of -66 mT. The grainy stripe domain contrast is reversed compared to the image in figure 5.5.20, panel (f) because the tip magnetization has flipped into the new field direction at -65 mT. Panel (b) measured in -300 mT shows again FM–contrast. Very large dark domains have formed in the FM–layers. The dark domains which have nucleated, have the same width as the original stripe domains. In a field of -400 mT (panel (c)), an even ratio of up and down domains has emerged again. The magnetization distribution precisely reflects the one in panel (a) of figure 5.5.19. Panels (d) and (e) acquired in fields of -600 mT and -700 mT respectively, show the same stages of domain reversal as already seen on the positive branch of the hysteresis loop. Panel (f) depicts an MFM image taken in -7.0 T field. The grainy contrast is still visible, but the contrast range as decreased to 0.72 Hz. All images have a size of $5\mu m \times 5\mu m$.

formation in the saturation field cooled case, the localized biased regions in the FM–layers return to their original domain configuration.

Panels (d) and (e) acquired in fields of -600 mT and -700 mT respectively, show the same stages of domain reversal as already seen on the positive branch of the hysteresis loop. In panel (e) again, point–like domains have formed. This could be due to the formation of a 360° Bloch domain walls upon the collapse of the stripe domains. These walls are very stable against annihilation because they can only be destroyed by breaking the 360° spin chain in high fields (green and red circles in panel (e)). The point–like domain in the red circle has a higher MFM contrast than the one in the green circle. This may be due to the penetration of the domain in the red circle through all FM–layers in the sample whereas the domain in the green circle was only formed in some of the layers. However, this behavior was only observed for the point–like domains, never for the stripe domains of the FM– or AF–contrast.

The strong FM–contrast vanishes at -800 mT. Panel (f) depicts an MFM image taken in -7.0 T

field. The grainy contrast is still visible, but the contrast range has decreased to 0.72 Hz.

Comparing the onset of nucleation in the FM–layers on both branches of the field loop, a very small deviation of 5 mT can be found. On the negative branch, the nucleation of domains in the FM–layers starts at -284 mT, whereas it starts at +279 mT on the positive branch. Interestingly, the onset of the AF–contrast, which essentially reflects the saturation field of the FM–layer, has a larger deviation for both branches. On the negative side of the loop, the onset lies at -792 mT whereas on the positive side, the FM–layers are already saturated in a field of +775 mT. This deviation of 17 mT which has the same sign as the deviation for the onset of nucleation in the FM–layers, has been repeatedly measured in field cycles.

5.5.2 Origin of the contrast inversion on different branches of the loop

After the saturation of the FM layers in a field above 800 mT, the original domain structure can be regained by ramping the external field up to about 400 mT on the opposite hysteresis loop branch. However, upon close inspection of two images taken in +400 mT and -400 mT
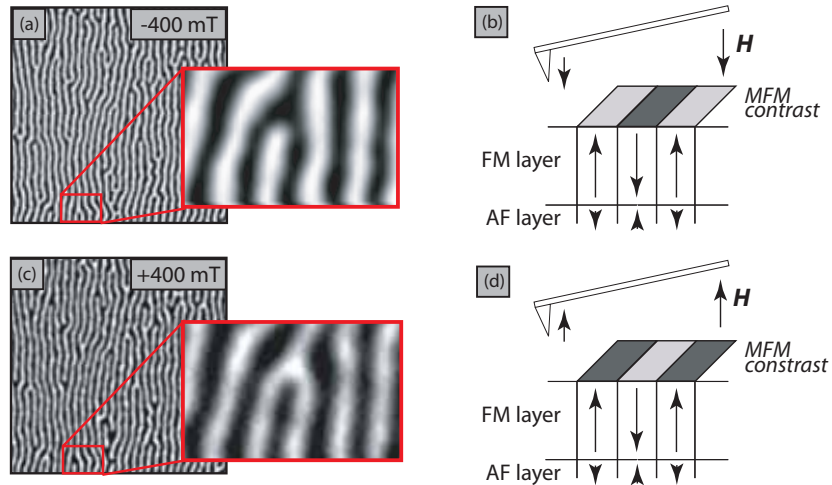
Fig. 5.5.21: Contrast inversion of the domain pattern on the positive and negative branch of the field cycle. The inversion in the images of panels (a) and (c) is due to the reversal of the tip magnetization in low fields. In subsequent measurements is always aligned with the external field whereas the FM–domains, biased by the AF–domains stay with their magnetization fixed (panels (b) and (d)). The images in panel (a) and (c) have a size of 5μm $\times$ 5μm.

at the same lateral scan coordinates, a inversion of the MFM contrast is visible. This is depicted in figure 5.5.21, panels (a) and (c). The zooms show a characteristic feature in the scan image, for easy comparison. Once the domain bifurcation is imaged with dark contrast and once with bright contrast. The contrast inversion is due to the alignment of the tip magnetization with the external field when the latter is increased. The image in panel (a) is taken on the negative loop branch. After decreasing the field back to zero and increasing it on the other side of the hysteresis loop, the tip magnetization switches into the new field direction at 65 mT. However, the magnetization direction of the FM–layers is preset by the coupling to the AF–layers, therefore its direction persists. Consequently, the interaction of the tip with a particular repulsive domain on one loop branch becomes attractive on the other, so the MFM contrast of the two images is inverse. This is shown in the drawings in panels (b) and (d) of figure 5.5.21. Due to the alignment of the tip magnetization with the field direction on both sides of the loop, the domains with a magnetization direction antiparallel to the external field will always be imaged as bright domains.

5.5.3   Origin of the contrast inversion within the same loop branch

In external fields above about 800 mT, the FM–layers are saturated in the field direction and do not contribute to the measurement signal anymore. The very weak and grainy AF–contrast appears. This contrast is still of magnetic origin because it matches exactly the domain pattern visible in the FM–contrast. Furthermore, the contrast has no similarity with the underlying topography shown in figure 5.4.12.

By comparing panels (a) and (e) in figure 5.5.19 as well as panels (d) and (f) in figure 5.5.20, it can be observed that AF– and FM–contrast are inverse on the same loop branch. In order to illustrate this fact, line sections at identical locations in panels (a) and (e) in figure 5.5.19 are shown in figure 5.5.22. In order to improve the signal to noise ratio, the line sections were averaged over the area in the blue boxes in direction of the arrow. The stripe domains inside this area are very well aligned, so that the geometric error induced by the averaging process is negligible. The black and red curves show the line section from panel (a) and panel (e) respectively. The red curve was enlarged by a factor of 10 to be comparable to the black curve. The curves show a colinear but antiphase alignment. This concludes that the initial
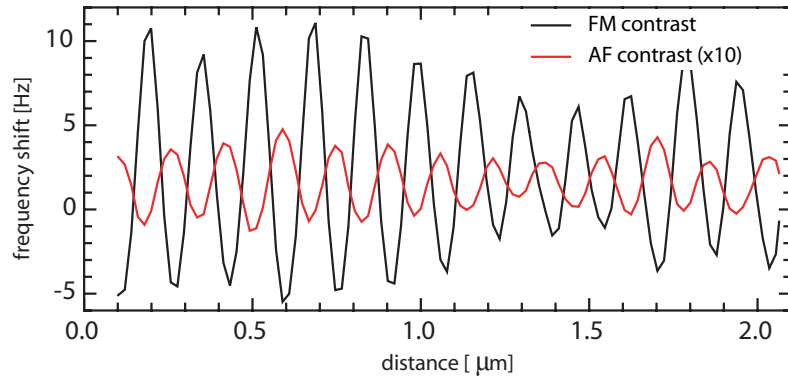
Fig. 5.5.22: Averaged line sections of images with FM and AF–contrast. The boxes in figure 5.5.19 (a) and (e) indicate the area of the line section. Clearly, a colinear but antiphase alignment of the domains is visible.

domain state prepared in the FM–layers at room temperature was indeed copied into the AF–layers upon cooling through the Néel temperature. Furthermore, the contrast inversion reveals an antiferromagnetic alignment of the spins in the FM–layer and the uncompensated spins at the AF–FM interfaces. This suggests a magnetic super-exchange interaction via the oxygen atoms. The direct exchange between the cobalt ions in the CoO is very weak,
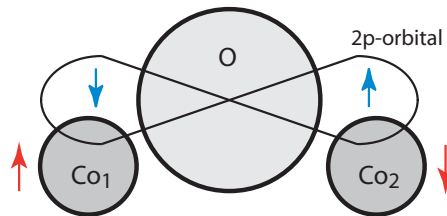
Fig. 5.5.23: Illustration of the super-exchange interaction between to Co ions mediated by an O^{2-} ion. The red arrows indicate the total spin of the Co ions, the blue arrows, the spins of the O^{2-} $2p$ electrons.

because it is interrupted by the interstitial O^{2-} ions. However, a super-exchange interaction can act between the Co ions mediated by the O^{2-}, an idea introduced by Kramers [121]

and theoretically developed by Anderson [122]. The essential point of this mechanism is as follows: The O^{2-} ion has an electronic structure expressed by $(1s)^2(2s)^2(2p)^6$. The p-orbitals stretch towards the neighboring Co ions, Co_1 and Co_2 as shown in figure 5.5.23. One of the p-electrons can transfer to the $3d$ orbit of one of the Co ions (eg Co_1). In this case, the electron must retain its spin, so that its sense will be antiparallel to the total spin of the Co^{2+}, because the Co^{2+} has already had seven electrons and the vacant orbit must accept an electron with spin antiparallel to that of the seven electrons (Hund's rule). On the other hand, the remaining electron in the p-orbital must have a spin antiparallel to that of the transferred one because of the Pauli exclusion principle. The exchange interaction with the other Co ion (Co_2) is therefore negative. As a result, the total spin of Co_1 becomes antiparallel to that of Co_2. An in-depth coverage of this effect has been published by Nagamiya *et al.* [123].

5.5.4 Conclusions from the examination of the field loop images

From the MFM images presented in section 5.5.1 and the MFM contrast inversions addressed in the two previous subsections, the following conclusions can be drawn:

1. The hysteresis loop shows that the FM–layers are fully saturated in fields larger than 800 mT. The AF–layer withstands a ferromagnetic ordering by the external field even in high fields of 7.0 T. Therefore the magnetic contrast visible in figure 5.5.19, panels (e) and (f) as well as in panel (f) of figure 5.5.20 result from uncompensated spins at the interfaces of the AF–layers.

2. The contrast inversion found when comparing panels (a) and (e) in figure 5.5.19 as well as panels (d) and (f) in figure 5.5.20, reveals an antiferromagnetic alignment of the spins across the AF–FM interfaces.

3. The granular structure of the domain pattern shown in figure 5.5.19, panels (e) and (f) as well as in panel (f) of figure 5.5.20 is reproducible and its length scale is comparable to the structural grain size (15-50 nm). This suggests that the distribution of the uncompensated spins is not spatially uniform but is linked to the granular microstructure of the film.

4. The large reduction of the MFM–contrast, upon the increase of the external field above saturation field of the FM–layers suggests that only a very thin layer, possibly only a fraction of a monospin layer is uncompensated. This has in fact been observed by a number of authors [92, 109, 124, 125].

5. The further (slow) decrease of the AF–contrast range in external fields from 800 mT to 7.0 T suggests of a gradual rotation of the interfacial spins of the AF–layer.

In order to understand the nature of the FM and AF–contrast, a quantitative analysis of the MFM data was performed. The main focus was set on verifying if all ten FM–layers of the multi-layer sample contribute to the FM–contrast and also whether it would be possible to extract the approximate amount of uncompensated interfacial spins responsible for the weak AF–contrast. A third issue was to compare the MFM images taken in high field to theoretical models accounting for the exchange bias effect and evaluate their capability in explaining the observed effects. The last two issues are discussed in the following two sections whereas the origin of the FM–contrast is explained in this section.

5.5.5   Quantitative analysis of the FM–contrast

The images of the hysteresis loop displayed in figures 5.5.19 and 5.5.20 were taken under the same experimental conditions and with the same cantilever as used for the measurements for the saturation field cooled case. Therefore, the tip transfer function determined by the calibration process in chapter 5.4 could be reused for the calculations in this chapter. For the verification of the FM–contrast, a sub-image cut out from the upper left corner of the image in panel (a) of figure 5.5.19 was chosen. A simulation of the MFM contrast was computed and compared to the measurement, in the same way as already performed for several images from the hysteresis loop of the saturation field cooled case.
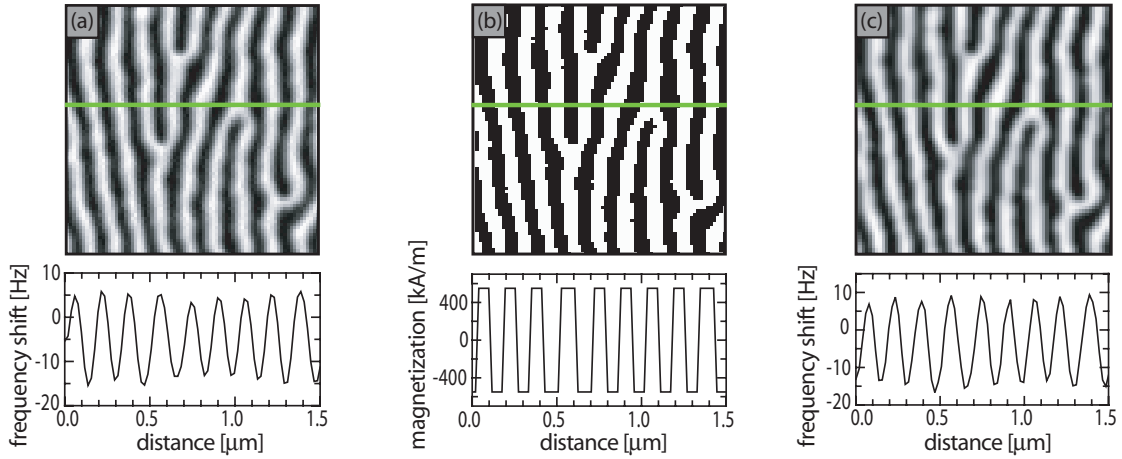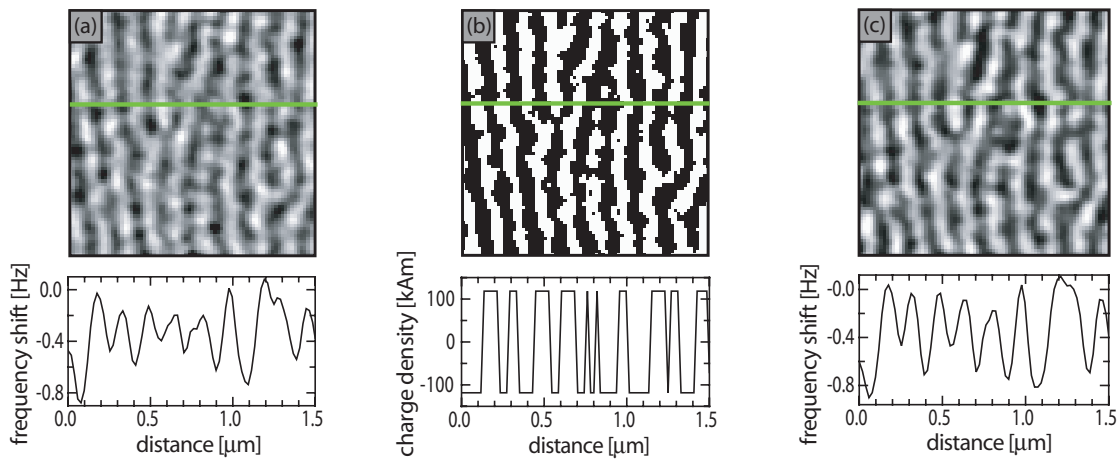

Fig. 5.5.24: Panel (a) shows an MFM image and cross section after zero–field cooling. Panel (b) depicts the magnetization pattern and cross–section generated from the MFM image. The modeled and measured grey scale images in panels (a) and (c) agree extremely well, when the saturation magnetization of 550 kA/m is used for the calculation. From this analysis it is apparent that the stray field emanates from a single, unique domain structure in all FM–layers. The images have a size of 1.5 μm × 1.5 μm.

Figure 5.5.24 shows the result of the calculations. In panel (a) the measured MFM image is shown. Again, the magnetization pattern of the sample is estimated. The up–direction was distinguished from the down–direction by choosing an appropriate discrimination level for the frequency shift image. The magnetization pattern is depicted in panel (b). When calculating the MFM–contrast arising from a domain structure in the FM–layers, the effect of the AF–layers on the MFM signal was neglected. In a second step, the sample stray field was calculated from the magnetization pattern. In order to calculate the stray field of one single domain pattern existing in all the FM–layers, the sample was considered as a collection of ten ferromagnetic thin films located at the tip–sample distances:

$$d_9 = d_{AF} + d_{ts} \quad \text{and} \quad d_{i-1} = d_i + d_{FM} + d_{AF}, \tag{5.5.2}$$

for $9 > i \geq 0$. Here $d_{AF} = 1\,\text{nm}$ denotes the thickness of an AF–layer, $d_{ts} = 30.4\,\text{nm}$ is the separation between the tip and the sample surface (the top–most AF–layer) in the measurement, and $d_F = 5\,\text{nm}$ is the thickness of a FM–layer. With this information, the MFM image shown in figure 5.5.24, panel (a) can be modeled. The spatial Fourier components of the total field become:

$$H_z^{tot}(\mathbf{k}) = \frac{M_{FM}}{2} \cdot \left(1 - e^{-kd_{FM}}\right) \cdot \sum_{i=1}^{10} e^{-kd_i} , \tag{5.5.3}$$

where $M_{FM} = 550\,\mathrm{kA/m}$ is the saturation magnetization of the FM–layers, and d_i is the distance between the tip and the i–th FM–layer of the sample as defined by equation 5.5.2. In a final step, the MFM image was calculated. This was carried out by multiplying the stray field with the tip transfer function and the instrument calibration function.

The modelled and measured domain patterns show the same structures and the grey scale distribution matches extremely well. Moreover, comparing the line sections taken from panel (a) and (c) along the green lines, a very good agreement in the peaks of the frequency shift can be found. A close inspection however, reveals that the measured contrast is always slightly smaller than the simulated one. This might be due to the additional contribution from the uncompensated interfacial AF–spins which produce a stray field opposing the stray field arising from the FM–layers. This was neglected in the simulation.

5.5.6   Quantitative analysis of the AF–contrast

When a sufficiently strong magnetic field is applied, the FM–layers become saturated. Since a homogeneously magnetized thin film does not generate a field, the magnetic stray field of the features seen in the MFM measurements above 800 mT must originate from uncompensated spins pinned at the AF–FM interfaces. They do not saturate in a 7.0 T field. In order to calculate the magnetic charge density at these interfaces a quantitative evaluation of the MFM–contrast, similar to that described above for the FM–layers was applied to the AF–layers. Again, a magnetization pattern (figure 5.5.25, panel (b)) was derived from the measured MFM data (figure 5.5.25, panel (a)). In contrast to the simulations performed for the FM–layers, the magnetic charge density at the AF–FM interfaces depends on the density of uncompensated spins. Therefore, the density of uncompensated spins was iteratively adjusted in the model to obtain the best agreement between the measured (figure 5.5.25, panel (a)) and the modelled (figure 5.5.25, panel (c)) images. The best agreement is obtained for a surface charge density of $\sigma_{CoO} = 118.4\,\mathrm{kAm}$.

Fig. 5.5.25: Panel (a) shows an MFM image and cross section at $800\,\mathrm{mT}$. Panel (b) depicts the magnetization pattern and cross–section generated from the MFM image. The modelled and measured grey scale images in panels (a) and (c) agree extremely well, when a surface charge density of $118.4\,\mathrm{kAm}^2$ is used. This reflects the reduced density of uncompensated spins at the AF–FM interfaces. The images have a size of 1.5 μm $\times$ 1.5 μm.

In order to determine the fraction of uncompensated spins at the FM–AF interfaces, the surface charge density found in the MFM image simulation was compared to the surface charge

density of a full monolayer of uncompensated spins. CoO is an atomically layered antiferromagnet with alternating sheets of oxygen and cobalt ions along the [111] direction as described in figure 5.2.2, panel (a). The Co^{2+} ions carry a magnetic moment of $+3.8\,\mu_B$ [126, 127]. Assuming a monolayer of uncompensated spins contributing at each interface, an expected surface charge density of 1813.2 kAm^2 is calculated. For bulk CoO, inside a [111] Co^{2+} ion layer the magnetic moments are ferromagnetically coupled and aligned with the [117] direction. Therefore the magnetic moment directed perpendicular to the interfaces will be reduced by the cosine of the angle between the [111] and [117] directions. In neglecting this angle of $\cos(43.3^o)$, an error of 28% is introduced into the calculation. However for very thin AF–layers as used in this sample (1 nm of CoO comprises only about three to four spin layers), the tilt angle might be smaller [111]. For an easy comparison with previous work, it was omitted here. From the charge density found in the simulations 0.07 monolayers of uncompensated spins at each interface are estimated. The results compare well with the estimates of 0.04 monolayers for the Co/NiO system in [109] and the 0.01 monolayers for CoO/MgO multi-layers [92] from XMCD measurements.

There have been numerous approaches to explain why only a small minority of interfacial spins are uncompensated. Malozemov *et al.* [97, 98] explained this fact by random local fields which cause the overall interfacial moment to diminish. The local fields emerge from structural defects and the mismatch of spin lattices in neighboring grains. Nowak *et al.* [129] and Rezende *et al.* [95] suggested the existence of an extended interface region, in which by interdiffusion of elements from the AF– and FM–layers, a disordered layer forms. This layer gives rise to an almost random orientation of the spins or only a very locally ordered spin structure.

In the present sample, the Co and CoO are both grown in [111]–direction with a small mocaicity. The magnetic multi-layer system only consists of two elements and the lattice mismatch is expected to be small due to the growth method of the CoO. This means, that Malozemovs', Nowaks' and Rezendes' assumptions are not fulfilled in the present case. However, Takano *et al.* [92], have put forward another model which only deploys the idea that, due to roughness of the grain surface and/or tilt of the spin lattices towards the sample normal, both AF spin sublattices are present at the interface. Using this model and the fact that the AF–layers were preset by the bias field of the FM–layers during cooling, the grainy AF–contrast can be explained.
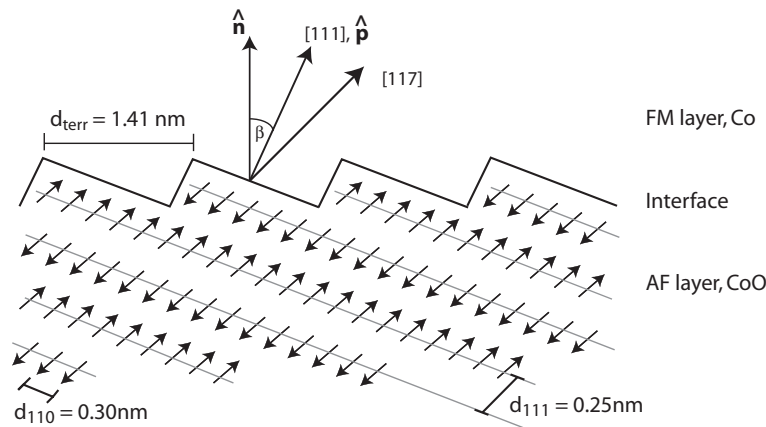
Fig. 5.5.26: Schematic drawing of AF spin layers at the interface. If the spin sheet axes p is 10° off the nomal n of the interface, the spin sublattices form terraces with a width of 1.54 nm. The distance between the spin sheets in [111]–direction measures 0.27 nm, the distance between spins in one sheet is 0.65 nm.

Due to the mocaicity of the [111]–directions of the grains to the interface normal in the AF–layer, the two spin sub–lattices will form monospin terraces at the interface as depicted in figure 5.5.26. In the oxidation process of Co, CoO is formed as oxygen atoms move to the interstitial sites of the Co lattice, so that Co and thin CoO films have the same structure. For the analysis, the bulk NaCl (double fcc) lattice structure of CoO is assumed [126, 128, 130]. The lattice constant of CoO is 0.425 nm [131], therefore the spins within one ferromagnetic sheet are distanced by 0.30 nm and the antiferromagnetically coupled sheets are spaced by 0.25 nm[13]. If one assumes an off-angle of 10° or smaller from the [111] direction, the terraces will have a minimum size of 1.41 nm (about 4-5 spins). From the topography image in figure 5.4.12 grain sizes of 15 nm to 50 nm can be found, resulting in 7 to 23 terraces respectively. If the size is equal for all terraces and if they are occupied alternatingly by the two different spin sublattices, no net excess of spins of one type (either up or down) results (no uncompensated spins). However, the roughness of the grain surfaces will generate a distribution of terraces sizes being able to create a net excess of one spin type.

In addition, the bias field from the FM–layer when cooling the AF–layer though the Néel temperature can generate such an excess. Figure 5.5.27 illustrates this model:
Panel (a) shows a combined AF–FM layer system above the Néel temperature. In this configuration, the spins in the AF are not ordered. Panels (b) and (c) show an AF–FM layer system below the ordering temperature of the AF. It is assumed that the coupling across the grain bounderies is negligible compared to the AF–FM coupling. In the case represented by panel (b), the AF–layer was cooled down through T_N, biased by the field of an adjacent FM–layer with a random domain structure. One of the domain boundaries in the FM–layer formed on top of the grain boundary in the AF–layer. Biased by the up domain in the FM–layer, the right grain is terminated by a terrace of down–spins, assuming an antiferromagnetic coupling of the two layers across their common interface. Likewise, the left grain is terminated by a terrace of up–spins. Averaging the number of interfacial spins per grain, the right grain shows an excess of down–spins whereas, the left grain possesses more interfacial up–spins. The local uncompensated spins generate a stray field outside the sample, which can be sensed by an MFM tip. Assuming, the magnetization direction of the MFM tip points towards the sample, in an external magnetic field, large enough to saturate the FM layer, the right grain would be imaged with a dark contrast, the left grain with a light contrast.

Finally, panel (c) shows several grains within one domain. This case equals the situation, in which the whole sample was cooled down in a uniform magnetic field. At a temperature lower than T_N, the AF grains arrange so that the majority (or the first interfacial layer, depending on the definition of the interface) of interfacial spins couples antiferromagnetically to the FM layer. It is assumed that the coupling across the grain bounderies is negligible compared to the AF–FM coupling. In the presented configuration, the grain on the left hand side shows the highest amount of uncompensated spins, followed by the grain on the left hand side and finally the grain in the middle. Consequently, in a large enough external magnetic field, the MFM tip described before will image the grain on the right with a bright contrast, the grain on the left in a dark contrast and the middle grain in an intermediate contrast.

Based on this model, the grainy contrast occurring on a 50 nm to 80 nm scale in the images of panels (e) an (f) of figure 5.5.19 and panel (f) of figure 5.5.20 can be explained. Its origin lies in the averaging of the MFM measurement over several grains due to the data point resolution of 19.5 nm. This leads to a certain local MFM–contrast on the length scale observed in the images. However, this also implies that the amount of uncompensated spins and therefore

---

[13]However a 1 nm thick CoO layer will certainly be distorted to some extent from the undisturbed bulk structure. This is neglected here.
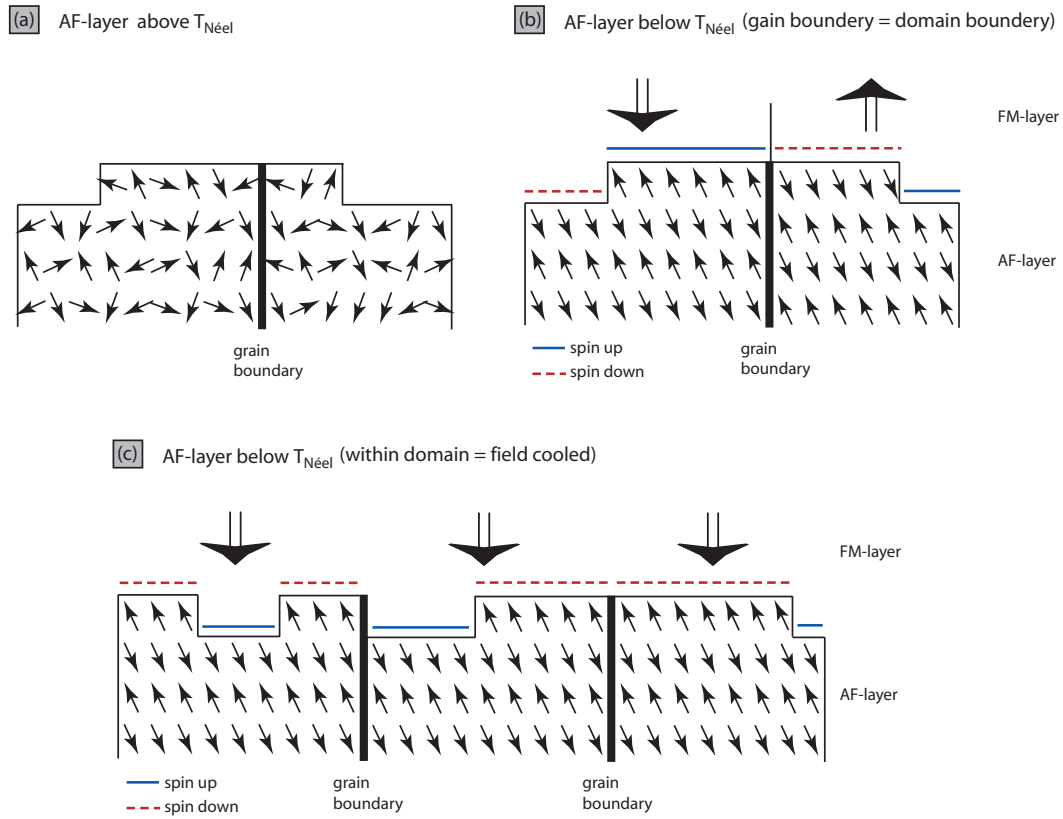
Fig. 5.5.27: Illustration of the formation of uncompensated spins. Panel (a) shows two grains of a AF–layer above the Néel temperature, their spins being completely at random direction. Cooled down through T_N the spins will align depending on the bias field they experience. In panel (b), a domain boundery coincides with the grain boundery, leaving the right grain with an excess of dwn–spins and the left grain with an excess of up–spins. Panel (c) shown several grains within a single domain. Due to the different interfacial geometry, the grains have a different amount of uncompensated spins exhibiting a different MFM contrast.

the MFM–contrast might be much larger on a single grain scale.

In figure 5.5.27, panel (b), several spins in the left and right grain could not form an anti-ferromagnetic coupling across the AF–FM interface. These spins are called *frustrated spins* because their total energy is higher than of the surrounding spins, increased by the ferro-magnetic alignment with the spins from the FM–layer. Note, that this energy increase is independent of the strength of the bias field or the external field.

5.5.7 Origin of the contrast decrease in high external fields

In fields larger than 800 mT, the FM–layers are saturated in field direction. In the sketch of figure 5.5.28, panel (a), the external field is directed downwards. The two blue arrows indicate a pair of spins from the two spin sublattices. The total energy of these two spins in the AF–layer is given by the sum of the Zeemann energy, the anisotropy energy and the exchange energy of the two spins:

$$E_{tot} = -|\mathbf{H}_{ex}| \cdot |\mathbf{s}|(\cos\theta_\uparrow + \cos\theta_\downarrow) + K_{AF}(\sin^2\theta_\uparrow + \sin^2\theta_\downarrow) + A_{AF}\cos(\theta_\uparrow - \theta_\downarrow), \quad (5.5.4)$$

with H_{ex} being the external field and s the spin moment. K_{AF} and A_{AF} are the anisotropy constant and the exchange stiffness. $\theta_\uparrow$ and $\theta_\downarrow$ denote the angle between the up–spin and the

field direction and the down–spin and the field, respectively. The up-spins stand against the field direction, resulting in an increased Zeemann energy. In order to lower this energy they can cant in the external field as indicated. Below the sketch the Zeemann energy of the spins is drawn in units of $|\mathbf{H}_{ex}| \cdot |\mathbf{s}|$ for a fixed H_{ex} as a function of the canting angles $\theta_\uparrow$ and $\theta_\downarrow$. It is apparent that the up–spin (indicated by the red cross at an angle of 136.7^o) can strongly decrease its energy by canting slightly into the field direction (following the blue arrow in the sketch). The down–spin can also lower its dipolar energy by canting further into the field direction. In a bulk CoO, this would lead to the formation of a (partial) domain wall in the AF–layer parallel to the interface as suggested by Mauri [91]. In order for such a domain wall to form, the AF–FM interface exchange coupling J_{ex} needs to be larger than the anisotropy constant times the exchange stiffness of the spins ($J_{ex} \gg \sqrt{K_{AF}A_{AF}}$)[14]. Indeed this model is favoured by most authors who investigated CoO/Co bilayers [132, 111, 124], only one group claims the domain wall exists in the FM–layer [125].

The anisotropy constant of bulk CoO is very large ($2.9 \cdot 10^9$ J/m^3 [134]), much larger than the interfacial exchange coupling to the FM–layer. Therefore a (partial) domain wall in the AF layer would be energetically very unfavourable. However, in the sample at hand, the AF–layers are very thin, therefore upon rotation of the FM–layer into field direction, strong destabilization forces are impinging on the AF–spins standing against the field direction. This could weaken the extremely thin layer, moving it towards a superparamagnetic behaviour and causing a "magnetically soft" AF state as suggested by Spagna *et al.* [133]. Recent works on oxide passivated fine Co particles [135, 136] support this explanation.
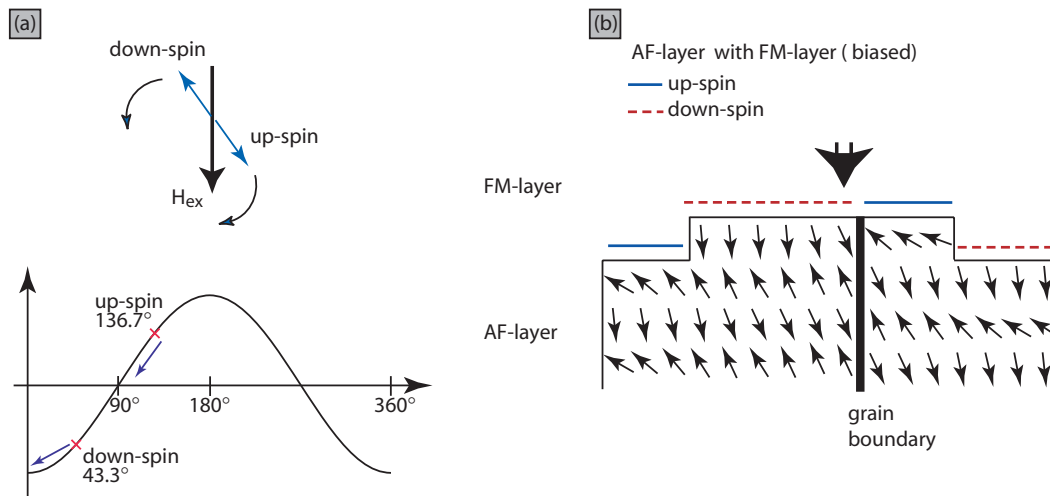
Fig. 5.5.28: In a large external field directed downwards, the up-spins will cant towards the field direction, lowering their Zeemann energy as shown in panel (a) in the upper sketch. In order to restore the original AF spin structure, spins in successive sheets have to cant as well, forming a spin wave in vertical direction (panel (b)). The spins directed towards the field direction will cant a bit more in this direction. To circumvent the built-up of an energetically unfavourable domain wall perpendicular to the interface, the spins within one spin sublattice form a spin wave in the plane parallel to the interface.

---

[14]Then the bias field $H_{ex} \sim \sqrt{A_{af}K_{AF}}$ is independent of J_{ex} and saturates already at energies far less than the fully uncompensated interfacial exchange coupling case of Meiklejohn and Bean [137]. They assumed that $J_{ex} \gg \sqrt{A_{AF}K_{AF}}$, therefore in their exchange field expression, H_{ex} is proportional to J_{ex}. It is interesting to note that in the case of both $\sqrt{A_{AF}K_{AF}}$ and J_{ex} being much larger than $\sqrt{A_{FM}K_{FM}}$, the domain wall will form in the FM–layer.

In the thin AF–layers of the present sample, it is unlikely, that a full domain wall will form. Instead, the spins within one spin sheet will wiggle slightly in order to allow the up-spins to cant into the field direction as shown in the illustration in figure 5.5.28, panel (b). This winds up a twist parallel to the interface. In order to restore the original AF spin structure, spins in successive sheets have to cant as well, forming a spin wave in vertical direction. This leads to a reduction of the generated magnetic surface charges at the interface and consequently to a smaller stray field and a weaker MFM contrast. Indeed, the reduction of the MFM signal can be observed in measurements of the AF-contrast. This was verified for images acquired

	Contrast range [Δf]	FWHM of Gaussian fit
0 mT	2.73 Hz	1.96 Hz
-65 mT	2.47 Hz	1.81 Hz
-800 mT	1.66 Hz	0.76 Hz
-2500mT	1.31 Hz	0.51 Hz
-4000mT	0.97 Hz	0.39 Hz
-7000mT	0.72 Hz	0.17 Hz

Table 5.5.3: Summary of the contrast reduction analysis for high external fields.

in various fields. They were compared by fitting a Gauss function to their frequency shift histograms as already performed in chapter 5.4.3. Table 5.5.7 shows the frequency shift range as well as the FWHM of the Gaussian fits. The reduction of the MFM contrast is clearly visible. It supports the model of the canted spin configuration in high external fields.

Conclusions and outlook

The data presented and discussed in this thesis clearly show that high resolution magnetic force microscopy, together with a quantitative analysis of the MFM measurements is a powerful and versatile tool for the investigation of magnetic samples. The possibility to calibrate the imaging properties of a cantilever paired, with model calculations and simulations of an MFM image, opens up a wide field for the investigation of sample magnetization structures. In a quantitative analysis, not only can the stray field of the magnetic surface layer be revealed, but it is also possible to identify magnetization structures deep inside a magnetic multi-layer. Moreover, the evolution of magnetic domains as a function of an applied external magnetic field can be studied.

In chapter 1, the contrast formation in an MFM image has been described by a transfer function theory. The theory in combination with experimental methods described by van Schendel [9], allows the calibration of the imaging properties of an MFM tip and therefore the quantitative interpretation of an MFM measurement. In addition, a new type of calibration sample based on a out-of-plane recording media was presented. Into this media, bits of various sizes were written. The sample shows a homogenous domain size distribution down to domains of 6 nm to 8 nm which facilitates the calibration of high resolution MFM tips.

All data presented in this work were acquired with either the low temperature ultra high vacuum SFM (LTSFM) or the newly built high resolution MFM (hr-MFM). The latter was constructed for applications in industrial research, implying a easy handling and non-destructive measurement of whole hard disk platters. The hr-MFM works at room temperature and shows a superior lateral resolution comparable to the resolution obtained with the LTSFM. Both instruments and schematic diagrams of their electronics have been described in chapter 2.

In chapter 3.1, two techniques to separate magnetic from non-magnetic tip-sample contributions of an MFM measurement were studied. The first technique relies on the fact that the MFM contrast will be inverse if the magnetization direction of the tip is rotated by 180° between two scan images. However, the topographic contrast originating from the van der Waals interaction between the tip and the sample, will not reverse. The technique reliably determines the topographic influence in the MFM image. It was qualitatively compared to a topography scan performed in constant frequency shift mode. However, the difficulties of the experimental procedure, namely the removal of the sample from the microscope when remagnetizing the tip, and the accuracy with which the lateral and vertical tip–sample positions have to be recovered, made it necessary to develop a different approach. The second technique for the separation of topography and magnetism relies on the fact that the topography induced contribution to the measured MFM image can be calculated from a topography image, if the geometry of the tip and the vertical distance between the topography measurement and MFM measurement are known. The pure magnetic contribution in the MFM image can thus be calculated by subtracting the topography influence from the MFM raw data. The technique produces results of similar quality compared to the first technique. The difficulty of the

second technique lies in the reliable determination of the tip geometry which is important for the calculation of the topographic influence. In addition, it was found that it is vital for both techniques that the tip geometry does not change in between the scans. A hard tip sample contact, for example, can blunter the tip, making it less sensitive to magnetic forces and more sensitive to van der Waals forces. In the future, it may be interesting to study if the magnetic and non-magnetic contributions in an MFM image could be written as a convolution, much in the same way as the magnetic contrast can be written as a convolution between the stray field of the sample and the magnetization of the tip. This would enable the separation of the magnetic contributions from the topographic influence in an MFM measurement using only a single MFM image.

The applicability of cantilever tips with various geometry and magnetic coating for high resolution MFM was studied in chapter 3.2. Three types of cantilevers were tested, namely, Nanosensor PP, Team Nanotec SC and ISC and tips grown by electron beam deposition from Utke *et al.* The sensitivity spectra and stray fields of the tips were compared. It was shown that the ISC and SC tips coated with a thin ferromagnetic layer from only one side of the taper of the tip are most suited for high resolution MFM. Their sensitivity spectra fall off most gently with decreasing magnetic wavelength which enables the measurement of small magnetic structures of the sample with a high signal to noise. In addition, their stray fields are very weak, less than 8 mT, which prevents mutual modifications of a hard magnetic sample. The tips from Utke *et al.* are also suited for high resolution MFM, however, their stray fields are almost a factor of 4 larger than that of the ISC tips. This may lead to non-negligible modifications of the sample magnetization structure. In future work, it would be interesting to compare the MFM tips prepared in our lab to commercially available MFM cantilevers. In addition, new ferromagnetic coatings could be studied.

In order to maintain a very high imaging quality in MFM, the degradation of the imaging properties of a cantilever tip during an experiment has to be kept to a minimum. In chapter 3.3, the decrease in imaging sensitivity and in lateral magnetic resolution under typical MFM operations as well as operational errors was studied. ISC and SC cantilevers from Team Nanotec and Nanoworld PP tips were tested. It was shown that the very fragile ultrasharp tips from Team Nanotec should only be used in a true non-contact operation mode. In addition, when scanning in constant height, the dissipation of the cantilever oscillation has to be monitored. Whenever the dissipation exceeds 1.5x the excitation needed to maintain a constant amplitude for the free oscillating cantilever (dissipation limit), the tip has to be retracted to a safe distance from the sample. Only doubling the value for the dissipation limit degrades the maximum lateral resolution of the tips by almost 3 nm. The tip and its magnetic coating have been damaged, namely the apex has become blunter, so it is less sensitive to short spatial magnetic wavelengths. In addition, the enlarged apex increases the van der Waals interaction between tip and sample; therefore, topography artifacts become more pronounced. The SC and ISC tips are also not suitable for intermittent contact operation modes. The maximum lateral resolution of the ISC tip, for example, decreased from initially 11.2 nm to 21.3 nm after only one image of tapping mode. The reduction in stray field of the tip to one third of the initial stray field value shows that a part of the apex of the tip or even of the taper has broken off. The imaging properties of the Nanoworld cantilever are less prone to degradation in the tests which can be explained by the geometry of the taper; a pyramid of micrometer size dimensions. However, the imaging properties are not suitable for high resolution magnetic measurements.

In chapter 4, hard disk media, written tracks and bits were investigated with MFM. The high resolution MFM images offer a wide variety of analysis methods. Qualitatively, the form

of the transitions or defects in the media and in the development of the write head field can be extracted. In addition, the images can reveal a possible cause for abnormal values of a measured spin stand property. These properties are the most important data on which the performance of hard disk media and write heads is evaluated. Therefore, quantitative evaluation procedures were established to extract parameters such as the transition position jitter and transition jitter from an MFM measurement. This was performed by first extracting each individual bit transition from the analyzed MFM images. It is a clear advantage over the spin stand data analysis in which only the statistical average of the bit transition position can be extracted. For the investigated media, the transition jitter was about 13 nm for both track densities analyzed. This clearly shows a magnetic clustering of the grains, which have a size of only about 10 nm, in the vicinity of the bit transition. In future work, more procedures to extract media and write head properties from the MFM images, such as determination of DC and AC noise and percolation analysis, should be implemented.

In chapter 5, the exchange bias and its origin in a sample of alternating ferromagnetic (Co/Pt) and antiferromagnetic (AF) layers (CoO) were investigated. In a first experiment, the sample was cooled down to a temperature well below the Néel temperature of CoO in an external field, well above the saturation field of the ferromagnetic (FM) layers. The domain formation in subsequently measured MFM images along a hysteresis loop shows the formation of two-dimensional and line-like reverse domains in eight of the ten FM layers in the sample. Only in higher external fields, when the eight FM-layers have already completely reversed into field direction, the other two layers start to nucleate domains. It was shown by a quantitative analysis of the MFM contrast that these two layers are the lowest two in the sample. Furthermore, it was found that the reason for their separate nucleation in high fields on both sides of the hysteresis loop can only be explained by a larger average anisotropy value in the two layers. This may be connected to more uniform growth conditions for the lowest two layers in the sample. The very weak and grainy contrast observed in images taken in either fields lower than the nucleation field or higher than the saturation field of all FM layers, was compared to the underlying topography of the sample. It could be shown that the length scale of the grainy MFM contrast was about a factor of two larger than the average grain size. This indicates that the contrast is due to the uncompensated spins at the interfaces of the AF-FM layers. The MFM contrast in a field slightly higher than the nucleation field was quantitatively analyzed as well. The magnetization distribution of all eight FM-layers was extracted from the MFM data. A simulation of an MFM image showed an excellent agreement with the MFM measurement. Small deviations of the MFM contrast could be eliminated by a redistribution of domains in a smaller or larger number of FM layers. This clearly shows that with quantitative MFM it is possible to identify magnetization structures even if they are located deep inside a magnetic multi-layer.
The exchange bias shift of the measured hystersis loop was calculated to be 112 mT. This is in very good agreement with SQUID hysteresis loop measurements carried out at a temperature of 10 K.
In the second experiment discussed in chapter 5, the magnetic multi-layer was cooled down in zero external field, but with a well prepared stripe domain state in the FM layer. This domain structure was copied into the AF layers upon cooling through the Néel temperature. In subsequently measured MFM images along the hysteresis loop, the domains in the FM layers reversed into field direction. However, a grainy and very weak magnetic contrast (AF-contrast) remained even in fields of 7 T. This contrast can be attributed to the uncompensated spins at the AF-FM interfaces. It was found that the weak AF-contrast is colinear but inversed with respect to the contrast arising from domain structures in the FM-layers (FM-contrast). The colinear alignment of the domains agrees with work by Nolting *et*

al. [138] and is consistent with the model in [111] where the spins were assumed to align along the crystalline axis closest to the field cooling direction. The alignment can be explained by an antiferromagnetic coupling of the AF- and FM-layer across their common interface. The coupling is mediated by a superexchange interaction via the oxygen atoms of the CoO layers. However, the results stand in contrast to a mean-field analysis by Parker *et al.* [139] which concluded direct exchange for the operating mechanism and Ohldag *et al.* [109] who found, that for NiO, the uncompensated spins were parallel to the ferromagnet.

The contrast inversion of images of the FM- and AF-contrast taken on opposite branches of the hysteresis loop could be explained by a reorientation of the tip magnetization into the new field direction in a very weak external field of 65 mT. A quantitative comparison of the measured FM-contrast with a simulated FM-contrast revealed a very good agreement if all the ten FM-layers in the multi-layer sample were used for the modeling. This is in contrast to the observation made in the saturation field cooled case, in which only the highest eight FM-layers of the sample contributed to the MFM contrast in low external fields.

Considering the procedure by which the FM-contrast of the zero field cooled case was simulated, the percentage of uncompensated spins at the AF-FM interfaces was extracted from MFM measurements. It was found that only 7% of the interfacial Co spins are effectively uncompensated. This is in good agreement with the value of 0.04 monolayers found by XMCD methods in Co/NiO systems [109] and the 0.01 monolayers for CoO/MgO multilayers [92].

The further slow decrease in the AF-contrast in fields above the saturation field of the FM-layers can be explained by a small rotation of spins out of the anti-parallel alignment towards the field direction, thus lowering their Zeemann energy. This leads to a reduction of the generated magnetic surface charges at the interface and consequently to a smaller stray field and thus a weaker MFM contrast.

As a suggestion for future work, it would be interesting to map the distribution of uncompensated spins on an inter-grain or even intra-grain length scale with high resolution MFM. A comparison to the underlying topography of the grains could lead to a better understanding of the micromagnetic origin of the exchange bias shift. In addition, the spin-rotation model for the interfacial AF-layer spins in high external fields could be verified. Furthermore, investigations of the uncompensated spin density in multi-layer systems which can more easily be accessed by XMCD methods would enable direct comparison of the results and a verification of the MFM based determination of the number of uncompensated spins.

List of Figures

List of Tables

Bibliography

[1] F. Bitter: *On the inhomogeneities in the magnetization of ferromagnetic materials*, Phys. Rev. **38**, p1903 (1931)

[2] L. v. Hámod, P. A. Thiessen: *Über die Sichtbarmachung von Bezirken verschiedenen ferromagnetischen Zustandes fester Körper*, Z. f. Phys. **71**, p442 (1931).

[3] P. Weiss: *L'hypthese du champs mol eculaire et la propri et e ferromagn etique*, J. de Phys. **6**, p661 (1907).

[4] J. J. Saenz, N. Garcia, P. Grütter, E. Meyer, H. Heinzelmann, R. Wiesendanger, L. Rosenthaler, H. R. Hidber, H.-J. Güntherodt: *Magnetic domain structure by measuring magnetic forces*, J. Appl. Phys. **62**, p4293 (1987)

[5] Y. MArtin, C. C. Williams, H. K. Wickramasinghe: *Atomic force microscope – force mapping and profiling on a sub-100Å scale*, J. Appl. Phys. **61**, p4723 (1987)

[6] D. Rugar, H. J. Mamin, P. Guenther, S. E. Lambert, J. E. Sern, I. McFayden, T. Yogi: *Magnetic force microscopy: General principles and application to longitudinal recording media*, J. Appl. Phys. **68**, p1169 (1990)

[7] H. J. Hug, B. Stiefel, P. J. A van Schendel, A. Moser, S. Martin, H.-J. Güntherodt: *A low temperature ultrahigh vacuum scanning force microscope*, Rev. Sci. Instrum. **70**, p3625 (1999).

[8] S. Foss, C. Merton, R. Proksch, G. Skidmore, J. Schmidt, E.D. Dahlberg, T. Pokhil, Y.T. Cheng: *Variable magnetic field magnetic force microscopy of the magnetization reversal in epitaxial iron (111) thin films*, J. Magn. Magn. Mat. **190**, p60 (1998)

[9] P. J. A. van Schendel: *Investigation of magnetization structures in ferromagnetic and superconducting samples by magnetic force microscopy*, Ph.D. thesis, University of Basel 1999

[10] P. Fischer, D. Denbeaux, H. Stoll, A. Puzic, J. Raabe, F. Nolting, T. Eimuller, G. Schutz: *Multilayered magnetic nanostrips studied by transmission x-ray microscopy*, J. de Phys **IV** Proc., p471 (2003)

[11] S. Anders, H. A. Padmore, R . M. Duarte, T. Renner, T. Stammler, A. Scholl, M. R. Scheinfein, J. Stöhr, L. SŐve, B. Sinkovic: *Photoemission electron microscope for the study of magnetic materials*, Rev. Sci. Instr. **70**, p3973 (1999)

[12] R. Allenspach: *Spin-polarized scanning electron microscopy*, IBM J. Res. Dev. **44**, p553 (2000)

[13] M. R. Scheinfein, J. Unguris, M. Kelley, D. T. Pierce, R. J. Celotta: *Scanning electron microscopy with polarization analysis (SEMPA*, Rev. Sci. Instr. **61**, p2501 (1998)

[14] P. J. A. van Schendel, H. J. Hug, S. Martin, H. J. Güntherodt: *A method for the calibration of magnetic force microscopy tips*, J. Appl. Phys. **88**, p435 (2000)

[15] P. Grunberg, J. Barnas, F. Saurenbach,J. A. Fuss, A. Wolf, M. Vohl: *Layered magnetic structures: antiferromagnetic type interlayer coupling and magnetoresistance due to antiparallel alignment*, J. Magn. Magn. Mat. 93, p58 (1991)

[16] A. Barthelemy, M. N. Baibich, J. M. Broto, R. Cabanel,G. Creuzet,P. Etienne,A. Fert, A. Friederich, S. Lequien, F. Nguyen-Van-Dau, K. Ounadjela:*Giant magnetoresistance of (001)Fe/(001)Cr superlattices*, Charact. Prop. Ultrathin Magn. Films Multilayers, Mater. Res. Soc, Pittsburgh, p43 (1989)

[17] R. Hoffmann: *Magnetic and interatomic forces measured by low temperature scanning force microscopy*, Ph.D. thesis, University of Basel (2001)

[18] J. D. Jackson: *Classical electrodynamics*, 2nd ed., John Wiley and Sons, London (1975)

[19] E. Meyer, H- J. Hug, R. Bennewitz: *Scanning Probe Microscopy*, 1st ed, Springer, Berlin (2003)

[20] F.-J. Giessibl: *Forces and frequency shifts in atomic-resolution dynamic-force microscopy*, Phys. Rev. B **56**, p16010 (1997)

[21] U. Dürig: *Relations between interaction force and frequency shift in large-amplitude dynamic force microscopy*, Appl. Phys. Lett. **75**, p433 (1999)

[22] M. Abramowitz and I. A. Stegun: *Handbook of mathematical functions*, US Government Printing Office, Washington (D.C.) (1965)

[23] T. Albrecht, P. Grütter, D. Rugar, D. P. E. Smith: *Low-temperature force microscope with an all-fiber interferometer*, Ultramic. |ëextbf42, p1638 (1991)

[24] R. Madabhushi, R.D. Gomez, E. R. Burke, I.D. Mayergoyz: *Magnetic biasing and MFM image reconstruction*, IEEE Trans. Magn. **32**, p4147 (1996)

[25] T. Chang, M. Lagerquist, J.-G. Zhu, J.H. Judy, P. B. Fischer, S.Y. Chou: *Deconvolution of magnetic force images by Fourier analysis*, IEEE Trans. Magn. **28**, p3138 (1992)

[26] J.-G. Zhu, X. Lin, R.C. Shi, Y. Luo: *Magnetic force microscopy image restoration technique for removing tip dependence*, J. Appl. Phys. **83**, p6223 (1998)

[27] J. Lohau, S. Kirsch, A. Karl, G. Dumpich, E.F. Wassermann: *Quantitative determination of effective dipole and monopole moments of magnetic force microscopy tips*, J. Appl. Phys.**86**, p3410 (1999)

[28] D.E. Gray (editor): *American Institute of Physics Handbook*, 3rd ed, McGraw-Hill Book Company, New York (1972).

[29] G. Bochi, C. Ballentine, H. E. Inglefield, C. V. Thompson, R. C. O'Handley, H. J. Hug, B. Stiefel, A. Moser: *Perpendicular magnetic anisotropy, domains, and misfit strain in epitaxial $NiCu_{1-x}/Ni_x/Cu/Si$ (001) thin films*, Phys. Rev. B **52**, p7311 (1995).

[30] G. Bochi, H. J. Hug, D. I. Paul, B. Stiefel, A. Moser, I. Parashikov, H.-J. Güntherodt, R. C. O'Handley: *Magnetic domain structure in ultrathin films*, Phys. Rev. Lett. **75**, p1839 (1995).

[31] L. Abelmann, S. Porthun, M. Haast, C. Lodder, A. Moser, M. E. Best, P. J. A van Schendel, B. Stiefel, H. J. Hug, G. P. Heydon, A. Farley, S. R. Hoon, T. Pfaffelhuber, R. Proksch, K. Babcock: *Comparing the resolution of magnetic force microscopes using the CAMST reference samples*, J. Magn. Magn. Mater. **190**, p135 (1998).

[32] B. Stiefel: *Magnetic force microscopy at low temperatures and in ultra high vacuum*, Ph.D. thesis, University of Basel (1998)

[33] R. Garcia, R. Perez: *Dynamic atomic force microscopy methods* Surf. Sci. Rep. **47**, p197 (2002)

[34] U. Rabe, K. Janser, W. Arnold: *Vibrations of free and surface-coupled atomic force microscope cantilevers: theory and experiment* Rev. Sci. Instrum. 67, p3281 (1996).

[35] T. R. Albrecht, P. Grütter, D. Horne, D. Rugar: *Frequency modulation detection using high-Q cantilevers for enhanced force microscope sensitivity*, J. Appl. Phys. **69**, p668 (1991).

[36] H.J. Hug, private communications

[37] C. Loppacher: *Nichtkontakt-Rasterkraftmikroskopie mit digitalem Phasenregelkreis*, Ph.D. thesis, University of Basel (2000).

[38] C. Loppacher, M. Bammerlin, F. Battiston, M. Guggisberg, D. Müller, H. R. Hidber, R. Luethi, E. Meyer, H.-J. Güntherodt: *Fast digital electronics for application in dynamic force microscopy using high-Q cantilevers*, Appl. Phys. A **66**, pS215 (1998).

[39] A. Moser: *Untersuchungen von Hochtemperatursupraleitern mit dem Rasterkraft-mikroskop* Ph.D. thesis, University of Basel (1995).

[40] Website: www.swissprobe.com

[41] Website: www.nanonis.com

[42] H. A. M. van den Berg: *Order in the domain structure in soft-magnetic thin-film elements: A review*, IBM J. Res. Dev. **33**, p540 (1989)

[43] M. L. De Graef: *Recent advances in quantitative Lorentz microscopy*, Digest of technical Papers, Intermag 2002 Cat.No.02CH37323. (2002)

[44] J. Israelachvili: *Intermolucular and Surface forces*, 2nd ed., Academic Press, London (1992)

[45] C. Schönenberger, S.F. Alvarado, S.E. Lambert, I.L. Sanders: *Separation of magnetic and topographic effects in force microscopy*, J. Appl. Phys. **67**, p7278 (1990)

[46] M. Saint Jean, S. Hudlet, C. Guthmann, J. Berger: *Van der Waals and capacitive forces in atomic force microscopies*, J. Appl. Phys. **86**, p4245 (1999)

[47] S. Belaidi, P. Girard, G. Leveque: *Electrostatic forces acting on the tip in atomic force microscopy: Modelization and comparison with analytic*, J. Appl. Phys. **81**, p1023 (1997)

[48] H. Hölscher, U.D. Schwarz, R. Wiesendanger: *Calculation of the frequency shift in dynamic force microscopy*, Appl. Surf. Sci. **140**, p344 (1999)

[49] F.J. Giessibl, H. Bielefeldt: *Physical interpretation of frequency-modulation atomic force microscopy*, Phys. Rev. B **61**, p9968 (2000)

[50] M. A. Lantz, H. J. Hug, R. Hoffmann, P. J. A. van Schendel, S. Martin, A. Baratoff, A. Abdurixit, H.-J. Güntherodt, Ch. Gerber: *Low temperature scanning force microscopy of the Si(111)-(7x7) surface*, Phys. Rev. Lett. **84**, p2642 (2000)

[51] M. A. Lantz, H. J. Hug, R. Hoffmann, P. J. A. van Schendel, P. Kappenberger, S. Martin, A. Baratoff, H.-J. Güntherodt, Science **291**, p2580 (2001)

[52] N. Sasaki, M. Tsukada: *Theoretical evaluation of the frequency shift and dissipated power in noncontact atomic force microscopy*, Appl. Phys. A **72**, S39 (2001)

[53] A. Baratoff, private communications

[54] J. Schelten, P. Bauer, H. Bochem, WO9637, p788 (1996)

[55] T. Arie, H. Nishijima, S. Akita, Y. Nakayama: *Carbon-nanotube probe equipped magnetic force microscope*, J. Vac Sci. Technol. B **18**, p104 (2000)

[56] L. Folks, M. E. Best, P. M. Rice, B. D. Terris, D. Weller, J. N. Chapman: *Perforated tips for high-resolution in-plane magnetic force microscopy*, Appl. Phys. Lett. **76**, p909 (2000)

[57] Z. Liu, Y. Dan, Q. Jinjun, Y. Wub: *Magnetic force microscopy using focused ion beam sharpened tip with deposited antiferroÐferromagnetic multiple layers*, J. Appl. Phys. **91**, p8843 (2002)

[58] Y. Wua, Y. Shen, Z. Liu, K .Li, J. Qiu: *Point-dipole response from a magnetic force microscopy tip with a synthetic antiferromagnetic coating*, Appl. Phys. Lett. **82**, p1748 (2003)

[59] Website: www.nanoworld.com

[60] Website: www.team-nanotec.de

[61] Y. Akama, E. Nishijiama, S. Akita, Y. Nakayama: *New scanning tunneling microscopy tip for measuring surface top*, J. Vac Sci. Technol. A **8**, p429 (1990)

[62] I. Utke, P. Hoffmann, R. Berger, L. Scandella: *High-resolution magnetic Co supertips grown by a focused electron beam*, Appl. Phys. Lett **80**, p4792 (2002).

[63] V. Poulsen, US Patent: 661-619-1900 (1898)

[64] F. Jorgensen: *The inventor Valdemar Poulsen*, J. Magn. Magn. Mat. **193**, p1 (1999)

[65] L. Mayer, General Mills Newsletter, Minneapolis, Minnesota (1958)

[66] D. L. A. Tjaden, L. Leyten: *A 5000:1 scale model for the magnetic recording process*, Philips Res. Reports **25**, p319 (1964)

[67] S. Iwasaki, T. Suzuki: *Dynamical interpretation of magnetic recording process*, IEEE Trans. Magn. **MAG-4** (1968)

[68] D. Weller, private communications

[69] D. Kean: *International Business Corporation*, IBM San Jose, p23, (1977).

[70] A. S. Hoagland: *History of magnetic disk storage based on perpendicular magnetic recording*, IEEE Trans. Magn. **39**, p1871 (2003)

[71] E. .E. Fullerton, D. T. Margulies, M. E. Schabes, M. Carey, B. Gurney, A. Moser, M. Best, G. Zeltzer, K. Rubin, H. Rosen: *Antiferromagnetically coupled magnetic media layers for thermally stable high-density recording*, Appl. Phys. Lett. **77**, p3806 (2000)

[72] E. N. Abarra, A. Inamota, H. Sato, I. Okamoto, Y. Mizoshita: *Longitudinal magnetic recording media with thermal stabilization layers*, Appl. Phys. Lett. **77**, p2581 (2000)

[73] S.H. Charap, P.L. Lu: *Thermal stability of recorded information at high densities*, Y.He, IEEE Trans. Magn. **33**, p978 (1997)

[74] D. Weller, A. Moser: *Thermal effect limits in ultrahigh-density magnetic recording*, IEEE Trans. Magn. **35**, p4423 (1999)

[75] S.H. Charap, P.L. Lu: *Thermal stability of recorded information at high densities*, Y.He, IEEE Trans. Magn. **33**, p978 (1997)

[76] H.N.Bertram: *Theory of magnetic recording*, Cambridge University Press 1994

[77] S. S. Malhotra, B. B. Lal, M. Alex, M. A. Russak: *Effect of track edge erasure and on-track percolation on media noise at high recording density in longitudinal thin film media*, IEEE Trans. Magn. **33**, p2992 (1997)

[78] A. Moser, K. A. Rubin, M. E. Best: *Transition position jitter in longitudinal magnetic recording media*, IEEE Trans. Magn. **37**, p1872 (2001)

[79] A. Moser, private communications

[80] T. Min, L. Nix, D. Cahalan, K. Chopra: *Track position dependence of performance attributes in permanent magnet biased MR/SAL heads*, IEEE Trans. Magn. **32**, p67 (1996)

[81] Y. Guo, J. Chang, K. Ju: *Low fringe-field and narrow-track MR head*, IEEE Trans. Magn. **33**, p2827 (1997)

[82] T. Hamaguchi, T. Ichihara, F. Tomiyama, M. Hara, K. Akagi, and H. Takano: *A technique for capturing the transition curvature and analysis of the write head characteristics*, J. Appl. Phys. **87**, p5004 (2000)

[83] P. Rice, J. R. Hoinville: *Spatial correlation between magnetic force microscope images and recording head output*, IEEE Trans. Magn. **32**, p3563 (1996)

[84] J. R. Hoinville, R. S. Indeck, M. W. Muller: *Spatial noise phenomena of longitudinal magnetic recording media*, IEEE Tans. Magn. **28**, p3398 (1992)

[85] G. Binasch, P. Gr§nberg, F. Saurenbach, W. Zinn: *Enhanced magnetoresistance in layered magnetic structures with antiferromagnetic interlayer exchange*, Phys. Rev. B **39**, p4828 (1989).

[86] M. N. Baibich, J. M. Broto, A. Fert, F. Nguyen Van Dau, F. Petroff: *Giant magnetoresistance of (001)Fe/(001)Cr magnetic superlattices*, Phys. Rev. Lett. **61**, p2472 (1988).

[87] B. Dieny, V. S. Speriosu, S. Metin, S. S. P. Parkin, B. A. Gurney, P. Baumgart, D. R. Wilhoit: *Magnetotransport properties of magnetically soft spin-valve structures*, J. Appl. Phys. **69**, p4774 (1991).

[88] W. H. Meiklejohn, C. P. Bean: *New magnetic anisotropy*, Phys. Rev **102**, p1413 (1956).

[89] W. H. Meiklejohn, C. P. Bean: *New magnetic anisotropy*, Phys. Rev. **105**, p904 (1957).

[90] W. H. Meiklejohn: *Exchange anisotropy: A review*, J. Appl. Phys. **33**, p1328 (1962).

[91] D. Mauri, H. C. Siegmann, P. S. Bagus, E. Kay: *Simple model for thin ferromagnetic films exchange coupled to an antiferromagnetic substrate*, J. Appl. Phys. **62**, p3047 (1987).

[92] K. Takano, R. H. Kodama, A. E. Berkowitz: *Interfacial uncompensated antiferromagnetic spins: Role in unidirectional anisotropy in polycrystalline $Ni_{81}Fe_{19}/CoO$ bilayers*, Phys. Rev. Lett. **79**, p1130 (1997).

[93] A. P. Malozemov: *Random-field model of exchange anisotropy at rough ferromagnetic-antiferromagnetic interfaces*, Phys. Rev. B **35**, p3679 (1987).

[94] B. Beschoten, J. Keller, P. Mitenyi and G. Güntherodt: *Domain state model for exchange bias: thickness dependence of diluted antiferromagnetic $Co_{1-y}O$ on exchange bias in Co/CoO*, J. Magn. Magn. Mat. **240**, p248 (2002).

[95] S. M. Rezende, A. Azevedo, F. M. de Aguiar, J. R. Fermin, W. F. Engelhoff, S. S. P. Parkin: *Three-layer model for exchange anisotropy*, Phys. Rev. B **66**, p064109 (2002)

[96] M. D. Stiles, R. D. McMicheal: *Model for exchange bias in polycrystalline ferromagnet-antiferromagnet bilayers*, Phys. Rev. B **59**, p3722 (1999).

[97] A. P. Malozemov: *Mechanisms of exchange anisotropy*, J. Appl. Phys. **63**, p3874 (1988)

[98] A. P. Malozemov: *Heisenberg-to-Ising crossover in a random-field model with uniaxial anisotropy*, Phys. Rev. B **37**, p7673 (1988)

[99] L. Néel: *Etude theorique du couplage ferro-antiferromagnetique dans les couches minces*, Ann. Phys. Paris **2**, p61 (1967).

[100] D. Paccard, C. Schlenker, O. Masseneto: *A new property of ferromagnetic-antiferromagnetic coupling*, Phys. Stat. Solidi **16**, p301 (1966).

[101] V. I. Nikitenko: *Asymmetry of domain nucleation and enhanced coercivity in exchange-biased epitaxial NiO/NiFe bilayers*, Phys. Rev. B **57**, pR8111 (1998).

[102] O. Hellwig, private communications.

[103] M. Takahashi, A. Yanai, S. Taguchi, T. Suzuki: *A study of exchange anisotropy in Co-CoO evaporated thin films*, Japn. Jpn. J. Appl. Phys. **19**, p1093 (1980).

[104] M. B. Stearns: *Mechanism for enhanced unidirectional spin-glass behavior in layered Mn-Ni/Co structures*, J. Appl. Phys. **55**, p1729 (1984).

[105] C. Schlenker, J. Phys, Colloq. **29**, pC2-157 (1968).

[106] C.-H. Lai, H. Matsuyama, R.L. White, T.C. Anthony, G. G. Bush: *Exploration of magnetization reversal and coercivity of epitaxial NiO {111}/NiFe film*, J. Appl. Phys. **79**, p6389 (1996).

[107] J. Smit, Philips Res. Rep. **10**, p113 (1955).

[108] J. B. Kortright, S.-K. Kim: *Resonant magneto-optical properties of Fe near its 2p levels:ÊMeasurement and applications*, Phys. Rev. B **62**, p12216 (2000).

[109] H. Ohldag, A. Scholl, F. Nolting, E. Arenholz, S. Maat, A. T. Young, M. Carey, J. Stöhr: *Correlation between exchange bias and pinned interfacial spins*, Phys. Rev. Lett. **91**, 017203 (2003)

[110] H. Ohldag, T. J. Regan, J. Stöhr, A. Scholl, F. Nolting, J. Lüninhg, C. Stamm, S. Anders, R. L. White: *Spectroscopic identification and direct imaging of interfacial magnetic spins*, Phys. Rev. Lett. **87**, p247201 (2001).

[111] S. Maat, K. Takano, S. S. P. Parkin, and E. E. Fullerton: *Perpendicular exchange bias of Co/Pt multilayers*, Phys. Rev. Lett. **87**, p087202 (2001).

[112] T. L. Kirk, O. Hellwig, E. E. Fullerton: *Coercivity mechanisms in positive exchange-biased Co films and Co/Pt multilayers*, Phys. Rev. B 7textbf65, p224426/1 (2002)

[113] L. Congxiao, D. Jianhua, J. A. Barnard, G. J. Mankey: *Study of exchange anisotropy for $Ni_{80}Fe_{20}/Fe_{60}Mn_{40}$ (111) epitaxial films*, J. Vac. Sci. Techn. A **19**, p1213 (2001)

[114] L. Xiangdong, G. Z. Jian, W. Geng: *MFM study on temperature dependence of domain configuration in NiFe films exchange biased by FeMn*, IEEE Trans. Magn. **33**, p3987 (1997)

[115] O. Hellwig, S. Maat, J. B. Kortright, and E. E. Fullerton: *Magnetic reversal of perpendicularly-biased Co/Pt multilayers*, Phys. Rev. B **65**, p144418 (2002).

[116] K. O'Grady, S. J. Greaves, and S. M. Thompson: *Exchange anisotropy effects in NiFe layers and NiFe/Cr multilayers*, J. Magn. Magn. Mater. **156**, p253 (1996).

[117] G. Bottoni, D. Candolfo, and A. Cecchetti: *Effect of the coupling between Co and CoO in metal evaporated tapes*, J. Magn. Magn. Mater. **155**, p297 (1996).

[118] P. Miltényi, M. Gierlings, M. Bamming, U. May, G. Güntherodt, J. Nogués, M. Gruyters, C. Leighton, I. K. Schuller, Appl. Phys. Lett. **75**, p2304 (1999).

[119] N. J. Gökemeijer, J. W. Cai, and C. L. Chien: *Memory effects of exchange coupling in ferromagnet/ antiferromagnet bilayers*, Phys. Rev. B **60**, p3033 (1999).

[120] M.S. Pierce, L.B. Sorensen, S.D. Kevan, K.M Chesnel, J.B. Kortright, O. Hellwig, E.E. Fullerton: *Disorder-induced microscopic magnetic memory*, submitted to Phys. Rev. Lett.

[121] H. A. Kramers: *On the exchange interaction in magnetic crystals*, Physica **1**, p182 (1934)

[122] P. W. Anderson:Ê*Antiferromagnetism. Theory of superexchange interaction*, Phys. Rev. **79**, p350 (1950)

[123] T. Nagamiya, K. Yosida, R. Kubo: *Dynamical behavior of antiferromagnetic sublattice magnetization vectors. I*, Adv. Phys **4**, p1 (1955)

[124] M. Gruyters, D. Riegel: *Strong exchange bias by a single layer of independent antiferromagnetic grains: The CoO/Co model system*, Phys. Rev. B **63**, p052401 (2000).

[125] F. Radu, M Etzkorn, S. Siebrecht, T. Schmitte, K. Westerholt, H. Zabel: *Interfacial domain formation during magnetization reversal in exchange-biased CoO/Co bilayers*, Phys. Rev. B **67**, p134409 (2003).

[126] W. L. Roth: *Magnetic Structures of MnO, FeO, CoO, and NiO*, Phys. Rev. **110**, p1333 (1958).

[127] H. P. Myers, J. Sucksmith: *The Spontaneous Magnetization of Cobalt*, Proc. Roy. Soc. London, ser. A **207**, p427 (1951).

[128] J. H. Greiner, A. E. Berkowitz, and J. E. Weidenborner: *Exchange anisotropy properties in sulfided iron films*, J. Appl. Phys. **37**, 2149 (1966).

[129] U. Nowak, K. D. Usadel, J. Keller, P. MiltŐnyi, B. Beschoten, G. Güntherodt: *Domain state model for exchange bias. I. Theory*, Phys. Rev. B **66**, p014430 (2002),

[130] B. van Laar: *Multi-Spin-Axis Structure for CoO*, Phys. Rev. **138**, pA584 (1965).

[131] T. Pan, G. W. D. Spratt, L. Tang, D. E. Laughlin: *Magnetic properties and microstructure of evaporated Co oxide tape media*, J. Magn. Magn. Mat. **155**, p309 (1996).

[132] B. H. Miller, E. D. Dahlberg: *Use of the anisotropic magnetoresistance to measure exchange anisotropy in Co/CoO bilayers*, Appl. Phys. Lett **69**, p3932 (1996).

[133] S. Spagna, M B. Maple, R. E. Sager: *Ultrahigh vacuum SQUID magnetometry study of the magnetic properties of Co/Co-oxide thin films*, J. Appl. Phys. **79**, p4926 (1996).

[134] J. Kanamori, Prog. Theor. Phys. **17**, p177 (1957).

[135] X. Lin, G. C. Hadji, S. I. Shah: *Magnetic and structural properties of Co/CoO bilayers*, J. Appl. Phys. **75**, p6676 (1994).

[136] L. Smardz, U. Köbler, W. Zinn: *Oxidation kinetics of thin and ultrathin cobalt films*, J. Appl. Phys. **71**, p5199 (1992).

[137] J.-V. Kim, R. L. Stamps, B. V. McGrath, R. E. Camley: *Angular dependence and interfacial roughness in exchange-biased ferromagnetic/antiferromagnetic bilayers*, Phys. Rev. B **61**, p8888 (2000)

[138] F. Nolting, A. Scholl, J. Stör, J. W. Seo, J. Fompeyrine, H. Slegwart, J.-P. Locquet, S. Anders, J. Lüning, E. E. Fullerton, M. F. Toney, M. R. Scheinfein and H. A. Padmore, Nature **405**, p767 (2000).

[139] F. T Parker, K Takano, and A. E. Berkowitz: *Exchange coupling mechanisms at ferromagnetic/CoO interfaces*, Phys. Rev. B **61**, R866 (2000)

List of symbols and abbreviations

H	magnetic stray field
M	magnetization
F	force (between cantilever and sample)
σ_M, σ	magnetic surface charge
ρ_M	magnetic volume charge
Φ_M	magnetic scalar potential
f, f_0	frequency, resonance frequency
$\delta f, \Delta f$	frequency shift, frequency shift range
c_L	cantilever spring constant
A	cantilever oscillation amplitude
$k = |\mathbf{k}|$	magnetic wave vector
$\lambda = 2\pi/k$	magnetic wavelength
$\lambda_r = \lambda/2$	measurable magnetic resolution
q_{tip}	tip transfer function
$\sigma_{q_{tip}}$	standard deviation of q_{tip}
ICF	instrumental calibration function
LCF	lever canting function
γ	damping coefficient
m_{eff}	effective spring constant
Q	quality factor
E	Young modulus
t_{CL}, l_{CL}, w_{CL}	thickness, length and width of cantilever bar
B	measurement bandwidth
$\Gamma, \delta z, \delta\theta$	measured dissipation, tip–sample distance variation, oscillation phase variation
U_{bias}	bias voltage
U_{cp}	contact potential voltage
C	tip–sample capacity
A_H	Hamaker contant
K_U	magnetic anisotropy
V	bit volume
a	transition length parameter
T	temperature
T_N	Néel temperature
T_C	Curie temperature
K_{AF}	magnetic anisotropy of the antiferromagnetic layer
A_{AF}	magnetic exchange stiffness within the antiferromagnetic layer
J_{ex}	interface exchange coupling
k_B	Boltzmann constant
μ_0	permitivity of vaccum
μ_B	Bohr magneton

SFM	scanning force microscope
AFM	atomic force microscope
MFM	magnetic force microscope
LTSFM	low temperature scanning force microscope
hr-MFM	high resolution magnetic force microscope
UHV	ultra high vacuum
PLL	phase locked loop
vdW	van der Waals
PMR	perpendicular magnetic recording
LMR	longitudinal magnetic recording
AFC	antiferromagnetic coupled (media)
SUL	soft magnetic under layer
FWHM	full width at half maximum
FEB	field ion beam
PEEM	photoelectron emission microscopy
SEMPA	scanning electron microscope with polarization analysis
LEED	low energy electron diffraction
SQUID	scanning quantum interference device
MOKE	magneto-optical Kerr effect
FMR	ferromagnetic resonance
XMCD	x-ray magnetic circular dicroism
XMLD	x-ray magnetic linear dicroism
TJ	transition jitter
TPJ	transition position jitter
FM	ferromagnetic
AF	antiferromagnetic

Publication List

- P. J. A. van Schendel, H. J. Hug, R. Hoffmann, S. Martin, P. Kappenberger, H.-J. Güntherodt: *Applications of tip calibration in magnetic force microscopy (MFM)*, Magnetic Storage Systems beyond 2000 (Proceedings of the NATO Advanced Study Institute), p313 (2001)

- M. A. Lantz, H. J. Hug, R. Hoffmann, P. J. A. van Schendel, P. Kappenberger, S. Martin, A. Baratoff, H.-J. Güntherodt: *Quantitative measurement of short-range chemical bonding forces*, Science **291**, p2580 (2001)

- R. Hoffmann, M. A. Lantz, H. J. Hug, P. J. A. van Schendel, P. Kappenberger, S. Martin, A. Baratoff, H.-J. Güntherodt: *Atomic resolution imaging and force versus distance measurements on KBr(001) using low temperature scanning force microscopy*, Appl. Surf. Sci. **88**, p238 (2002)

- H. J. Hug, P. Kappenberger, S. Martin, P. Reimann, R. Hoffmann, J. Rychen, W. Lu, H.-J. Güntherodt: *High resolution quantitative magnetic force microscopy*, IEEE International Magnetics Conference (Intermag Europe 2002 Digest of Technical Papers), Cat.No. **02CH37323** (2002)

- R. Hoffmann, M. A. Lantz, H. J. Hug, P. J. A. van Schendel, P. Kappenberger, S. Martin, A. Baratoff, H.-J. Güntherodt: *Atomic resolution imaging and frequency versus distance measurements on NiO(001) using low-temperature scanning force microscopy*, Phys. Rev. B **67**, p85402-1 (2003)

- P. Kappenberger, H. J. Hug, S. Martin, H.-J. Güntherodt, D. Buchel, J. Ahner, D. Weller: *A novel high resolution quantitative magnetic force microscope for hard disk research*, 2nd North American Perpendicular Magnetic Recording Conference 6th Perpendicular Magnetic Recording (DIGEST Joint [NA]PMRC 2003), Cat.-No. **03EX650** (2003)

- A. Moser, P. Kappenberger, H. J. Hug, S. Martin, H.-J. Güntherodt: *Measurement of the transition parameter in longitudinal recording media using a magnetic force microscope*, accepted for publication in Appl. Phys. Lett. (2003)

- P. Kappenberger, S. Martin, Y. Pellmont, H. J. Hug, J. B. Kortright, O. Hellwig, Eric E. Fullerton: *Direct imaging and determination of the uncompensated spin density in exchange-biased CoO/(CoPt) multilayers*, accepted for publication in Phys. Rev. Lett (2003)

Curriculum Vitae

1.3.1973	Born in Stuttgart, Germany. Son of Roland Kappenberger and Inge Kappenberger-Klotz
1979–1983	Primary School "Mörike", Leonberg, Germany
1983–1992	Gymnasium "Johannes Kepler", Leonberg, Germany
1993–1995	Study of Physics at the University of Basel
1995–1998	Study of Physics at the University of Stuttgart, Germany
1998–1999	Diploma thesis at the Max Planck Institute, Stuttgart (Germany), under the supervision of Prof. Dr. J. Maier and Prof. Dr. M. Rühle with the title: "Determination of the bonding charge density of $SrTiO_3$ by means of covalent electron beam diffraction."
1999–2004	Ph.D. thesis at the University of Basel under the supervision of Prof. Dr. H. J. Hug and Prof. Dr. H.-J. Güntherodt

Acknowledgements

The work presented in this thesis could never have been performed without the guidance and support of many people in and outside the Institute of Physics at the University of Basel.

First of all, I would like to thank Prof. Dr. H.-J. Güntherodt, head of the scanning microscopy group in Basel, for making this project possible and his continuous interest in my work. I particularly profited from his positive attitude and from his outstanding will to promote young students. I also thank Prof. Dr. Ernst Meyer for being the second referee of my thesis.

I wish to express profound gratitude to Prof. Dr. H. J. Hug for his help throughout this thesis. His precise way of thinking and his profound knowledge of physics in general and understanding of magnetics in particular, have always been a guidance for me and have positively influenced my personality. He taught me that every problem in experimental physics can be solved and that nothing works without a reason. I would like to thank him for his time and patience in discussing and interpreting the results of my experiments.

I would like to thank all past and present scientific co-workers in the LTSFM group, whose contributions can be found in all parts of this thesis: Dr. P. J. A. van Schendel, Dr. R. Hoffmann, Dr. M. A. Lantz, Dr. W. Lu, Dr. J. Rychen, Dr. T. V. Ashworth, Dr. A. Drechsler, I. Schmid, N. Pilet and M. Meili. I also would like to express my gratitude to the technicians in the group, S. Martin and Y. Pellmont, who always provided help with large and small problems of all kinds.
In this respect, I also want to thank Ing. HTL P. Reimann for his endless help with technical and logistic problems. Furthermore, I would like to thank the following people at the University of Basel, who have all contributed to the results presented in this work in one way or another. I am really happy to have worked together with them.

- The people from the Mechanical workshops, for constructing of small and large parts.

- The people from the Electronic workshops, especially A. Tonin who taught me the secrets of electronic circuit design.

- The secretaries of the third and fist floor, G. Weaver, J. Vetter, E. Fischer, A. Kalt and B. Kammermann.

- Prof. Dr. H. J. Hug, Dr. T. V. Ashworth, M. De Serio, I. Schmid, Dr. V. Barwich and A. Bredekamp for critically reading the manuscript.

I would also like express thanks to the many collaborators and contributors from outside the University of Basel for their support and knowledge, namely:

- Dr. J. Greschner from Team Nanotec (Germany) for providing ultrasharp Si-cantilevers without which we would not have made the step into high resolution magnetic force microscopy.

- Dr. I. Utke at the EPFL, Lausanne (Switzerland) for providing me with the supersharp, FEB-grown magnetic tips.

- Dr. D. Weller and Prof. Dr. J. Ahner at Seagate Reseach Center, Pittsburgh (USA) for providing all kinds of recording media and a new cantilever calibration sample.